Interfacial Degradation Processes in Electrochemical Energy Storage and Conversion

Dongni Zhao

This dissertation is submitted for the degree of
Doctor of Philosophy

March 2025

Department of Chemistry
Lancaster University

Declaration

This thesis has not been submitted in support of an application for another degree at this or any other university. It is the result of my own work and includes nothing that is the outcome of work done in collaboration except where specifically indicated. Many of the ideas in this thesis were the product of discussion with my supervisor Prof Stijn Mertens.

Interfacial degradation processes in electrochemical energy storage and conversion –

Dongni Zhao – December 2024

Abstract

The comprehensive usage of clean energy is the biggest challenge of society in the 21st century. Advanced energy storage and conversion systems play a critical role in this vision, and electrochemical energy storage and conversion are the most promising candidates. However, their premature ageing limits their wider application. One of the biggest issues is the active material dissolution under electrochemical conditions, but the limited availability of characterization methods hinders an in-depth understanding of the process as well as mitigation strategies.

In this thesis, we develop real-time/*in-situ*/*operando* electrochemical techniques to study the degradation processes and mechanisms happening at the electrode-electrolyte interfaces within the Li-ion battery and water electrolyzer. We first establish online inductively coupled plasma-optical emission spectrometry (online ICP-OES) for real-time electrolyte analysis, enabling the direct detection of transition metal dissolution from Li-ion cathodes, taking $LiMn_2O_4$ (LMO) as an example.

Then, we apply the rotating ring-disc electrode (RRDE) technique for real-time speciation of the dissolving transition metal ions, which is the basis of a comprehensive understanding of the dissolution mechanism, and supplements findings from online ICP-OES, which could provide extraordinary detection limits for multiple elements but is blind to the oxidation states of the dissolving species. We focus on Mn, and combine voltammetry on stationary and rotating electrodes with electrochemical impedance spectroscopy and Raman spectroscopy. With the understanding of Mn behaviour on the ring and disc electrodes, respectively, we then investigate LMO dissolution and speciation on the ring electrode in real-time.

One of the widely reported Mn dissolution mitigation strategies is to replace one-fourth of the Mn in LMO with Ni, which then forms $LiNi_{0.5}Mn_{1.5}O_4$ (LNMO). We compared the chemical composition, morphology, crystal structure, and electrochemical properties including cycling capacity, stability, and rate capability of 2 commercial and 3 lab-synthesized LNMO samples. Their dynamic phase transformation during (dis)charging was observed by *operando* Raman spectroscopy, aimed at studying the dynamic cathode-electrolyte interphase (CEI) changes under different electrochemical conditions and their impact on cycling and rate performances.

Water electrolysis is considered to be the most promising way to generate green hydrogen as the next-generation energy carrier. Such a process includes the hydrogen evolution reaction (HER) on the cathode and the oxygen evolution reaction (OER) on the anode. The complexity and sluggish kinetics of OER make it often the limit of the whole process and thus usually requires advanced electrocatalysts. Ideal OER electrocatalysts should have both excellent activity and stability. While the former can be directly observed electrochemically, the latter is usually hard to characterize due to the lack of available techniques. We here employed online ICP-OES for direct detection of active material dissolution of several promising candidates of OER electrocatalysis, which provide direct evidence of the stability of the electrocatalysts.

To summarize, we established several real-time/*in-situ*/*operando* electrochemical techniques for studying the electrode-electrolyte interface in electrochemical energy storage and conversion systems. These results will help to better understand and mitigate the premature ageing of those systems.

Acknowledgement

First and foremost, I would like to express my deepest gratitude to my supervisor Professor Stijn Mertens for the invaluable guidance, support, and encouragement throughout my entire study.

To Dr Shahin Nikman for the training and help at the very beginning of my study, which put in place a very solid foundation for my following research. To Dr Enrico De Bonis for all the helpful discussions regarding electrochemistry. To Ms Mandana Azmi for the extensive training on scanning probe microscopy and image processing. To Prof Yue Chen for not only the discussions within the NEXGENNa project but also for the help for Raman setup and collaborations of post-Li batteries afterwards. To Dr Li Zhang for all the practical battery-related training. To Dr Bing Han for the electron microscopy measurements. To Dr Xiao Hua, Dr Zhenjiang Yu, and Dr Hekang Zhu for the help with XRD and crystallography. To Dr Rebecca Pittkowski, Dr Da Xing, and Mr Leander Kucklick for the collaborations in OER studies.

To all the colleagues and staff at the Chemistry department, especially Dr David Rochester and Dr Sara Baldock for the help and support for many instruments. To Dr John Hardy, Dr John Fielden, and Dr Nuria Tapia-Ruiz for not only helping monitor my progress throughout my study, but also suggestions for many other aspects.

To my family and friends who have always been my source of motivation, especially my parents for the support not only morally but also financially. To my partner Dr Yuezhen Lu for the invaluable support throughout my study and life.

Last but not least, I am deeply grateful for the financial support from the Chemistry Department at Lancaster University and the Faraday Institution NEXGENNa project. I would like to also acknowledge the receipt of a Sydney Andrew Scholarship from the Society of Chemical Industry and a Chinese Students Award from the Great Britain-China Educational Trust (GBCET).

List of publications

Journal:

1. Yue Chen, Shaohua Zhang, Dongni Zhao, Zhixian You, Yubiao Niu, Liqiang Zeng, Nagarathinam Mangayarkarasi, Oleg V Kolosov, Jianming Tao, Jiaxin Li, Yingbin Lin, Yongping Zheng, Long Zhang, Zhigao Huang, Deciphering the structure and kinetics in the performance enhancement of lithium titanate in Li^+/Na^+ dual-cation electrolyte. *Journal of Colloid and Interface Science*, **676**, 603-612 (2024).
2. Shaohua Zhang, Chun Lin, Jiefeng Ye, Dongni Zhao, Yue Chen, Jian-Min Zhang, Jianmin Tao, Jiaxin Li, Yingbin Lin, Stijn FL Mertens, Oleg V Kolosov, Zhigao Huang, Bi_2S_3/rGO nanocomposites with covalent heterojunctions as a high-performance aqueous zinc ion battery material. *Ceramics International*, **49**, 22160–22169 (2023).
3. Tugce Kutlusoy, Spyridon Divanis, Rebecca Pittkowski, Riccardo Marina, Adrian M Frandsen, Katerina Minhova-Macounova, Roman Nebel, Dongni Zhao, Stijn FL Mertens, Harry Hoster, Petr Krtil, Jan Rossmeisl, Synergistic effect of P-type and N-type dopants in semiconductors for efficient electrocatalytic water splitting. *Chemical Science*, **13**, 13879–13892 (2022).
4. Shahin Nikman, Dongni Zhao, Violeta Gonzalez-Perez, Harry E Hoster, Stijn FL Mertens, Surface or bulk? Real-time manganese dissolution detection in a lithium-ion cathode. *Electrochimica Acta*, **386**, 138373 (2021).

Conference contribution:

1. SCI Early career materials annual conference 2024 Frontiers in battery materials (London, UK): “Understanding Mn dissolution from $LiMn_2O_4$ cathodes”.
2. 37th ISE Topical Meeting (Stresa, Italy): “Understanding Mn dissolution from $LiMn_2O_4$ cathodes”.
3. 74th Annual ISE Meeting (Lyon, France): “Real-Time Speciation of Dissolving Mn from a Li-ion Battery Cathode”.
4. 243rd ECS Meeting (Boston, US): “Real-Time Detection and Speciation of Mn Dissolution in a Li-ion Battery Cathode”.
5. 243rd ECS Meeting (Boston, US): “Covalent Heterojunctions Enhance Bi_2S_3/rGO Nanocomposite Performance as Aqueous Zinc Ion Battery Material”.
6. 2022 IOP BRSG Summer Annual Group Meeting (Lancaster, UK): “Real-Time Dissolution Probing of Battery Electrode Materials”.
7. Electrochem 2022 (Edinburgh, UK): “Real-Time Manganese Dissolution Detection in a Li-ion Battery Cathode”.

Table of Contents

List of figures

List of tables

Chapter 1. Introduction

1-1 Renewable energy

The shift from fossil fuel to renewable energy is one of the most significant challenges in the 21st century, which is motivated by several key factors. Using fossil fuels has been proven to result in not only serious greenhouse gas emissions but also air pollution. The former is a major driving force of global climate change and the latter can cause many human diseases.[1–3] Besides, fossil fuels can become scarcer, which will increase the cost in the meantime, and eventually run out.[4] In addition, the survival and activities of humans, animals, plants, etc. are often interdependent and mutually beneficial, and thus such a shift can help to achieve a better ecosystem.[5]

Advanced energy storage and conversion systems are indispensable for the utilization of renewable and clean energy that is required for the further development of human society due to the following reasons: 1) energy storage and conversion systems enable many portable devices, such as smartphones, electric vehicles, etc., making our lives more convenient and intelligent; 2) clean energy, such as wind and solar energy, is often intermittent, while the demand from human society for energy often does not change with the availability of these energy sources. Therefore, proper energy storage and conversion systems can support a stable energy supply; 3) in emergencies such as natural disasters or similar situations that render traditional power generation equipment unavailable, novel energy storage and conversion systems can serve as a backup energy source.[6–8]

Among energy storage and conversion systems, electrochemical energy storage systems, such as Li-ion battery (LIB) and its derivative,[9–12] and electrochemical energy conversion systems, such as fuel cell[13,14] and water electrolyzer,[15,16] are attracting increasing attention thanks to their improved performances in the past decades. However, due to their premature ageing, further research is still required to enable complete replacement of fossil fuels with clean energies.[17–19]

1-2 Li-ion battery and its degradation

A Li-ion battery (LIB) cell consists of cathode, anode, separator, and electrolyte, Figure 1-1. In practice, a battery is mostly formed by many cells, which are connected in parallel, while only one cell is considered as the research object in electrochemical laboratory. Therefore, all the words ‘cell’ and ‘battery’ refer to one cell in this thesis.

Typical cathode and anode active materials are usually synthesized as powders. The cathode or anode materials are mixed with the conductive agent (e.g. super P carbon) and binder (e.g. polyvinylidene fluoride, PVDF) in a proper solvent (e.g. N-methyl-2-pyrrolidone, NMP) to form an electrode slurry, which is then coated on the current collector and dried. After that, the dried electrode is cut into the desired shape to form a cell. Commonly used separators include porous polypropylene (PP) or polyethylene (PE) membranes. The commercial electrolytes include $LiPF_6$ or similar salts in a mixture of linear and cyclic carbonates (e.g. ethylene carbonate, EC, and dimethyl carbonate, DMC) solvent.

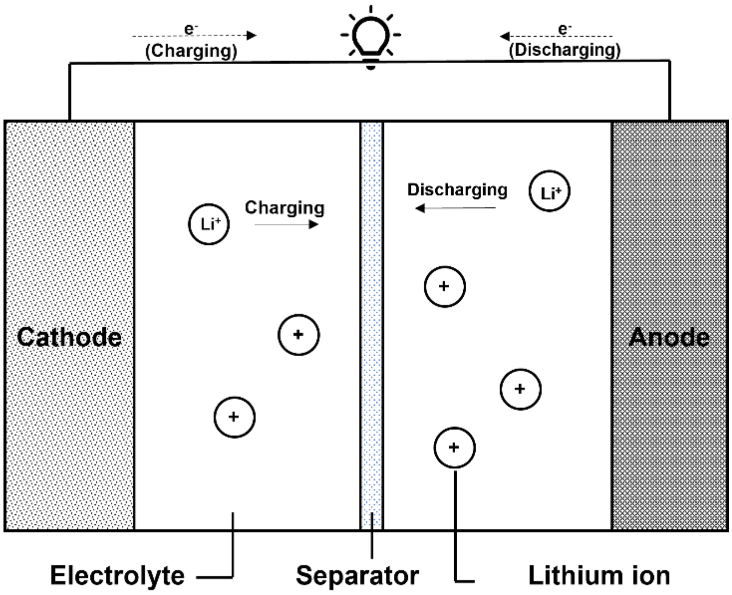

Figure 1-1. Schematic diagram of a LIB.

During (dis)charging, Li ions are extracted from the cathode or anode before being transported to and inserted into the other through the electrolyte. Simultaneously, the same number of electrons go through the external circuit to maintain the charge balance and form current. Taking the commercially available transition metal (M=Mn, Co, Ni, etc.) oxide cathode and graphite anode as an example, the reactions during charging can be described by Equation 1-1 and Equation 1-2.

Cathode: $$\mathrm{LiMO_2 - xe^- \xrightarrow{charging} Li_{1-x}MO_2 + xLi^+}$$ Equation 1-1

Anode: $$\mathrm{C + xLi^+ + xe^- \xrightarrow{charging} CLi_x}$$ Equation 1-2

The processes are reversed during discharging. The process of charge transfer between one electrode and the electrolyte is defined as a half-cell reaction, and the overall cell voltage is dependent on the potential difference between the two half-cell reactions. The separator is usually placed between the cathode and anode, and it allows Li ions to pass through while preventing direct contact between the two electrodes.

Although LIB is designed to have only fully reversible reactions as described by Equation 1-1 and Equation 1-2, in practice, both cathode and anode experience significant volume changes when inserting and extracting Li^+, which is likely to cause collapse and failure from the crystal structure to the electrode scale. Subsequently, such volume change is likely to result in or exacerbate the loss of contact, growth of electrode-electrolyte interphase, etc., which draws lifespan and safety concerns of LIB.[20–22]

Not only the properties of the components themselves are essential but also the interfaces between them play decisive roles in the overall performance of a LIB, as the electrochemical Li insertion and extraction always happen at the electrode-electrolyte interfaces. An ideal LIB is designed to only have the chemically fully reversible Li insertion and extraction reactions happening, but in reality, electrochemical and chemical side reactions occur that limit the performance of LIBs.[23,24]

1-2.1 Degradation of cathode

1-2.1.1 Overview

The cathode usually has a lower theoretical capacity than the anode and suffers from more serious degradation, making it the limiting factor of the overall capacity and life span of a LIB. Thus, a clear understanding of the degradation process and mechanism that take place on the cathode-electrolyte interface is beneficial for the further development of LIBs.[17,25,26] During cycling of a LIB, the cathode-electrolyte interphase (CEI) is formed by the decomposition products, such as LiF, Li_2CO_3, MnF_x, ROLi (R: alkyl group), etc., from both the cathode and the electrolyte.[27–30] CEI is widely believed to affect kinetics of the Li^+ interfacial charge transfer and usually undergoes dynamic changes during (dis)charging. Thus, it is essential to understand its formation process and mechanism. [27–30]

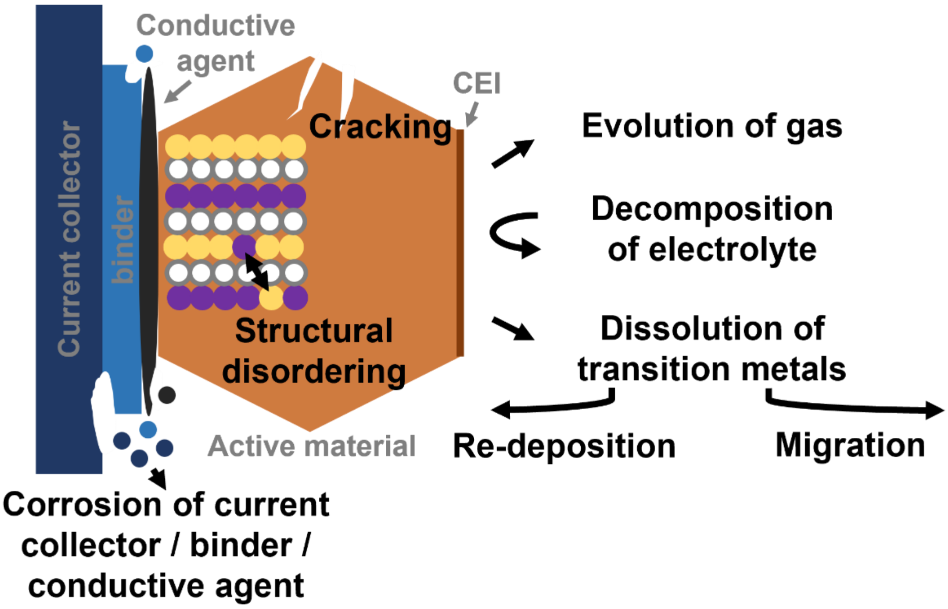

Figure 1-2. Schematic diagram of the cathode degradation processes in a LIB.

Multiple side reactions can happen on the cathode and its surface, which will affect the performance of the battery, Figure 1-2. These side reactions can be divided into four categories: 1) loss and/or ageing of the cathode active material; 2) degradation of the cathode electrode components (i.e. conductive agent, binder, or current collector); 3) decomposition of the electrolyte; 4) further reaction between the ageing products and other components (i.e. anode, electrolyte, or separator) in the LIB. The driving forces behind these side reactions may be electrochemical, chemical, or mechanical (e.g. in cracking of solid material).[17,23]

1-2.1.2 Transition metal dissolution

Among the rest, transition metal dissolution is an important but poorly understood side reaction. On the one hand, dissolution can result in serious irreversible loss of active redox sites, subsequently, the surface and structure of the cathode itself as well as the CEI can also be affected. On the other hand, the dissolved transition metal ions tend to migrate to the anode side during charging because of the potential gradient, which may then exacerbate the formation of solid-electrolyte interphase (SEI) or the decomposition of the electrolyte.[31–34]

There is no doubt that a clear understanding of the transition metal dissolution mechanism is a critical prerequisite for mitigation strategies. Furthermore, materials with better performances and longevities can be effectively screened and designed.

Hunter proposed a Mn^{2+} dissolution mechanism during chemical de-intercalation of Li^+ from spinel $LiMn_2O_4$ (LMO) in an acidic aqueous solution, Equation 1-3.[35]

$$2LiMn_2O_4 + 4H^+ \rightarrow 3\lambda\text{-}MnO_2 + Mn^{2+} + 2Li^+ + 2H_2O \qquad \text{Equation 1-3}$$

The mechanism proposed that with the Li^+ extracted from the spinel, the Mn^{3+} on the surface will disproportionate to Mn^{2+} and Mn^{4+}, while the former is soluble and the latter is not. Such conversion from LMO to λ-MnO_2 can keep the tetrahedral structure of LMO, although the unit cell will slightly shrink. As more Li^+ is extracted from the structure, more Mn^{4+} will accumulate on the surface of the spinel.

This mechanism was then adapted into the LIB research field for explaining the Mn dissolution from Mn-containing cathodes during Li^+ (de-)intercalation, where Mn^{2+} was believed to be the only dissolving species. Subsequently, similar processes have been suggested to occur in other transition metals-containing cathodes (i.e. Ni, Co, etc.).[32,36–39]

Attempts have been made for understanding the dissolution processes from Mn-containing Li-ion cathodes. Jang et al. analyzed the dissolution from spinel $Li_xMn_2O_4$ by intermittently sampling the electrolyte with differential pulse polarography analysis, where the accuracy of the responses is strongly dependent on the surface state of the electrode used for detection.[40] Hanf et al. combined electrophoresis with ultraviolet-visible (UV-Vis) absorption spectroscopy for *ex-situ* Mn dissolution detection and speciation.[41] Although they successfully detected, quantified, and distinguished the dissolving Mn^{2+} and Mn^{3+}, their method is hard to use in other transition metals (Ni, Co, etc.) dissolution study due to the instability of the complexing agent needed. Zhao et al. developed a novel UV-Vis probe, which allows them to *in-situ* monitor the Mn^{2+} dissolution.[42] Wang et al. detected the Mn dissolution from $LiMn_2O_4$ (LMO) by adding a sensing electrode in a Swagelok cell,[43] by which they found current contributed by non-Mn^{2+} species.[43] Wang et al. applied rotating ring-disc electrode collection experiments to detect the dissolving Mn^{2+}. However, their chosen potential for detection was too negative and thus all Mn species could be reduced and detected.[44–46] The Aurbach group combined electron paramagnetic resonance (EPR) spectroscopy, inductively coupled plasma-atomic absorption spectroscopy (ICP-AAS), and X-ray absorption near-edge spectroscopy (XANES) for *ex-situ* analysis and claimed that Mn^{3+} is the main dissolving species from $LiMn_2O_4$ (LMO) while Mn^{2+} is predominant for $LiNi_{0.5}Mn_{1.5}O_4$ (LNMO).[47,48] However, the basis of their interpretation, that Mn(II) is EPR-silent, is under debate.[49] Allen & Grey used solution nuclear magnetic resonance (NMR) and ICP-optical emission spectroscopy (ICP-OES) for *ex-situ* detection and their results suggested that the dissolving species from LMO, $LiNiO_2$ (LNO), and LNMO are exclusively divalent.[50] Rynearson et al. extracted the electrolyte from cells with different Mn-containing cathodes after cycling and analyzed them through the X-ray absorption spectroscopy (XAS) and XANES, their results suggested both Mn^{2+} and Mn^{3+} are dissolving, and their ratio is dependent on the cathode and unrelated to the cycling potential.[51] Terada et al. combined total reflection X-ray fluorescence analysis with XANES for *ex-situ* analysis.[52]

Besides, the dissolution as well as its impact on the anode can be inferred through surface analysis of the anode by laser ablation-inductively coupled plasma-mass spectrometry (LA-ICP-MS),[53] secondary ion mass spectrometry (SIMS),[54] combination of X-ray photoelectron spectroscopy (XPS) and electron microscopy,[55] etc.

However, advanced *in-situ/operando* methods are still desired because: 1) considering the cells that are commonly used in the lab usually have only up to milli litre level electrolyte and the dissolved transition metals are usually present in trace amounts, thus the detection techniques need to have excellent limits of detection; 2) the oxidation states of the dissolving species are hard to distinguish by *ex-situ* methods since some of them could already transform to other form or oxidation stated due to their instability; 3) the dependence of the dissolution on key parameters such as time, potential, state of charge (SoC), (dis)charge history, etc. are essential for dissolution mitigation strategies and better battery operation practices.

1-3 Water electrolyzer and the degradation of its electrocatalysts

Electrolysis for water splitting is one of the most important ways to generate hydrogen as a clean energy carrier, as its combustion only generates water. Such a process involves converting the electricity to chemical energy by splitting the water into molecular hydrogen (i.e. hydrogen evolution reaction, HER) and molecular oxygen (i.e. oxygen evolution reaction, OER), and is considered the most sustainable way for hydrogen generation, especially if renewable electricity can be used.

Water electrolysis can happen in both acidic and alkaline conditions, though the sluggish kinetics of anodic OER always limit the efficiency of the whole process. OER is a complicated reaction as it requires the transfer of 4 electrons and 4 protons (or OH^- ions). Besides being the anodic half-reaction in water electrolysis, OER also occurs in many other electrochemical systems, such as CO_2 reduction and ammonia synthesis.[56] Therefore, the development of OER electrocatalysts is essential for many industries.

Ideal electrocatalysts are expected to be excellent in both activity and stability while having reasonable costs. Although efforts have been made to develop suitable electrocatalysts for OER, the commercially available ones are still a series of noble-metal-based catalysts represented by IrO_2 and RuO_2.[57–59] However, the high cost and scarce reserves of these precious metal oxides make it challenging to work in sustainable industries. Simultaneously, these commercial catalysts typically require operating voltages of more than 1.8 V, which is considerably high. Several other electrocatalysts have been proposed, but they can rarely have both improved reactivity and stability.

Acidic electrolytes have the advantage of a more facile kinetic barrier of HER, higher conductivity, and require less overpotential to reach the same current densities.[60,61] However, most transition metal compounds that have OER activity are thermodynamically unstable in acidic conditions, which can result in serious dissolution.[62] Though some non-precious metal oxides prefer to work in alkaline electrolytes, their reactivity needs to be improved.[56,63,64] In both cases, the stability of the electrocatalysts under OER conditions is one of the biggest issues that require further development for commercialization.

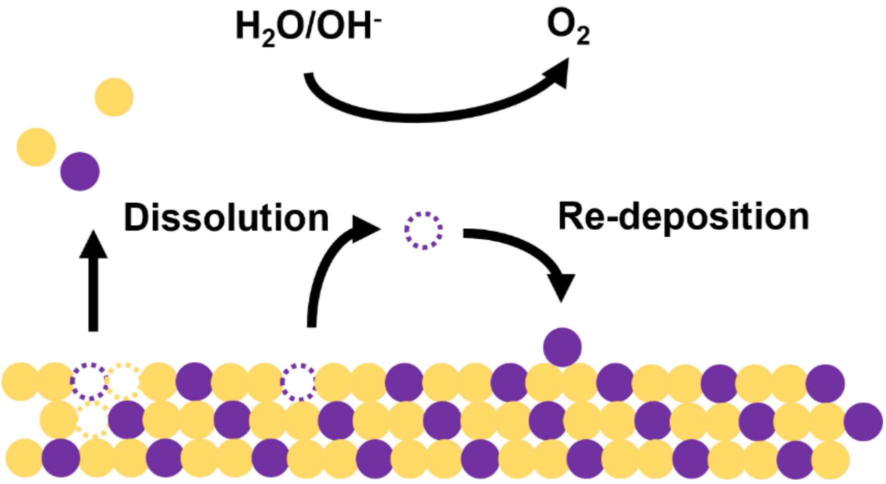

Figure 1-3. Schematic diagram of the degraded OER electrocatalyst surface caused by dissolution and re-deposition.

The main reasons causing degradation of the OER electrocatalysts include surface reconstruction, structure instability, dissolution and redeposition. Compared with the first two, dissolution and subsequent re-deposition are usually the main reasons causing decreased reactivity, Figure 1-3, but they only started drawing attention in recent years. The dissolution process and mechanism are affected by many factors such as the surface, support, operation potential, etc. of the electrocatalyst. Therefore, advanced *in-situ/operando* characterization techniques are an indispensable part of studying this process. Moreover, subsequent redeposition can also have a significant impact on the surface structure and activity of the electrocatalyst in long-term.[65]

Cherevko et al. developed a scanning flow cell/ICP-MS system and quantified six noble metal anodes dissolution under transient and steady-state potential control. They showed that the dissolution of the six noble metals shows similar trends but orders of magnitude differences in the kinetics.[66] Kasian et al. combined isotope labelling with atom probe tomography (APT), and online electrochemical mass spectrometry to quantify the relationship between the degree of lattice oxygen participation in OER and the dissolution of Ir.[67] Frydendal et al. evaluated the degradation of RuO_2 and MnO_x by combining the rotating disc electrode (RDE) test with electrochemical quartz crystal microbalance (EQCM) and ICP–MS.[68]

It is clear that estimating the stability of electrocatalysts by only short-term electrochemical analysis is not sufficient. Combining an electrochemical flow cell with a suitable elemental detection technique, such as ICP-MS or ICP-OES, can provide clues for the degradation process of the electrocatalysts. However, effort is still required to study the relationship between these degradation processes and long-term stability further, as well as between the three main reasons for the decreased performance of the electrocatalyst mentioned above.

1-4 Research objectives and thesis scope

The aim of this thesis is to provide some insights into the current challenges in the electrochemical energy storage and conversion systems mentioned above, that is, the transition metal dissolution process and mechanism in Li-ion battery cathodes, and the dissolution and its relationship with the stability of OER electrocatalysts under different electrolytes and potential controls.

In **Chapter 2**, the advanced characterization techniques established and used in this thesis are introduced, including the electrochemical flow cell-coupled online inductively coupled plasma-optical emission spectrometry (ICP-OES), rotating ring-disc electrode (RRDE) setup, and *operando* Raman spectroscopy. Their working principles, setup optimization, and system validation are discussed in detail.

In **Chapter 3**, the application of online ICP-OES system in the transition metal dissolution from a Li-ion cathode is revealed. The detection of dissolution from $LiMn_2O_4$(LMO) electrodes in real time is shown to reveal the role of surface versus bulk structure effects, electrode potential and degree of lithiation on Mn dissolution. The results indicate that fully lithiated LMO, with an average Mn redox state of 3.5, readily dissolves when brought in contact with 0.2 M Li_2SO_4, but that on initial charging a dissolution–passivation event preceding delithiation abruptly stops further detectable dissolution, until well past fully delithiated λ-MnO_2. The results suggest that by selecting a proper potential window, the dissolution can be mitigated as an alternative to the surface coating, which usually sacrifices the energy density.

In **Chapter 4**, the RRDE setup is used for real-time speciation of the dissolved transition metal ions from a Li-ion cathode, which is another indispensable information for understanding the dissolution mechanism. The results suggest that Mn^{3+} is the dissolving species when LMO approaches the end of charging, while Mn^{2+} dissolves when LMO is overdischarged in the first cycle. In the following scans, another dissolution period that contains both Mn^{2+} and Mn^{3+} is found during the Li^+ extraction from LMO. The data refine the use of Hunter's mechanism in Mn dissolution from Li-ion cathodes and prove the capability of RRDE for quantitative real-time study for transition metals dissolution in Li-ion batteries and beyond.

In **Chapter 5**, the dynamic interfacial change of spinel $LiNi_{0.5}Mn_{1.5}O_4$ (LNMO) as a Li-ion cathode is revealed by *operando* Raman spectroscopy. With the addition of Ni content, the stability of the spinel is assumed to be largely improved. However, interfacial degradation including the dissolution and subsequent phase change is still the limiting factor of its performance. The chemical composition, morphology, crystal structure, electrochemical property, as well as dynamic phase transformation of a few LNMO samples are compared, aiming for insights into the interfacial degradation.

In **Chapter 6**, the degradation of several OER electrocatalysts resulting from their dissolution is measured by online ICP-OES, which was then used to infer the long-term stability of the electrocatalysts. In addition, the dynamic active sites are analyzed with the help of the dissolution data as well as other characterization techniques.

The conclusion and outlook of the project are stated in **Chapter 7**. This chapter aims to give ideas regarding deepening the understanding of the interfacial degradation process of Li-ion battery and electrocatalysis systems and provides insights into their further development.

Chapter 2. Experimental techniques

2-1 Electrochemistry basics

Electrochemistry is the chemical reaction that happens at the interface between an ionic conductor (i.e. the electrolyte) and an electronic conductor (i.e. the electrode). When an external potential is applied, the potential gradient will drive the electrons to go across the interface from the electrode to its adjacent electrolyte or vice versa. In the meantime, the same amount of current will be passed through the external circuit. Figure 2-1 shows the conversion process of oxidised species O (O_{bulk}) from the electrolyte to the reduced species R (R_{bulk}) as an example, which includes the mass transport of O_{bulk} to $O_{surface}$, electron transfer, and mass transport of $R_{surface}$ to R_{bulk}. The rate of the overall conversion process from O_{bulk} to R_{bulk} is always limited by the slowest step among the three.

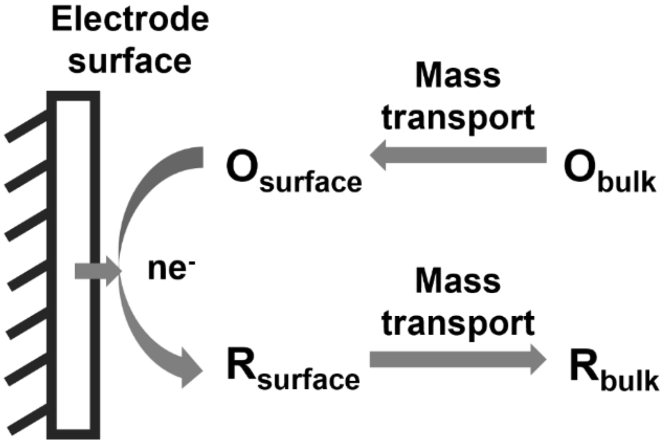

Figure 2-1. Schematic diagram of the electrochemical process happens at the electrochemical interface, taking the reduction reaction from O to R as an example.

At least two of the electrodes shown in Figure 2-1 are required for a working electrochemical cell. To maintain the electrical neutrality of the whole cell, if the species close to one electrode gains electrons, the species close to the other electrode must donate electrons. The former electrode is usually called cathode while the latter is called anode. The anions and cations in the electrolyte move toward the anode and cathode, respectively, due to the electric field in the electrolyte, and the electrons pass through the external circuit from the anode to the cathode.

In theory, the electrons transferred through the external circuit must match with the electrons transferred through the electrode-electrolyte interface. Therefore, the number of electrons passing through the external circuit per unit time is equivalent to the number of electrons transferred by the redox reaction at the electrode surface, directly yielding the current of the electrode reaction.

Considering the electrolysis of water as an example, the smallest potential to drive the reaction can be inferred by the Gibbs free energy changes ΔG through Equation 2-1,

$$\Delta G = -nFE^{e}_{cell} \qquad \text{Equation 2-1}$$

where E^{e}_{cell} is the equilibrium potential of the electrolysis cell; n is the number of electrons transferred in the reaction; F (96485 C mol^{-1}) is the Faraday constant. The cell equilibrium potential can be calculated from the standard reduction potential of the cathode and anode half reaction by Equation 2-2.

$$E^{e}_{cell} = E^{e}_{cathode} - E^{e}_{anode} \qquad \text{Equation 2-2}$$

To make the electrolytic cell work, the overall potential E_{cell} needed is described by Equation 2-3,

$$E_{cell} = E^{e}_{cell} - |\eta| - |IR_s| \qquad \text{Equation 2-3}$$

where η is the overpotential, which has its origin in kinetic barriers that exist; IR_s reflects resistive losses in solution, also called IR drop.

Figure 2-2 shows the schematic of a typical experimental electrochemical setup, which contains three electrodes, that are, a working electrode (WE), a reference electrode (RE), and a counter electrode (CE). The potential of WE is measured and controlled through its potential difference with RE, and the current only flows between WE and CE.

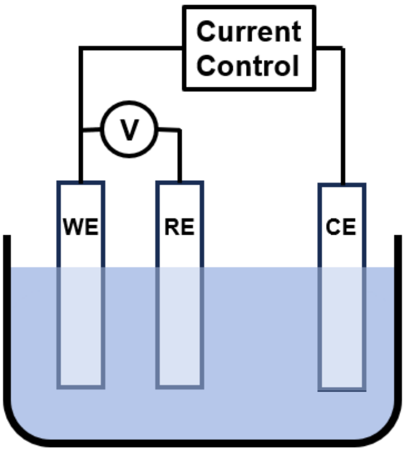

Figure 2-2. Schematic diagram of a typical the three-electrode electrochemical setup.

When no electrons are transferred externally, thus no conversion between O and R in the electrolyte could happen and the equilibrium potential E_e is reached. Taking the conversion from O to R as an example, the E_e can be described by the Nernst equation, Equation 2-4.

$$E_e = E_f + \frac{RT}{nF} ln \frac{C_O}{C_R} \qquad \text{Equation 2-4}$$

where E_f represents the formal potential; R (8.314 J K^{-1} mol^{-1}) is the universal ideal gas constant; and C_O and C_R represent the bulk concentration of O and R species (mol L^{-1}), respectively.

Theoretically, the Nernst equation should be expressed in terms of the activities of O and R rather than their concentrations. However, in practical applications, concentration is more accessible, but this is usually based on the premise that the O and R are dilute solutions and there is a large excess of inert supporting electrolyte.

During an electrochemical measurement, the potentiostat drives current from CE to WE until the potential difference between WE and RE reaches the desired value. The solution resistance is the origin of the IR drop, which will cause deviation of the applied potential to the desired potential and is usually unavoidable in practice. To accurately study the electrochemical process that happens on the WE, the system requires a stable RE, small solution resistance, and a negligible current (compared with the current caused by the electrochemical process of interest on WE) flowing between WE and RE.

Besides the Faradaic process discussed above, non-Faradaic processes also play an important role in electrochemistry. The non-Faradaic processes include all other phenomena where (typically capacitive) current flows but no redox change occurs, such as adsorption, double-layer charging, etc.

2-1.1 Electrochemical techniques

2-1.1.1 Chronoamperometry (CA)

Chronoamperometry (CA) measures the transient current changes caused by single potential step, and can also be called potential step experiments. In practice, the detected current response is affected by the double-layer charging in a very short period of time, and by the unavoidable convection caused by the environment in the long term. Thus, CA measurement is usually taken within 1 ms to 10 s.

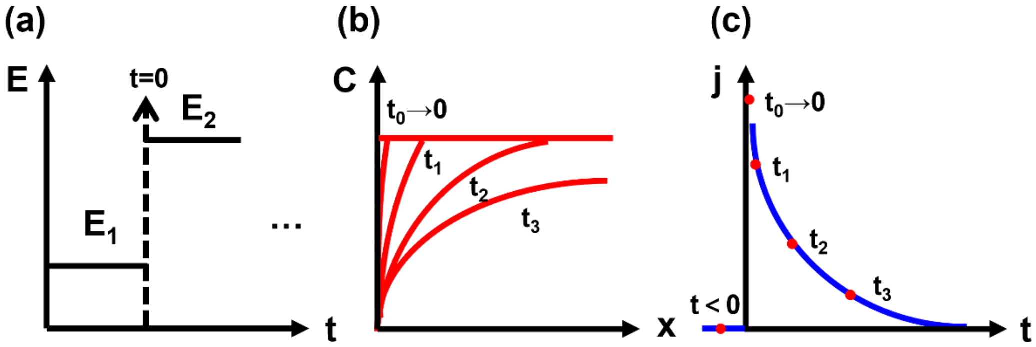

Figure 2-3. A CA measurement stepped from E_1 to E_2: (a) potential vs time; (b) concentration vs distance from the electrode surface at different times of the potential step measurement; (c) current response vs time.[69]

Figure 2-3 shows the process of a CA measurement when the potential is stepped from E_1, where no current is flowing, to E_2, which is a high potential that the conversion from the analyte to its product is only limited by diffusion. As soon as the potential is held at E_2, the analyte close to the electrode surface is all consumed and thus a large current is generated. Then, with the development of the diffusion layer, the current density decreases over time and can be described by the Cottrell equation, Equation 2-5,

$$j = \frac{nFD^{1/2}C}{\pi^{1/2}t^{1/2}} \qquad \text{Equation 2-5}$$

where j is the current density and D is the diffusion coefficient.

2-1.1.2 Cyclic voltammetry (CV) and linear sweep voltammetry (LSV)

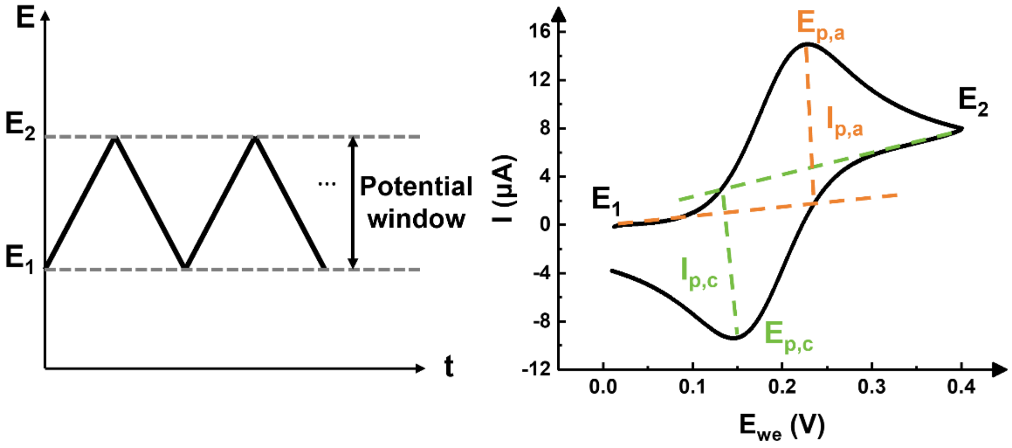

Figure 2-4. Potential applied during cyclic voltammetry (left) and typical current response (right).

Linear sweep voltammetry (LSV) and cyclic voltammetry (CV) are widely used electrochemical techniques for studying electrode processes. While LSV applies only the potential from E_1 to E_2, CV also includes the reverse scan, Figure 2-4. The current response is then detected and plotted as a function of the applied potential. E_1 is often chosen at a potential where no redox reaction of interest is happening. Ideally, with the potential scanned toward E_2, the oxidation/reduction current of the analytes grows exponentially until its peak value (I_p at E_p). After that, the diffusion becomes the rate-limiting factor and thus the current decreases.

In a system where electron transfer is much faster than mass transport of the analyte (i.e. mass transport is the rate-limiting factor), the reaction is called reversible. At room temperature, the peak current I_p (A) can be described by the Randles-Sevcik equation, Equation 2-6,

$$I_p = 2.69 \times 10^5 n^{3/2} A D^{1/2} C v^{1/2} \qquad \text{Equation 2-6}$$

where the numeric factor 2.69×10^5 has the unit of C mol^{-1} V$^{-1/2}$; A is the electrode area (cm^2); D is the diffusion coefficient (cm^2 s^{-1}) and C is the concentration (mol cm^{-3}) of the analyte; v is the scan rate (V s^{-1}). The relationship between the potential and concentration of the analyte and its product can be predicted by the Nernst equation.

When the electron transfer is the rate-limiting factor, the reaction is quasi-reversible or irreversible, the peak shape and position in a CV measurement will then be distorted.

2-1.1.3 Electrochemical impedance spectroscopy (EIS)

Electrochemical impedance spectroscopy (EIS) is an alternative current (AC) technique.[70] By applying a sinusoidal wave of potential or current at given frequencies, different processes at the electrochemical interface will perturb the input signal (the magnitude, phase angle, etc.) differently. Two types of EIS techniques are commonly used, these are, potentiostatic EIS and galvanostatic EIS. The former applies a potential, Equation 2-7, and detects the current response, Equation 2-8, while the latter is reversed,

$$E(t) = E_0 cos\,(\omega t) \qquad \text{Equation 2-7}$$

$$I(t) = I_0 cos\,(\omega t - \emptyset) \qquad \text{Equation 2-8}$$

where E_0 and I_0 are the sinusoidal wave amplitude; ω is the angular frequency; $\emptyset$ is the phase shift (or phase angle). An EIS measurement usually consists of inputting a series of sinusoidal waves that are centred around the given value with constant amplitude but different frequencies.

Once the EIS data is collected, it is essential to fit the data into an equivalent circuit that has real physical meanings. Then, the parameters for the electrochemical reactions can be extracted. The circuit elements used in this thesis and their meaning are summarized in Table 2-1.

Table 2-1. Summary of commonly used circuit elements in electrochemical impedance spectroscopy.

Element	Description	Impedance
Resistor (R)	Faradic processes through the interface	$Z_R = R$
Capacitor (C)	Usually represents the non-Faradic processes, such as electrochemical double layer charging, etc.	$Z_C = \frac{1}{j\omega C}$
Constant phase element (CPE or Q)	Non-ideal capacitor	$Z_{CPE} = \frac{1}{(j\omega)^{\alpha} Q}$
Warburg element (W)	Usually associate with the movement of electrons or ions in the solid or liquid phase	$Z_{CPE} = \frac{W}{(j\omega)^{0.5}}$

2-1.2 Mass transport in electrochemistry

In electrochemistry, the movement of analytes is controlled by three types of mass transport: 1) diffusion, which is driven by the concentration gradient; 2) convection, from mechanical forces such as the vibration of the solution; 3) migration, caused by the potential gradient. In typical analytical electrochemistry, migration is negligible because a large excess of an inert supporting electrolyte is present (1-2 orders of magnitude more concentrated than the analytes), so that the supporting electrolytes' ions will carry the charge through the solution. Therefore, either diffusion-only or convection-dominated mass transport is considered in analytical electrochemistry.[71]

In stationary electrochemical analytical techniques, diffusion is the only way of mass transport. Linear diffusion on a planar electrode is the most common model for such experiments, where the electrode is assumed to be completely flat and of infinite size on an atomic scale, so that the concentration gradient only occurs in the direction perpendicular to the electrode surface. Fick's first law is used to quantitatively describe linear diffusion, Equation 2-9.

$$Flux = -D\frac{dC}{dx}$$ Equation 2-9

where flux refers to the rate of diffusion (mol cm^{-2} s^{-1}); D is the diffusion coefficient (cm^2 s^{-1}) and the minus sign indicates the analyte diffuses from concentrated to diluted region; C is the concentration (mol L^{-1}); and x is the distance from the electrode surface. The D value in aqueous solution is usually around 10^{-5} cm^2 s^{-1}.

In electrochemical processes, the flux of oxidative species (O) into the surface must be accompanied by an equal amount of reductive species (R) flux leaving the surface and n electrons transfer, or vice versa. Thus, the fluxes of electrons, O, and R at the electrode can be described by Equation 2-10,

$$\frac{j}{nF} = D_R(\frac{\partial C_R}{\partial x})_{x=0} = -D_O(\frac{\partial C_O}{\partial x})_{x=0}$$ Equation 2-10

where j is the current density (A cm^{-2}).

2-1.3 Rotating disc and rotating ring-disc electrode (RDE/RRDE)

2-1.3.1 Working principle

For long-term steady-state measurements, the effect of convection on the electrochemical signal cannot be ignored, because even unstirred solutions can be affected by slight changes in the environment, such as thermal gradients or vibrations. Therefore, forced convection to achieve well-defined mass transport is preferred.

One of the most classical electrochemical techniques with forced convection is the rotating (ring-)disc electrode (RDE or RRDE),[71–73] Figure 2-5. During measurements, the electrode is rotating, so that a flux perpendicularly toward the disc electrode is derived. The species A from the bulk electrolyte is then oxidised/reduced to species B on the disc electrode. After that, the flux is thrown off and moves past the ring electrode (in the case of RRDE) that is surrounding the disc but separated by an insulator, and species B is oxidised/reduced to species C (note that in the simplest systems, species A and C are identical). Finally, species B (for RDE) or C (for RRDE) is circulated into the bulk electrolyte. At a stationary electrode, the thickness of the diffusion layer changes all the time, while at RDE/RRDE, the electrode generates a Nernst diffusion layer of constant thickness, so that diffusion through it is time-independent, thus yielding a steady state.

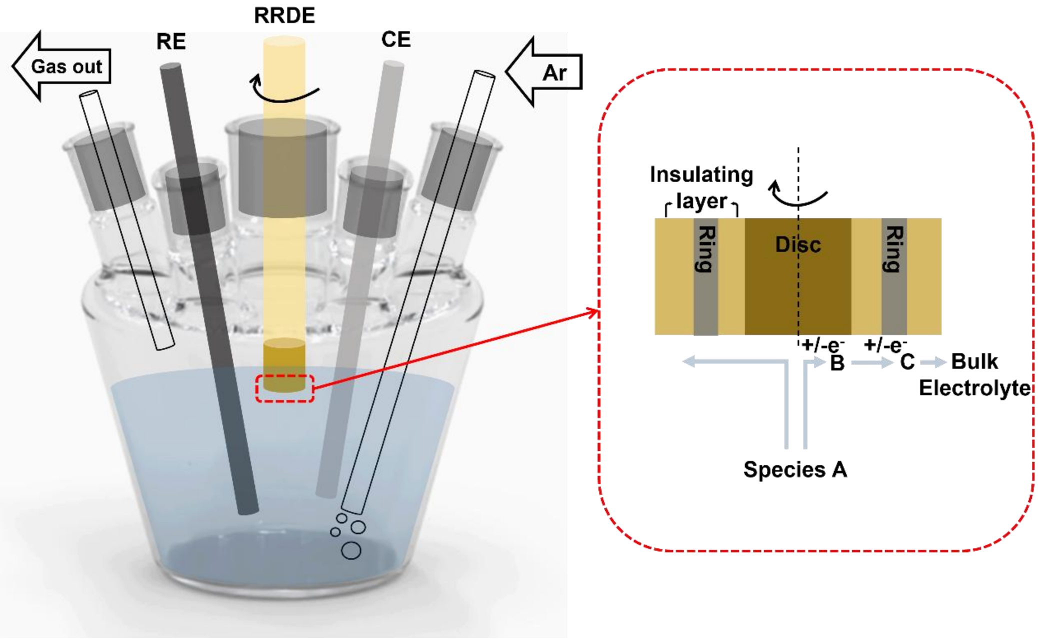

Figure 2-5. Schematic diagram of the working principle of a RDE or RRDE. Similar to other electrochemical techniques, RRDE experiments are usually performed under the protection of an inert atmosphere (such as Ar), or can be performed in other desired atmospheres as well.

Compared with RDE, RRDE adds a ring electrode concentric with the disc electrode to surround the disc. Such design enables the detection of the products from the disc electrode processes.

The time for the disc reaction products to travel from the disc to the ring is determined by the rotation rate of the electrode. Assuming the products are stable enough, the ratio of the products from the disc reaction that can be detected by the ring electrode (i.e. collection efficiency $N_{theoretical}$) is determined only by the geometrical parameters of the disc and the ring. Therefore, $N_{theoretical}$ can be predicted by the geometry of the RRDE.[74] While the $N_{apparent}$ can be observed from the disc and ring current, Equation 2-11.

$$N_{apparent} = -\frac{I_{ring}}{I_{disc}} \qquad \text{Equation 2-11}$$

Typically, the disc electrode can be subjected to voltammetry techniques, while the ring is usually held at a potential desired for oxidising or reducing certain species.

Nernst diffusion layer model is usually used to describe the mass transport in RDE/RRDE. Figure 2-6 shows the concentration distribution of O for the example of the reducing process from O to R, where the bulk solution contains only O.

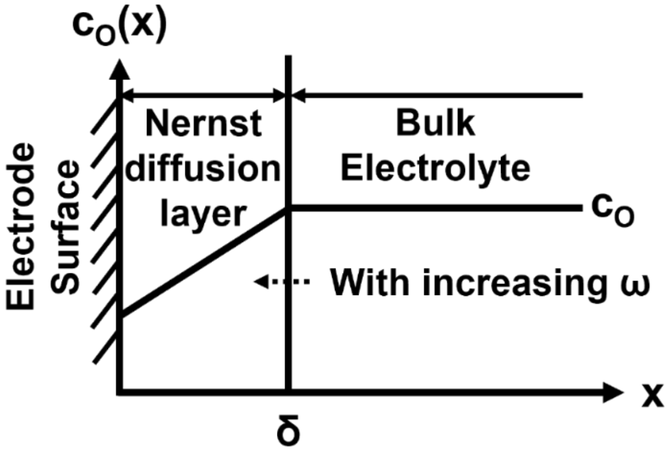

Figure 2-6. The Nernst diffusion later model in a RDE or RRDE system, taking the reducing process from O to R as the example.

When getting closer to the electrode, there is a hydrodynamic boundary layer with a thickness of δ_H, Equation 2-12, where the solution is stagnant relative to the electrode, so diffusion is the only way of mass transport.

$$\delta_H = 3.6(\frac{v}{\omega})^{1/2} \qquad \text{Equation 2-12}$$

where v is the kinematic viscosity (i.e. viscosity/density) of the electrolyte and ω is the angular rotation speed (rad s^{-1}) that can be converted from f (i.e. the rotation rate in revolutions per minute (RPM)) by Equation 2-13.

$$\omega = \frac{2\pi f}{60} \qquad \text{Equation 2-13}$$

The δ_H value for aqueous electrolytes with moderate rotation speeds is usually around 300-400 µm. Within this stagnant layer, diffusion dominates the mass transfer of the analytes to the electrode and the thickness of this diffusion layer δ can be described by Equation 2-14.

$$\delta = \frac{1.61 v^{1/6} D^{1/3}}{\omega^{1/2}} \qquad \text{Equation 2-14}$$

For ions or molecules with a typical D value (~10^{-5} cm s^{-1}), the diffusion layer in aqueous solutions is usually about 5% of the thickness of the hydrodynamic boundary layer.

Notably, the electrochemical response is dependent on the rotating rate of the electrode since the δ can be thinned by increasing ω. Thus, with increasing ω, more flux of analytes is transported to the electrode, which will then result in a larger current density.

When a sufficient overpotential is applied to the electrode surface, all the analytes near the electrode will be reacted, and the current density at this time is independent of the potential but related to the mass transfer rate, reaching the steady state. This also leads to the sigmoidal shape current response when applying voltammetry to the rotating electrode.

At steady-state (i.e. after the current reaching the plateau), the limiting current density $I_{lim,disc}$ on the disc electrode can be described by Levich equation,[73,75] Equation 2-15, taking the process of reducing O to R and only O exists in the electrolyte as an example,

$$I_{lim,disc} = 0.62nFAD_O^{2/3}\nu^{-1/6}\omega^{1/2}\,c_O$$ Equation 2-15

where A is the surface area of the disc electrode. The mass transport parameters, such as D, can be elucidated by the Levich equation.

Furthermore, the Koutechy-Levich equation[76, 158] can be employed to describe the current before reaching the plateau, which is limited by not only mass transport but also kinetics of the reaction, Equation 2-16,

$$\frac{1}{I} = \frac{1}{I_k} + \frac{1}{I_{lim,disc}}$$ Equation 2-16

where I_k is the kinetic current. Notably, the Koutechy-Levich equation is only valid for sluggish reactions, which have an electron transfer rate constant k^0 up to 10^{-2} cm s^{-1}. Otherwise, the electron transfer number n will no longer be independent of the potential.

2-1.3.2 Setup validation by hexacyanoferrate (II)/(III) redox couple

The RRDE used in this thesis is an E6R1 ChangeDisk RRDE from Pine Research Instrumentation, which is fitted with an interchangeable glassy carbon (GC) disc electrode (OD=5.0 mm), a Pt ring electrode (ID=6.5 mm, OD=7.5 mm), and a PTFE shroud. The $N_{theoretical}$ of this electrode based on its geometry is 25%, and its $N_{apparent}$ is validated by the hexacyanoferrate (II)/(III) redox pair, Figure 2-7.

As shown in Figure 2-7(a), sigmoidal curves are found for the disc current at all rotation rates, and the limiting current grows linearly with the square root of the rotation rate, Figure 2-7(c), meaning that the process is only controlled by mass transportation at high enough potential. The $N_{apparent}$ is approximately 28.3±0.4% for this RRDE, Figure 2-7(b). The slight decrease of $N_{apparent}$ when rotating faster may result from the sequence of the measurements, as Pt is easily poisoned over time. Uneven wear of the electrode during mechanical polishing is likely the reason causing $N_{apparent}$ to be slightly higher than the $N_{theoretical}$ of this electrode.

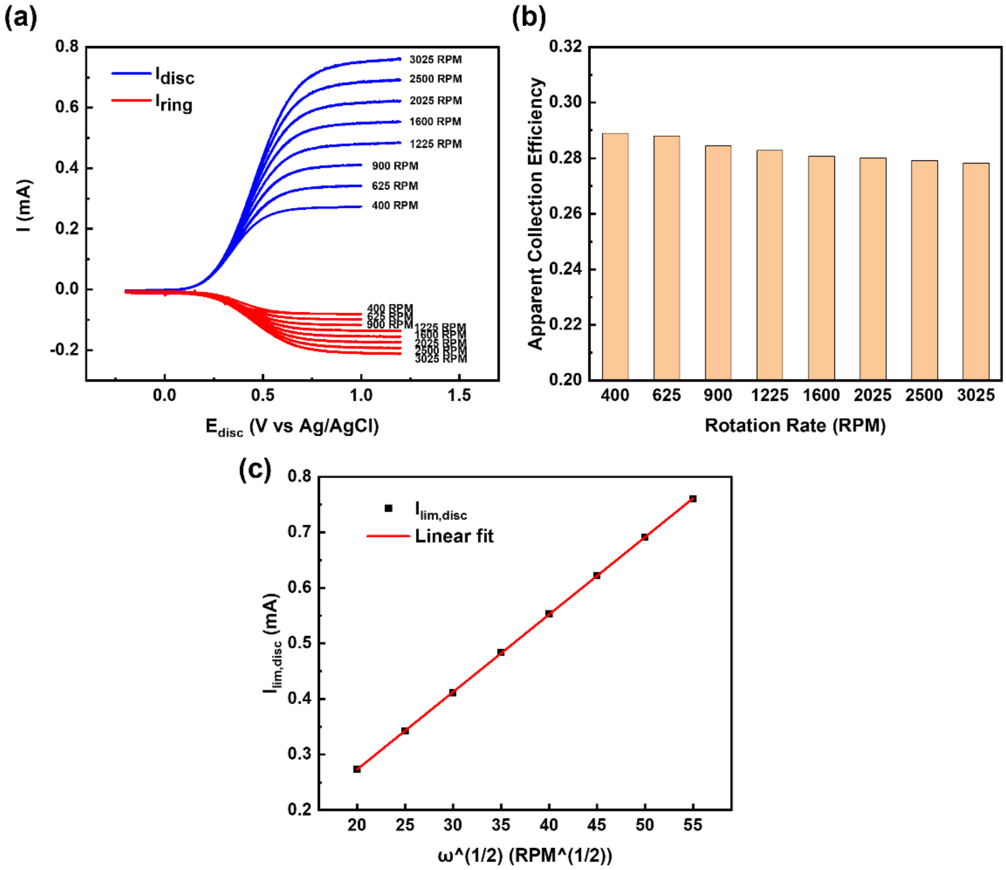

Figure 2-7. (a) Rotating Pt ring-GC disc voltammograms in 5 mM $[Fe(CN)_6]^{4-}$ + 0.1 M Na_2SO_4. Scan rate: 50 mV s^{-1}. (b) $N_{apparent}$ of the RRDE. (c) Limiting current on disc vs square root of the rotation rate.

2-1.3.3 Experimental details

The RE used for the hexacyanoferrate couple experiments was a conventional Ag/AgCl/3 M NaCl electrode. The CE was a Pt coil electrode. All the glassware was cleaned using boiling nitric acid 20% (diluted from >65% reagent grade, Sigma-Aldrich), which was then rinsed thoroughly with ultrapure water. A BioLogic BP-300 potentiostat was used for the electrochemical measurements. The electrolyte was prepared dissolving proper amount of Na_2SO_4 powder into ultrapure water (MilliQ, Millipore, 18.2 MOhm cm, total organic carbon < 2 ppb).

For all the measurements in this thesis, before each measurement, the RRDE was polished by 1.0 and 0.05 µm homogenized alumina suspension (Buehler), followed by a thorough rinse with ultrapure water and drying by N_2. To ensure the surface state is identical for each measurement (i.e. all the products from the previous measurements and/or any residues from the polishing agent were successfully removed), a CV was applied in the blank supporting electrolyte solution for both the GC disc and Pt ring once polished, Figure 2-8.

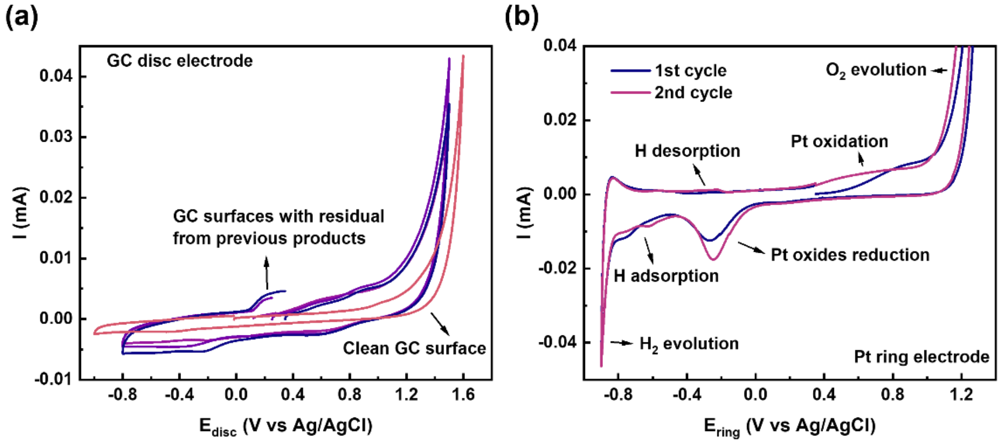

Figure 2-8. CV curves for checking the surface state of the disc and ring electrode of the RRDE: (a) for the GC disc electrode and (b) for the Pt ring electrode.[77] Electrolyte: 0.2 M Li_2SO_4. RE: Ag/AgCl/3.4 M KCl. CE: Pt.

No electrochemical reaction is expected on the GC disc electrode in the potential range of interest in this study except for the onset of the oxygen evolution reaction when the potential is scanned to above ~1.2 V. As shown in Figure 2-8(a), the lightest trace shows the CV for a clean GC surface. Thus, any current peak or shoulder on the CV curve suggests residue from the previous measurements (i.e. for the study in this thesis, Mn oxides) and requires further polishing (from the darker curve to the lighter curve in Figure 2-8(a)). In the case that polishing cannot help, acidifying the electrolyte could help to remove those residues.

As for the Pt ring, the onset potential of Pt oxidation and the peak potential for the subsequent reduction is different in the 1st cycle and the following cycles, Figure 2-8(b), which probably results from a different ratio of facets exposed on the polycrystalline Pt. Besides, the freshly polished Pt surface is less sensitive for Mn detection and speciation study in Chapter 4.

Therefore, a CV can not only check if the Pt surface is properly cleaned but also ensure identical sensitivity to elements in different measurements.

2-2 Online inductively coupled plasma-optical emission spectroscopy (ICP-OES)

2-2.1 Working principle

Inductively coupled plasma-optical emission spectrometry (ICP-OES) is a powerful technique for elemental detection. In recent decades, it has been widely used and developed for environmental, pharmaceutical, plant, etc. industries thanks to its excellent efficiency and sensitivity. It can reach the sub-parts per million (sub-ppm) level detection limit for most elements from the periodic table that can be dissolved in a liquid. Compared with other element analysis techniques, ICP-OES has advantages in its wide linear dynamic range, free of chemical interferences, enhanced efficiency of analysis, and multi-elemental capability.[78]

After the targeted solution is induced into the instrument, it is heated up by the ICP part of the instrument to 10,000 kelvin. Then, the molecules in the sample are broken down into individual atoms and/or ions, followed by excitation. Subsequently, when the excited electrons of the atoms and/or ions return to their ground states, they emit light with characteristic wavelengths, which is then detected and analyzed by the OES of the instrument. The intensity of the signals corresponds to the concentration of the elements.[79]

2-2.2 ICP-OES Components

An ICP-OES consists of the following parts:[78–81]

2-2.2.1 Nebulizer

The sample solution is introduced by the peristatic pump and reaches the nebulizer, where it is converted to an aerosol mist. This step enables the sample to be desolvated, vaporized, atomized, and ionized later in a homogenous manner. It is essential since the size and the size distribution of the droplets in the aerosol play a critical role in a stable measurement. [81]

One of the most widely used nebulizers is the concentric nebulizer. This type of nebulizer has an outer tube, where the gas can flow through, and an inner tube with a fine nozzle tip, where the liquid is carried, and is usually designed based on Bernoulli's principle, Figure 2-9. The gas from the outer tube creates a low-pressure area at the tip of the inner tube, resulting in turbulence generation when the liquid is mixed with the gas, which is then dispersed into the aerosol. Therefore, the tube size, the flow rate of the carrier gas and the liquid sample, and the physical properties of the liquid are all important for the formation of the aerosol. Besides, small precipitation may be formed and accumulated at the nozzle tip of the inner tube, which may block the tube and terminate the measurement. Thus, the total dissolved solids (TDS) are usually limited by the tube size. When measuring samples with high TDS values, a strategy to mitigate the blockage caused by the precipitations is to humidify the carrier gas by passing it through ultrapure water prior to flowing it to the nebulizer.

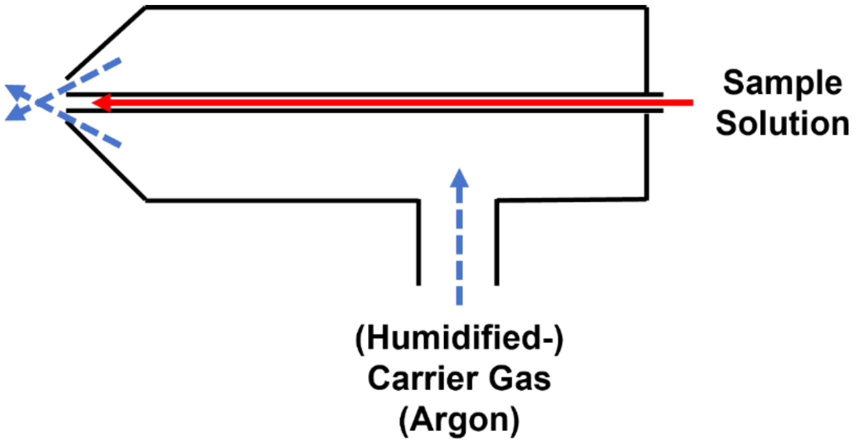

Figure 2-9. Schematic diagram of the concentric nebulizer.

Compared with the concentric nebulizer, the cross flow nebulizer is easier to make but creates a larger mist. Other types of nebulizers include V-Groove, Thin Film, Hildebrand Grid and Parallel Path designs, where a pump or gravity feed is usually needed for sample delivery since they have neither suction nor back pressure. Another commercially available alternative is the flow blurring nebulizer, which creates smaller droplets by introducing the liquid into the gas stream by pressure, and is capable of high TDS samples.[80,82]

2-2.2.2 Spray chamber

The resulting aerosol is then sent to the spray chamber. The Spray chamber can not only connect the nebulizer with the torch but also filter the large droplets. Commonly used spray chamber types include cyclonic chamber and Scott double pass chamber, where the former can deliver approximately twice as much sample as the latter and thus tends to be twice as sensitive, while the latter tends to give sample flows with lower relative standard deviation.[81]

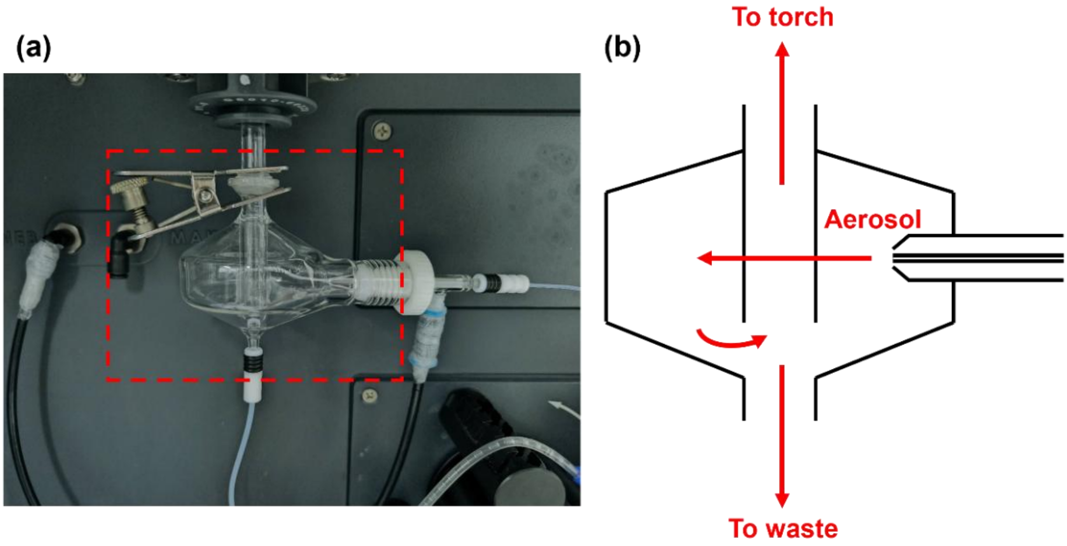

Figure 2-10. The cyclonic spray chamber. (a) A photograph of part of the sample introduction system fitted for the ICP-OES used in this thesis, the red rectangle highlighted the spray chamber; (b) Schematic diagram of the working principle of the cyclonic spray chamber.

Figure 2-10 shows the photograph of the cyclonic spray chamber fitted with the ICP-OES used in this thesis and a schematic diagram of its working principle. Once the aerosol reaches the spray chamber, it is forced into a vortex pathway and sent to the torch on the top of the chamber, while the excess sample with deviated droplet size is collected by the waste, so that the stability of the plasma can be increased. In general, up to 70% of the sample solution is sent to the waste, thus, it has to be removed effectively or excess liquid entering the torch may cause the plasma to extinguish.

Most spray chambers are made from borosilicate glass to limit the cost, which works fine for most mild aqueous solutions. Some corrosive acids such as HF may corrode the spray chambers and introduce impurities from the chamber to the sample. Chamber made from other materials, such as polypropylene (PP), polytetrafluoroethylene (PTFE), etc., are also available for harsh samples, such as Si-containing, HF-containing, organic, etc. samples.[81,83,84]

2-2.2.3 Torch

The torch has a similar structure and working principle to the concentric nebulizer, but has one more layer of tube. The Ar gas in the outer tube, which is usually 7-18 L min^{-1}, is mainly for cooling down the torch to prevent it from melting by the plasma while enabling the emission of the sample elements. The Ar gas flow in the intermediate tube (0-2 L min^{-1}, also called auxiliary flow) helps position the plasma. The Ar gas flow in the inner capillary tube is usually 0.5-1.5 L min^{-1}. [78,79] The pressure differences on the top of the torch create a constant and homogenous driving force that draws up the aerosol from the spray chamber, allowing smooth signals.

Ar ICP has always been used as the main source of OES because it is mono-atomic, so it has low spectral interference as its own spectrum is simple. Moreover, Ar has high ionization energy (15.76 eV), thus it can atomize, excite, and ionize most elements in the periodic table while chemically inert with them. It is also cheaper compared with other noble gases.[85–87] The sizes of both tubes and the Ar flow rate are designed to provide a constant and smooth driving force for the aerosol. These two factors, together with the physical properties of the aerosol, determine the amount of sample aspirated.[79]

2-2.2.4 Plasma generation

After the mixture of the Ar gas and aerosol reaches the top of the torch, it is ionized by a brief ignition spark. The top of the torch is surrounded by the radio frequency (RF) coil, where a high-frequency alternating current is supplied to generate an electromagnetic field that can maintain the ignition of the plasma at a constant temperature, Figure 2-11. The power of the RF coil should be optimized in consideration of the elements of interest based on their ionization energies. The Ar gas flow in the outer tube needs to be increased to effectively cool down the torch when the targeting elements have high ionization energies, where a high RF power is needed. While the RF power needs to be lowered to reduce the background signal when the targeting elements require low ionization energy. Besides, the RF power also requires adjustment according to the sample introducing rate. [88]

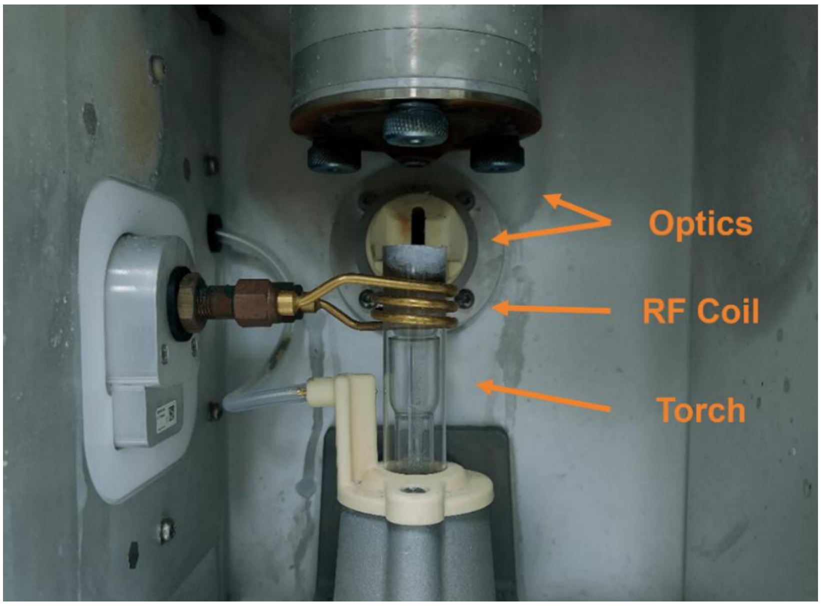

Figure 2-11. A photograph of the top half of the torch, the RF coil, and the optics.

2-2.2.5 Optics

The emission of the elements in the sample can usually be observed by axial or radial viewing, Figure 2-12, the former has a better detection limit and the latter provides better sensitivity. For the axial mode, all emission signals are collected from the top, while the radial mode requires careful positioning of where the spectrum is taken, because the temperature gradient in the plasma will cause different spectral intensity gradients for different elements.

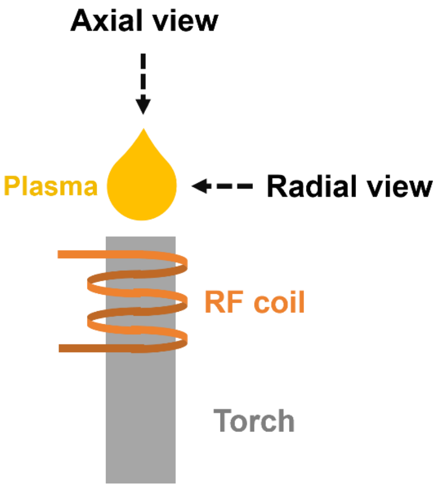

Figure 2-12. Schematic diagram of the axial and radial viewing configuration.

2-2.2.6 Spectrometer and detector

Once the optic has collected the emissions, the spectrometer then disperses them into their component wavelengths, to distinguish each of the elements and/or the interferences, and focuses them on the detector for further analyses. After that, the emission is observed either by a monochromator, which is flexible to measure any single wavelength of interest but requires complex background correction, or a polychromator, which is able to measure a wide wavelength range at once but is limited by the number of available spectral lines. [78,85]

The Agilent ICP-OES 5100 ICP-OES used in this thesis is fitted with a charge-coupled device (CCD) detector, which consists of a large number of light-sensitive small sensors known as the pixel array. Each pixel can detect a single wavelength, which can then be assembled as an image of the interested area. Therefore, the CCD detector is essential for multielement detection and/or the observation of several wavelength for a single element for a more accurate measurement.

2-2.2.7 Signal acquisition

The signal acquisition in this thesis is completed by ICP Expert software (version 7.4.2). Similar to other spectroscopy techniques, the signal acquisition time as well as replication needs to be optimized based on the signal-to-noise ratio and in consideration of a reasonable time resolution for online measurements. For routine offline measurement, a read time of around 30 seconds with 3-5 replicates is recommended. For online measurement, a read time of 1 second without any replicate is used in this thesis for giving the correlation of element dissolution while doing electrochemistry.

2-2.2.8 Element concentration calibration and the detection limit

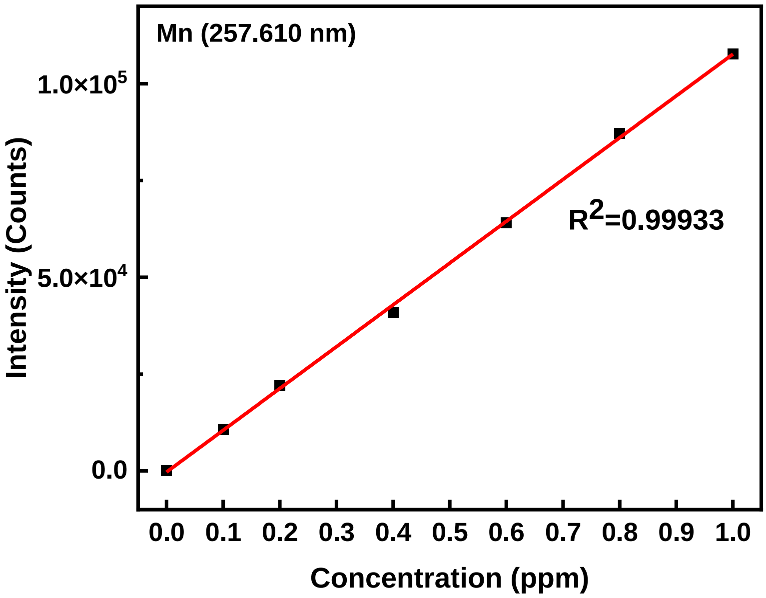

Figure 2-13. Concentration calibration for Mn observation at 257.610 nm wavelength in a 0.2 M Li_2SO_4 aqueous solution with a 1.5 mL min^{-1} flow rate. As the relative atomic mass of Mn is 55.94 g mol^{-1}, 1 ppm Mn = 17.88 µmol L^{-1} Mn.

A correlation between the observed intensity and the concentration of the element is essential for quantitative analysis. Thus, a series of standard solutions of known concentrations covering the range of expected sample concentrations to be measured are prepared. The intensity of the elements in the standard solutions should be linearly dependent on the concentration, Figure 2-13.

For online measurements that are longer than 30 minutes, it is advisable to monitor the standard solutions before and after the online measurement to adjust for changes in the sensitivity of the instrument. During the measurement, some elements that have low solubility in the required aqueous matrix may be deposited on the wall of the sample inlet components (i.e., tubing, nebulizer, and spray chamber). In offline measurements, the trace deposits are usually negligible. However, in online measurements, on the one hand, this will cause the sample concentration reaching the torch to be noticeably lower than its actual concentration. On the other hand, due to the accumulation of deposits, the sample introduction system may no longer be able to generate homogeneous and stable aerosol, which will further affect the accuracy of the measurement.

Each STD is measured for at least 30 seconds and their average value is taken. By plotting the intensity versus concentration, a linear trendline can be yielded from the regression fitting, Equation 2-17,

$$\text{Intensity} = \text{slope} \times C + \text{y-intercept} \qquad \text{Equation 2-17}$$

where the Intensity is the raw signal read by the instrument in counts and C is the concentration is in ppm.

From the STD, the limit of detection (LoD) can also be estimated by Equation 2-18,[89]

$$\text{LoD} = \text{Standard deviation of the blank} \times 3 \qquad \text{Equation 2-18}$$

2-2.3 Online ICP-OES configuration

The online ICP-OES system setup consists of three parts: the electrolyte reservoir, the electrochemical flow cell, and the ICP-OES, Figure 2-14. The ICP-OES is discussed in the previous section, and the other two parts are discussed in the following sections.

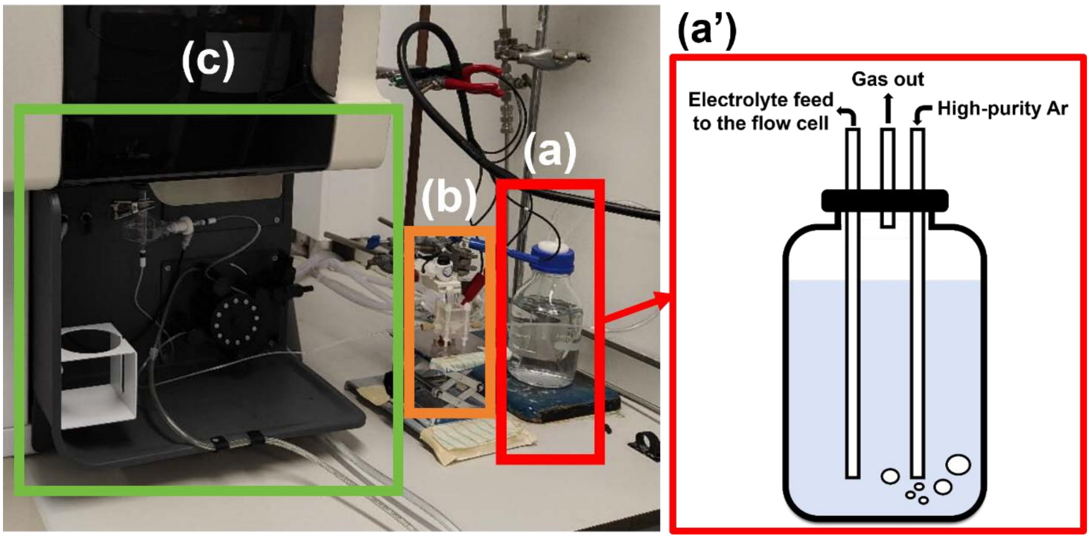

Figure 2-14. Online ICP-OES setup. (a) The electrolyte reservoir, and (a') schematic diagram; (b) The electrochemical flow cell; (c) The sample inlet of ICP-OES.

2-2.3.1 Electrolyte reservoir

The electrolyte reservoir stores the fresh electrolyte, where the electrolyte is sparged by high-purity Ar (99.999%) to remove oxygen. The group previously developed a suspended reservoir for the droplet-type flow cell, where the inlet flow rate of the flow cell is controlled by hydrostatic pressure together with a needle valve located between the reservoir and the flow cell. While the flow cell outlet flow rate is adjusted by the peristaltic pump of ICP-OES. With such a configuration, the flow rate of the inlet and outlet need to be matched perfectly for a stable bubble-free electrolyte flow, which is essential for both electrochemistry and elemental detection.

A closed-type flow cell, which will be discussed later, is designed to access the samples with smaller surface areas and/or samples that cannot be prepared by drop-casting. In addition, better control of the electrolyte flows is desirable. For this closed-typed flow cell, a reservoir as presented in Figure 2-14(a') is used. The electrolyte is usually sparged by high-purity Ar from 5-10 min before until the end of the measurements. Once the reservoir is connected to the flow cell and the ICP-OES, the negative pressure generated by the peristaltic pump from the ICP-OES will draw the electrolyte, and thus no extra pump or overpressure is needed for feeding the electrolyte to the flow cell, and the alignment of the inlet and outlet flow rate is no longer needed.

2-2.3.2 Electrochemical flow cell design and optimization

The droplet-type flow cell (Type 1 flow cell) that was previously developed by the group is described in detail by Nikman.[90] A closed-type flow cell (Type 2 flow cell) was then designed based on a similar working principle but for the purpose of accessing more diverse samples, for better flow controls, and for better protection of the electrochemical reaction from the air once the electrolyte is sparged.

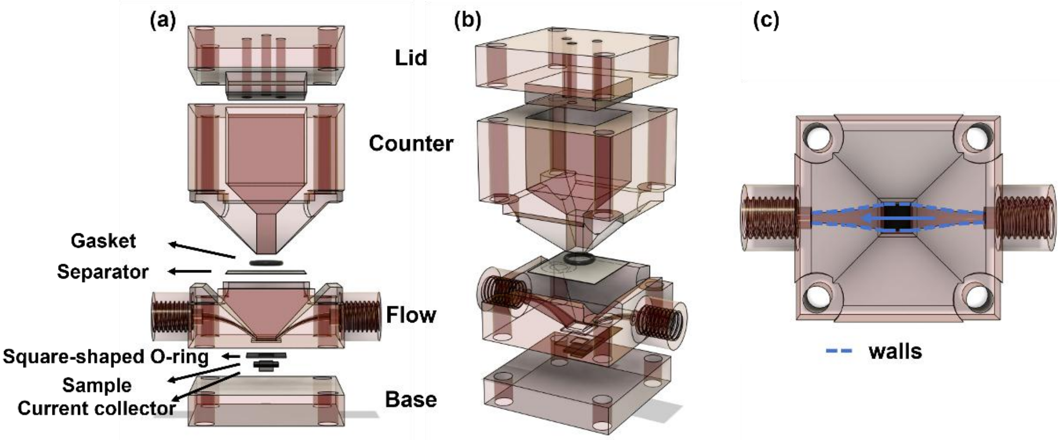

Figure 2-15. Different views of the initial close-type flow cell design and assembly. (a) Front view; (b) Side view; (c) Top view of the flow compartment, and the blue arrow indicates the electrolyte flows

The type 2 flow cell, as shown in Figure 2-15, consists of four parts: 1) the lid compartment, which can protect the electrolyte and electrodes in the counter compartment; 2) the counter compartment, where the reference electrode (RE) and counter electrode (CE) usually stay; 3) the flow compartment, where the fresh electrolyte can flow through to the sample (working electrode, WE) and to the ICP-OES after any electrochemistry; 4) the base compartment, which can sandwich the WE and the current collector with the flow compartment. Overall, the type 2 flow cell is designed to be $3 \times 3 \times 4$ cm^3 (L×W×H). The separator is placed in between the counter and flow compartments with the help of a gasket, where a Viton rubber O-ring is usually used thanks to its excellent chemical resistivity. Between the flow and base compartment, a square-shaped O-ring is made by parafilm to define a 0.3×0.3 cm^2 surface area of WE. A copper foil is placed at the back of the WE to act as a current collector. The electrolyte is transported by 1/8” (outer diameter, OD) and 1/16” (inner diameter, ID) perfluoroalkoxy (PFA) tubings to and from the flow cell. The tubings are connected to the flow cell by polyether ether ketone (PEEK) male nut.

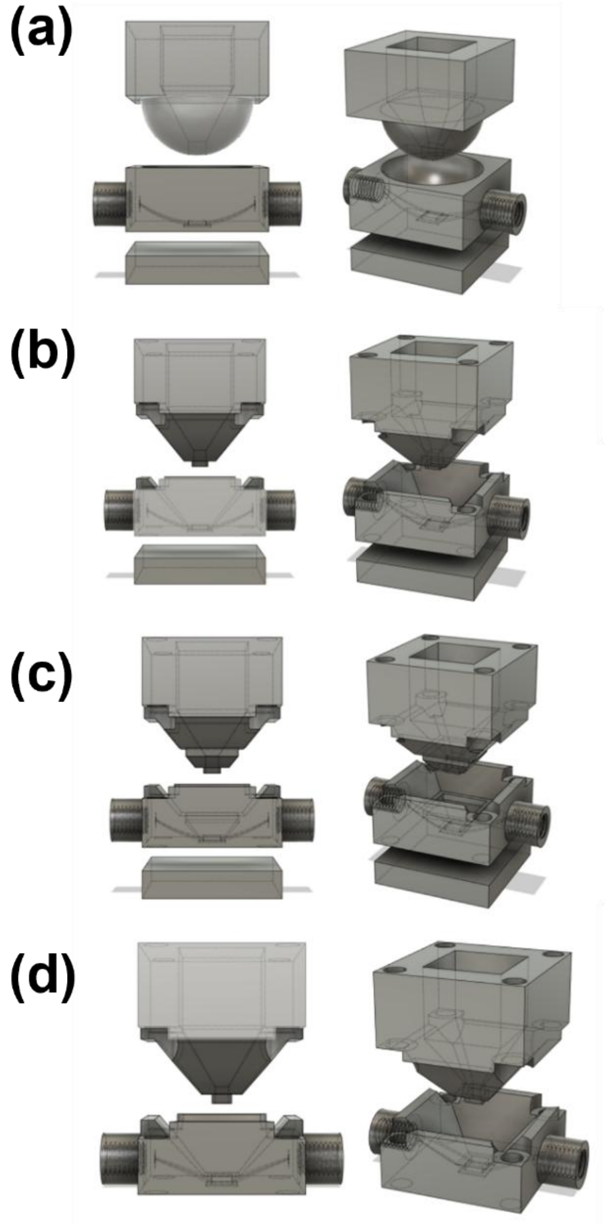

Figure 2-16. Optimization process of the flow cell design.

The assembled flow cell should be airtight so that the peristaltic pump from the ICP-OES can generate a negative pressure throughout the cell and tubing to drive the electrolyte. In order to achieve good airtightness and avoid damage to parts caused by sharp edges and corners of the compartments, the next version was designed with curved counter and flow compartments, Figure 2-16(a). However, due to the limited precision of 3D printing, it is often difficult for the two compartments to fit together. In the next versions of design, the pyramid-like connection between the flow and counter compartments was used again. In order to improve the airtightness of the flow cell, different numbers of gaskets were tried, and the shape of the space reserved for the gaskets was continuously optimized, so that the cell would not be easily broken due to inappropriate angle or thickness design, and the gasket would not be easily moved during installation or use, Figure 2-16(b)-(d).

2-2.3.3 3D printing and flow cell assembly

The 3D printer used for this thesis is a stereolithography (SLA) 3D printer called Form 2 which was purchased from Formlabs. The printer uses a 405 nm violet laser (250 mW) to cure the liquid resin and the laser spot size is 140 microns. Clear V4 resin that also bought from Formlabs was used for all the flow cells and the z-layer thickness during printing is 25 microns.

After printing is finished, all the cell parts are immersed in a reusable and a fresh isopropyl alcohol bath for 10 min each to clean the excessive resin. Then, use a N2 gun to dry the cell parts and check all the channels. Before assembling, all the surfaces of the cell are carefully polished with sandpaper (grits 1000-8000) to remove any uneven bits.

The Viton (fluorocarbon rubber polymers, FKM) O-ring that was purchased from Polymax UK is used when assembling the cell. The separator was a microporous polypropylene membrane (Celgard 3401). The reference electrode (RE) was Leak-Free Ag/AgCl/3.4 M KCl electrodes (Innovative Instruments) and the counter electrode (CE) was either Pt or Au coil depending on the electrochemical systems. The Cu current collector is a Li-ion battery grade Cu foil bought from TOB New Energy. The tubing and nuts are purchased from Cole-Parmer.

2-2.3.4 Time alignment of the potentiostat and ICP-OES and the design validation

Once the flow cell is assembled and connected with ICP-OES, a Zn pulse protocol with one-minute intervals, where a Zn foil is held at different potentials for several one-minute lengths to generate Zn^{2+} dissolution, Equation 2-19,[91] is used to align the timestamp of the potentiostat and ICP-OES:

$$\mathrm{Zn} \rightarrow \mathrm{Zn}^{2+}(\mathrm{aq}) + 2\mathrm{e}^{-} \qquad \text{Equation 2-19}$$

The Zn^{2+} concentration in the flowing electrolyte should have the same shape as that of the potential or current if the flow is ideal. By aligning the starting point of each step of the current signal and the dissolution signal, the delay caused by the tubing and the internal clock difference of the two instruments can be corrected, Figure 2-17.

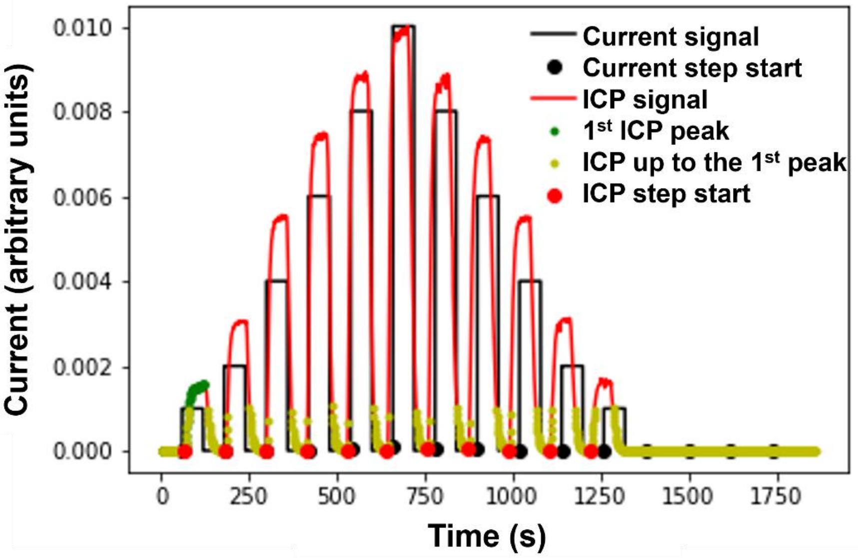

Figure 2-17. Time alignment of the potentiostat and the ICP-OES signals.

Besides, the Zn pulse protocol can also be used for the validation of the cell designs. Figure 2-18 shows representative results from the initial type 2 flow cell design, where the same Zn pulse protocol was used to generate soluble Zn, and the dissolutions were recorded at different flow rates. Ideally, the flow cell setup should allow detection of the square-wave concentration profile of Zn^{2+} in solution without any peak broadening or rounding of features. For the initial design, the squared shape signal of Zn concentration is only observable when the peristaltic pump speed is increased to 30 RPM and above, meaning that transport characteristics were far from ideal.

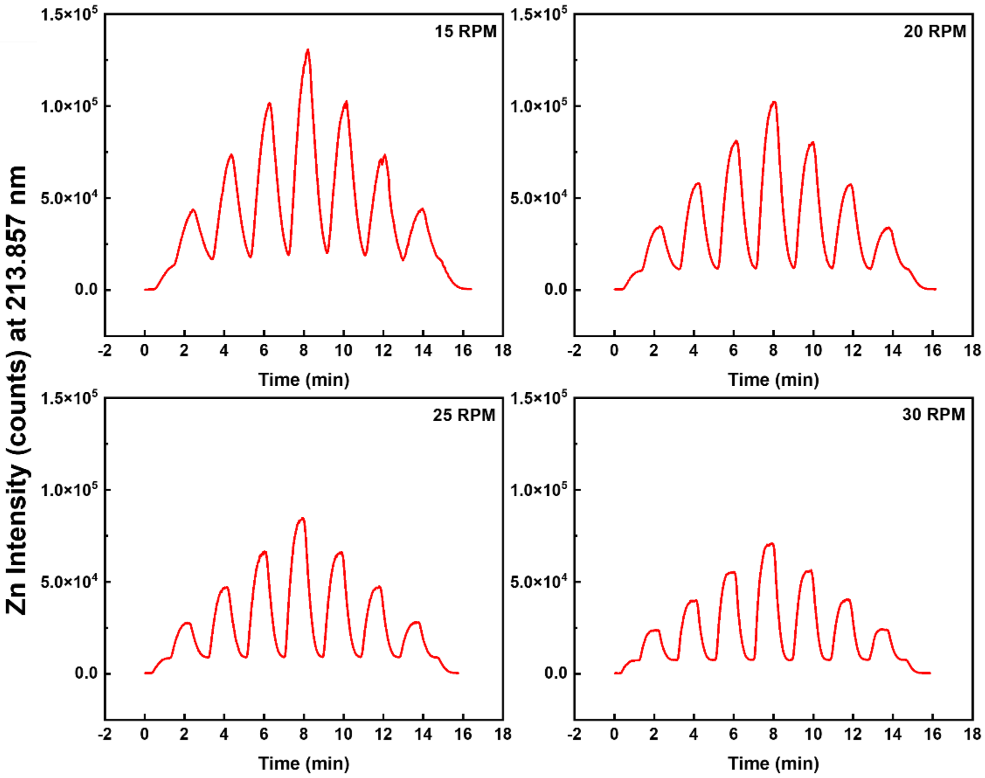

Figure 2-18. Signals of Zn dissolution detected at different flow rates, generated by the same Zn pulse protocol.

2-3 *Operando* Raman spectroscopy

2-3.1 Raman spectroscopy

When a substance is illuminated by a light, two types of scattering light can be generated, namely elastic scattering and inelastic scattering. The elastic scattering is also known as Rayleigh scattering, which means that the scattered light has the same frequency and wavelength as the incident light. Inelastic scattering, which is also known as Raman scattering, results in scattered light with different frequency and wavelength from the incident light. The latter occurs very rarely (once every 10^6-10^8 photons). Raman spectroscopy is non-destructively analyzing the Raman scattering of the substance to provide vibrational information on chemical bonds, structure, etc.[92]

The molecules can be excited by absorbing the light that has the same frequency as their vibration. If that happens, the light scattered off the molecule will have different energies from the incident light because of the absorbance, thus causing Raman scattering. Based on the original state of the bonds, two types of Raman scattering can happen. When the molecule is exited and comes back to a higher energy state, photons with lower energy than their original state are released, that is the Stokes scattering. Whereas when the photons have higher energy since the electron of the molecule relaxes to a lower vibrational level, an anti-Stokes scatter happens, Figure 2-19.

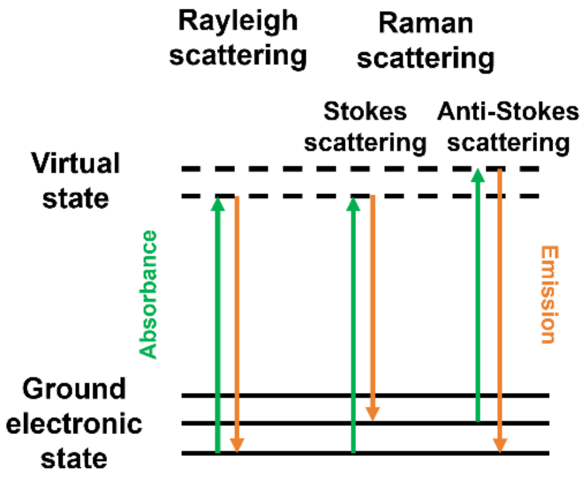

Figure 2-19. Schematic diagram of Rayleigh, Stokes Raman, and anti-Stokes Raman scattering.

The relative intensity of the Stokes and anti-Stokes scattering is determined by the Boltzmann distribution and symmetry selection rules. In general, Stokes scattering is more intense at room temperature, though anti-Stokes scatter is used to avoid interferences such as fluorescence.

In Raman spectroscopy, a monochromatic laser is usually used for generating the incident light beam, by detecting the frequency change (i.e. Raman shift) of the scattered light, the vibrational mode of the chemical bond can then be determined.

The Raman spectroscopy used in this thesis is a Renishaw inVia confocal Raman microscope that features 532 nm and 785 nm lasers, with 15 mW and 20 mW maximum power, respectively. The spectra are recorded by WiRE software and processed by SpectraGryph (version 1.2) software.

2-3.2 Operando setup

For the *operando* Raman spectroscopy measurements, an electrochemical optical cell (ECC-Opto-Std) from EL-CELL was used, Figure 2-20. The cell consists of (from top to bottom): 1) a stainless-steel lid, which can help close the cell and secure all components; 2) the sapphire optical window; 3) the Li metal (99.95%, China Energy Lithium Co., Ltd) with a hole that allows the laser to go through; 4) a glass fibre separator (Whatman) with a hole for the laser; 5) the cathode (WE) that coated on the Al foil (battery grade, TOB New Energy); 6) the PEEK cell body; 7) a Ni pin for the electrochemical control of the RE/CE; 8) the stainless-steel cell parts for the electrochemical signal of the WE. The cell was assembled in an Ar-filled glove box (O_2 and H_2O<0.1 ppm).

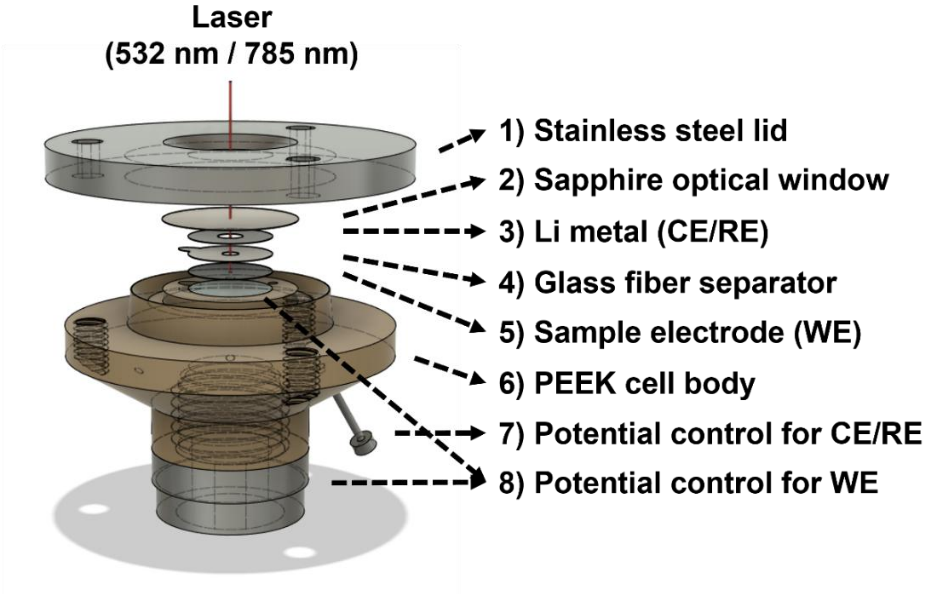

Figure 2-20. Electrochemical optical cell set up for *operando* Raman spectroscopy measurements.

Chapter 3. Real-time manganese dissolution detection in a lithium-ion cathode

Parts of the results in this chapter are published as:

Nikman, S., Zhao, D., Gonzalez-Perez, V., Hoster, H. E., & Mertens, S. F. L., Surface or bulk? Real-time manganese dissolution detection in a lithium-ion cathode. *Electrochimica Acta*, 2021, **386**, 138373. DOI: 10.1016/j.electacta.2021.138373.

In this chapter, we established online ICP-OES for real-time transition metal dissolution detection from a Li-ion battery cathode under various conditions. The longevity of lithium-ion batteries is determined by the rate of chemical and electrochemical side reactions that limit their charge storage capacity. In particular, dissolution of transition metals from the cathode accelerates the blockage of Li_xC_6 anodes, but few direct dissolution studies have been made to date. Although $LiMn_2O_4$ (LMO) has been frequently used as a model electrode for dissolution studies, the cause and nature of dissolution and dissolution-free states are still unclear. By online ICP analysis, we detect dissolution from LMO electrodes in real time to reveal the role of surface versus bulk structure effects, electrode potential and degree of lithiation on Mn dissolution. We find that fully lithiated LMO, with an average Mn redox state of 3.5, readily dissolves when brought in contact with 0.2 M Li_2SO_4, but that on initial charging a dissolution–passivation event preceding delithiation abruptly stops further detectable dissolution, until well past fully delithiated λ-MnO_2. Dissolution reactivates on returning to the initial potential of pristine LMO, and increases exponentially in the overlithiation region. Our results provide access to much more detailed dissolution information than post-mortem battery analysis allows, enabling targeted materials screening and informing best practices in charging/discharging profiles. In particular, our data suggests that suitable potential conditioning of electrodes may mitigate dissolution, as an alternative or additional measure to the use of protective surface films or incorporation of dopants.

I performed part of the experiments with the type 1 flow cell for initial Mn dissolution detection from LMO during cyclic voltammetry with wide potential windows in the neutral electrolyte. In order to better eliminate the effect of O_2 from air on the performance of LMO, I designed the type 2 flow cell. I also performed the pH dependence experiments to understand the dissolution mechanism further.

3-1 Introduction

Lithium-ion batteries have enabled a societal revolution since their entry to market in 1991.[93] Since then, incremental advances in capacity retention, power delivery capabilities and competitive pricing have permitted their implementation in consumer electronics, vehicles and intermittent grid storage.[94] In 2018 the global energy output was 162,820 TWh,[95] and is estimated to grow by 27% by 2040. However, the current deployed energy storage facilities amount to only 17 GWh, while the predicted demand for stationary and vehicle energy storage by 2040 is 4584 GWh.[96] If this growth is to be sustainable, the lifespan of deployed batteries should be as long as possible to reduce cost of replacement,[97] and environmental impact. The ultimate battery should only involve a single, fully reversible charge–discharge reaction, have minimal internal resistance and retain capacity indefinitely, i.e. not degrade chemically or electrochemically. Gains in battery longevity have been made by meticulous screening to find electrodes, electrolytes and solvents that decompose minimally.[98] Yet, due to a 4.2 V potential span, electrolyte and solvent still decompose to form a solid-electrolyte interphase (SEI) on the anode and a cathode-electrolyte interphase (CEI) on the cathode.[99–101]

While the SEI is an essential yet poorly understood part of a lithium-ion battery, dissolution of transition metal ions from the cathode leads to excessive SEI formation in what is known as the dissolution-migration-deposition (DMD) process, causing premature capacity fading and responsible for the majority of overall capacity loss.[33,102] CEI however, is not typically found in aqueous rechargeable alkali batteries,[103] which are greener and safer alternatives to flammable $LiPF_6$-containing electrolyte.[104] Although these aqueous batteries also store charge reversibly, and have recently gained significant research attention for affordable energy storage,[105] they also suffer from cathode dissolution mediated by acid formed by fluorine-containing electrolytes in non-aqueous systems.[106,107]

Detailed and accurate real-time data on the dissolution of electrode materials, under all relevant operating conditions, are critical in delivering numerous scientific and technological targets: (i) to better understand the various degradation processes that occur in batteries, as a function of time, potential and charging/discharging rate; (ii) to deepen the insight in SEI and/or CEI formation, function, and degradation; (iii) to propose alternative battery chemistries informed by fundamental understanding and less relying on trial and error; (iv) to inform "best practices" of battery charging and discharging to maximise lifetime; (v) to open an additional window on a battery's "state of health", diagnosing the effects of adverse events such as improper storage and charging/discharging; (vi) to quantify the impact of electrode modification, including the use of coatings, potential or other treatments, and artificial SEIs.

To date, battery electrode dissolution data are inferred by post-mortem analysis, which easily introduces errors due to multiple handling steps. More detrimentally, however, any time resolution is also lost, making the interpretation of signs of dissolution and correlation to charging/discharging history highly contrived. Recent examples include anode surface deposition mapping by LA-ICP-MS[53] and dissolved transition metal electrolyte characterization by total reflection X-ray fluorescence (TXRF),[108] where only the total lost cathode material per cycle is available. Direct observation of lithium-ion cathode dissolution has been limited to a few studies, based on rotating-ring-disk electrode (RRDE),[45] ultraviolet-visible (UV-vis) spectrometry,[42] and electron paramagnetic resonance (EPR) measurements,[47] but these methods suffer from limited selectivity and/or detection range. In an elegant recent paper, capillary electrophoresis showed remarkable ability to distinguish both element and oxidation state, and may therefore make a significant impact in upcoming battery degradation research.[41]

In this chapter, we present the first real-time dissolution study of the model cathode material $LiMn_2O_4$ (LMO) using an online flow cell- ICP-OES setup under potentiostatic and galvanostatic control. LMO dissolution has been studied previously using post-mortem approaches, leaving many important questions unanswered, including time resolution and potential dependence.[109] Online flow cell-ICP techniques, by contrast, make real-time dissolution observation possible and offer superior detection limits,[110,111] but they typically use aqueous solutions unless the sample introductory system is heavily modified. Our measurements are performed with aqueous 0.2 M lithium sulfate as electrolyte, mostly for compatibility reasons with the ICP torch. However, studying the dissolution of cathode materials not compounded by CEI formation-as is generally the case in organic electrolytes-may also lead to a clearer understanding of the intrinsic manganese dissolution processes.

3-2 Materials and methods

3-2.1 Materials

Titanium foil (99.995%) was obtained from Advent. As electrolyte, 2.0 M Li_2SO_4 (BioUltra, Merck) was diluted with ultrapure water (MilliQ, Millipore, 18.2 MOhm cm, total organic carbon < 2 ppb) to 0.2 M; this concentration is lower than in typical lab batteries (2 M), but its impact on achievable capacity and IR drop in aqueous solutions has been reported as minimal.[112] $LiMn_2O_4$ (LMO) powder (Mesh-325), dimethylsulfoxide (DMSO, ACS grade), Super-P carbon and polyvinylidene difluoride (PVDF) powder were obtained from Alfa Aesar. The ultrapure 96% H_2SO_4 from Supelco and 5 M aqueous NaOH from Sigma Aldrich were used for adjusting the pH of the electrolyte.

3-2.2 $LiMn_2O_4$ electrode preparation

LMO powder, Super-P carbon and PVDF were added to DMSO (2 mL) in a 20:6:1 mass ratio for a total solids mass of 27 mg. For the pH dependence experiments, a ratio of LMO: Super P carbon: PVDF = 25:6:4 for a total solids mass of 35 mg in 2 mL DMSO was used, as this ratio is found to provide a better chance of yielding a smooth film on the substrate while not sacrificing the electrochemical behaviour of LMO DMSO is much safer than N-methyl-2-

pyrrolidone and has been recently shown to be a promising green alternative with comparable slurry properties.[113] To disperse the solids, the mixture was magnetically stirred for 24 h, sonicated for 30 min, and shaken vigorously. A cut-out piece of titanium foil was polished successively with 1.0, 0.3 and 0.05 μm homogenised alumina suspension (Buehler) and thoroughly rinsed with Milli-Q water, before drying by N_2 blasting. To achieve a loading of 100 μg cm^{-2}, for a geometric electrode area of 0.636 cm^2, 6 μL of the suspension was deposited onto the titanium foil using an air displacement pipette. For the pH dependence experiments, 3 μL of the suspension was used due to a smaller exposed electrode area (0.16 cm^{-2}). The titanium current collector was chosen due to its low activity towards the oxygen evolution reaction (OER) which may take place on stainless steel at high states of charge and cause electrochemical interference.[114] Unlike stainless-steel alloys, Ti also does not contain manganese which may interfere with ICP-OES analysis by introducing artefacts. In view of the high boiling point of DMSO, the deposited ink was heated by an infrared lamp to accelerate the evaporation of the solvent. Higher ink loadings were avoided as these frequently led to mechanical cracking and detachment of the dried ink from the current collector.

3-2.3 Online electrochemical flow cell-ICP-OES

Two lab-built flow cells were designed and used in this study, namely type 1 flow cell and type 2 flow cell. The type 1 flow cell is a two-compartment droplet flow cell, Figure 3-1 and Figure 3-2(1). Similar to the flow through scanning droplet cell described by Schuppert et al.[115] the droplet through which the electrolyte solution flows is exposed at the bottom so that a solid sample can be raised up and closes the electrochemical circuit upon wetting. An ethylene propylene diene monomer (EPDM) rubber O-ring was glued to the edge of the opening using two-component epoxy glue (RS-components), defining a 0.636 cm^2 working electrode area. A flow rate of 1.5 mL min^{-1} was used to transport dissolution products away from the working electrode, using the onboard ICP-OES peristaltic pump downstream of the cell. As with the atomic emission spectroelectrochemical cell described by Ogle et al.,[116] the stagnant electrolyte compartment contained a 15 cm^2 carbon cloth counter electrode (Panex PW06, Zoltech) and was separated from the flow compartment by a microporous polypropylene separator membrane (Celgard 3401). The reference electrode (RE) was a Leak-Free (LF-1) Ag/AgCl/3.4 M KCl electrode (Innovative Instruments) positioned upstream of the working electrode compartment; all potential values in this paper are with reference to this RE.

The type 2 flow cell, Figure 3-2(2), was designed to better protect the electrodes and electrolyte against the effect of air, which could introduce more side reactions. Besides, the droplet in the type 1 flow cell usually requires perfect matching of the inlet and outlet flows, while the type 2 flow cell is gas-tight, making the cell built more accessible while not changing the working principle of the system. The type 2 flow cell was used in the pH dependence experiments. It has a slightly different WE area as defined by the cell geometry, which is a 0.4×0.4 cm^2 square. The same RE was used and a Pt coil electrode (~6 mm diameter, ~10 mm height, and ~0.5 mm thick) was used as the CE.

The ICP-OES was an Agilent 5100 dual-view instrument fitted with a Seaspray nebuliser, double-pass cyclonic spray chamber and 2.8 mm wide bore torch for high total dissolved solids applications. Due to a manufacturer recommended upper limit of 20 g L^{-1} total dissolved solids, the concentration of Li_2SO_4 was limited to 0.2 M. Data was acquired through the ICP Expert software LiveView feature, and the timestamps of the ICP-OES and the BioLogic SP-200 potentiostat/galvanostat were synchronised by comparing 12 one-minute long dissolution pulse intervals of zinc anodisation steps while monitoring the zinc emission signal at 213.856 nm. Manganese was monitored at 257.610 nm emission wavelength. Standard solutions between zero (blank) and 1 ppm were prepared by diluting 5, 10, 20, 30, 40 and 50 μL of 1000 ppm manganese ICP standard (Sigma-Aldrich) to 50 mL using 0.2 M Li_2SO_4; taking into account the cell footprint and electrolyte flow rate, these standard solutions cover an instantaneous Mn dissolution range between zero and 39 ng s^{-1} cm^{-2}. A limit of detection (LOD) between 0.015 ng s^{-1} cm^{-2} and 0.016 ng s^{-1} cm^{-2} was estimated for Mn by multiplying the standard deviation of a blank solution across 10 measurements by 3.[89] Assuming a standard normal distribution, the probability of a false positive signal 0.015 ng s^{-1} cm^{-2} from the mean blank signal is $(1-0.9987) \times 100 = 0.13\%$. We subtract the mean blank signal from the spectroscopic data instead of adding it to the calculated detection limit.

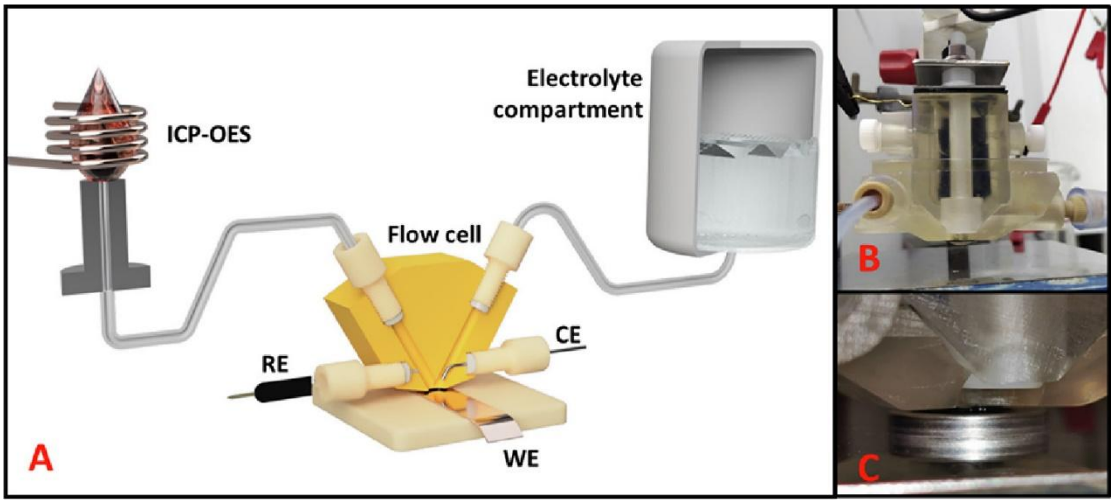

Figure 3-1. (A) Cross-section diagram of the online flow cell ICP-OES setup. (B) Photograph of the lab-built two-compartment droplet flow cell. (C) The flow cell in contact mode with a compressed exposure O-ring.

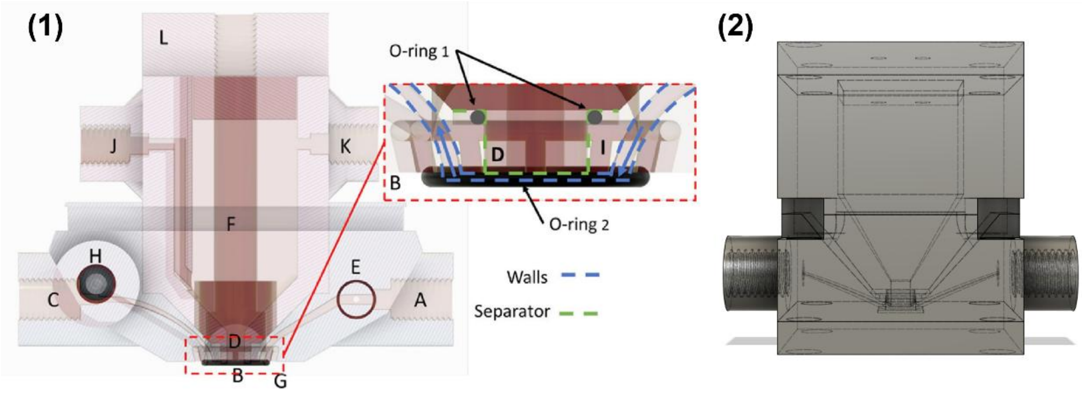

Figure 3-2. (1) cross-section scheme of the type 1 flow cell. (A) electrolyte inlet (B) flow compartment (C) electrolyte outlet (D) separator (E) reference electrode port (F) stagnant counter electrode compartment (G) working electrode sealing O-ring (H) nitrogen inlet port (I) nitrogen shield channels. (2) type 2 flow cell with an identical operation principle to type 1 but a slightly different exposed electrode geometry and area (0.16 cm^2).

The manganese standards yielded a linear relationship in the trace concentration range 0.1-1.0 ppm for the 257.610 nm wavelength. Spectroscopic intensity was converted to dissolution rate using Equation 3-1:

$$m_{Mn} = \frac{m_f \times f \times 10^6\, ng\, mg^{-1}}{A} \qquad \text{Equation 3-1}$$

where m_{Mn} is the dissolution rate in ng s^{-1} cm^{-2}, m_f the instantaneous dissolution concentration in mg kg^{-1}, f the flow rate in kg s^{-1} and A the electrode area in cm^2. The geometric area was that of the area defined by the flow cell O-ring, as the LMO particle size uncertainty (mesh-325) was large.

3-3 Results

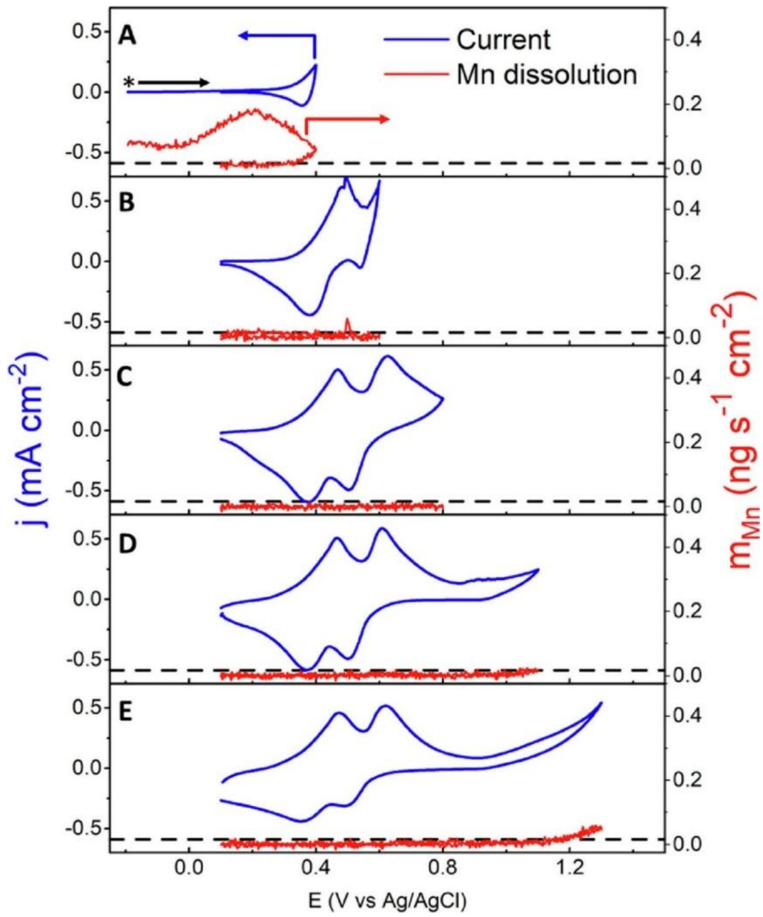

Figure 3-3. Cyclic voltammograms (blue traces, left axis) and simultaneous Mn dissolution rates (red traces, right axis) of drop-cast LMO in 0.2 M Li_2SO_4 with increasingly positive vertex potential (panels A-E). The starting potential is indicated with an asterisk. Scan rate 2 mV s^{-1}, flow rate 1.5 mL min^{-1}. The dashed line represents the 3σ detection limit of manganese.

Figure 3-3 shows cyclic voltammograms of a freshly prepared LMO electrode and the concurrent manganese dissolution rate, starting at the open circuit potential (OCP) after stabilisation for 30 min. Already during the first anodic scan, from OCP to 0.45 V, manganese dissolution is detected and increases to a maximum at 0.20 V, before falling below the detection limit, even as the potential scan direction is reversed.

During subsequent scans, with gradually increasing positive vertex potential (Figure 3-3, panels B-E), no further Mn dissolution is detected as long as the potential remains below +1.2 V. The anodic lithium extraction and cathodic insertion peaks agree well with published voltammograms in the same electrolyte.[117] In the range from 0.3 to 1.1 V, no dissolution features were observed above the detection limit that correlate to the order/disorder transition peaks of LMO, contrary to RRDE studies conducted in aprotic $LiPF_6$ electrolyte,[44] where Mn dissolution was found to increase rapidly at 90-100% state of charge (SoC). On our potential scale, this would correspond to 0.75-1.0 V, and no Mn is detected; only in the fifth scan (panel E), Mn dissolution is again detected for potentials above 1.2 V, well beyond 100% SoC and seemingly in the oxygen evolution region. In aprotic, $LiPF_6$/carbonate systems dissolution of manganese at 90-100% SoC may be promoted by carbonate oxidation and subsequent HF formation which may attack the LMO surface.[99]

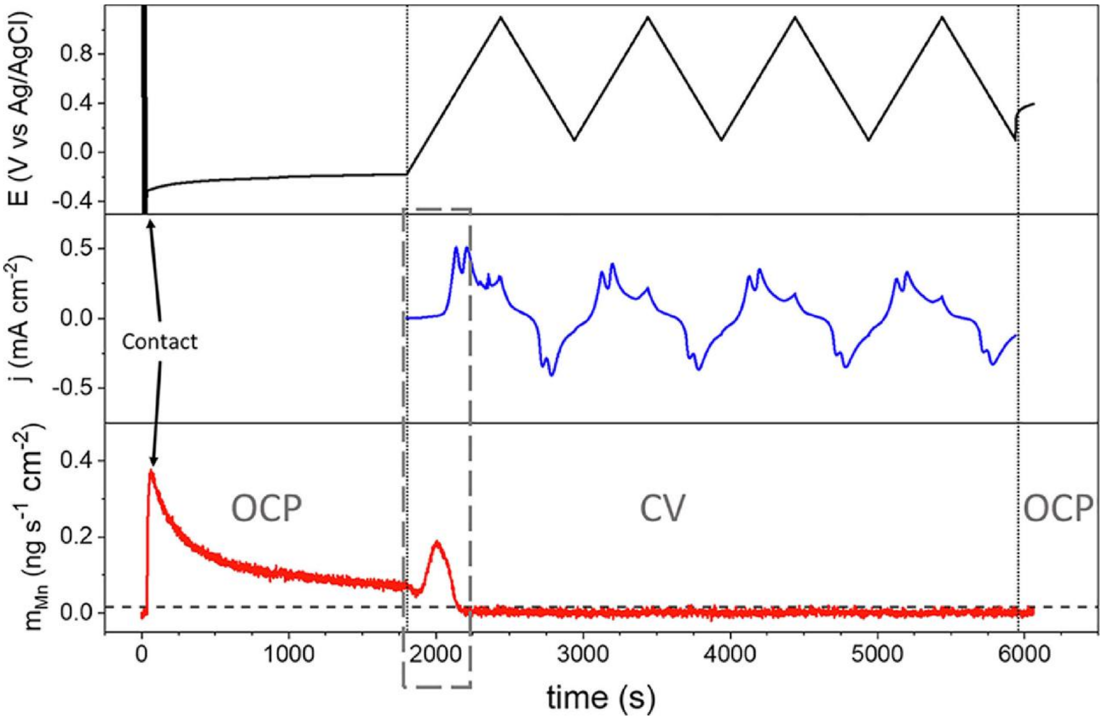

Figure 3-4. Potential (top), current (middle), and Mn dissolution rate (bottom panel) as a function of time after contacting a drop-cast LMO electrode with 0.2 M Li_2SO_4 at time zero. OCP and CV (4 cycles, scan rate 2 mV s^{-1}) regions as indicated. Flow rate, 1.5 mL min^{-1}. The dashed line represents the 3σ detection limit of Mn.

To investigate this behaviour in more detail, Figure 3-4 shows four consecutive cyclic voltammograms, preceded by a 30-minute OCP period following initial contact with the LMO electrode. Immediately after wetting of the LMO by the electrolyte, which itself may depend on the microscopic details of the electrode surface,[118] the manganese dissolution rate reaches 0.35 ng s^{-1} cm^{-2}, before decreasing exponentially to 0.1 ng s^{-1} cm^{-2} after 30 min. Over the same period, the electrode OCP value rises from -0.30 V to -0.20 V. Based on the Pourbaix diagram of manganese, this potential value suggests that Mn(II) is present.[119] The presence of sulfate anions increases the solubility of $Mn(OH)_2$ precipitates,[120] which may explain that any lower valence manganese oxide or hydroxide on the surface of the LMO particles is dissolved by the initial contact of Li_2SO_4 solution on electrode wetting.

During the first anodic scan, starting at 1800 s, the manganese dissolution rate passes through a maximum of 0.2 ng s^{-1} cm^{-2}, before falling below the detection limit for the rest of the experiment. After the four cycles, the OCP approaches 0.4 V, 0.6 V more positive than before cycling and indicating that the LMO electrode was not returned to its initial state. In the entire experiment, no Mn was detected in the electrolyte after the initial anodic scan, starting at t = 1800 s. The maximum in dissolution rate, at t = 2000 s, is accompanied by a slight shoulder in the current trace, in the potential region between 0 and 0.3 V. In sulfate electrolyte, oxidation features in this region have been linked to conversion of Mn_3O_4 to Mn_2O_3,[121] which would correspond to a change in the average Mn oxidation state from 2.67 to 3.

The dissolution-passivation feature at 2000 s appears to be of particular significance, as it separates regions of active Mn dissolution before the maximum from undetectable Mn levels in the electrolyte after. In order to analyse this feature (highlighted by a dashed box in Figure 3-4) in more detail, we show a magnification in Figure 3-5. By fitting an exponentially increasing baseline to the initial and final segments of the current trace, we can integrate the charge corresponding to the shoulder in the voltammogram, yielding 1.41 mC cm^{-2}.

For the sake of comparison, we also convert the Mn dissolution signal into an equivalent current using Equation 3-2, assuming a 1-electron Faraday process and considering that

$$j_{\mathrm{Mn}} = \frac{m_{\mathrm{Mn}} z F}{M_{\mathrm{Mn}}}$$ Equation 3-2

where M_{Mn} = 54.94 × 10^9 ng mol^{-1} is the relative atomic mass of manganese, F = 96,485 C mol^{-1} Faraday's constant and z = 1 the assumed charge transfer number for the dissolution process. The conversion thus assumes that each manganese ion detected by ICP-OES contributes one electron to the equivalent manganese dissolution current j_{Mn}, which is plotted in Figure 3-5. Integrating the peak in j_{Mn} yields 59.0 μC cm^{-2} (equivalent to Mn dissolution of 33 ng cm^{-2}), which is less than 5% of the electrochemical charge producing the shoulder in the voltammogram. Clearly, therefore, the current shoulder cannot be explained by a 1-electron anodic dissolution process, but may instead be related to electrochemical oxidation of the surface itself, mostly without forming soluble Mn products, Equation 3-3:[122]

$$j_{ext} = j_{diss} + j_{film} + \cdots$$ Equation 3-3

where the total externally measured current (j_{ext}) consists of direct anodic dissolution (j_{diss}) and other contributions (e.g. film formation, j_{film}).

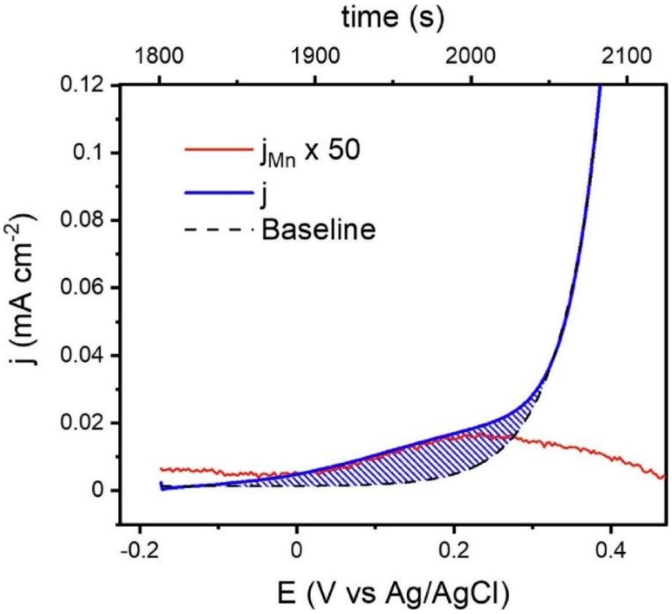

Figure 3-5. Magnified initial anodic scan (from Figure 3-4), revealing a shoulder in the current trace. The concurrent Mn dissolution signal has been converted to an equivalent current, assuming a 1-electron Faraday process.

So far, we have established that Mn dissolution occurs when a pristine LMO electrode is exposed to sulfate electrolyte under open circuit conditions, but that this dissolution ceases as soon as a single anodic scan over 0.5 V has occurred.

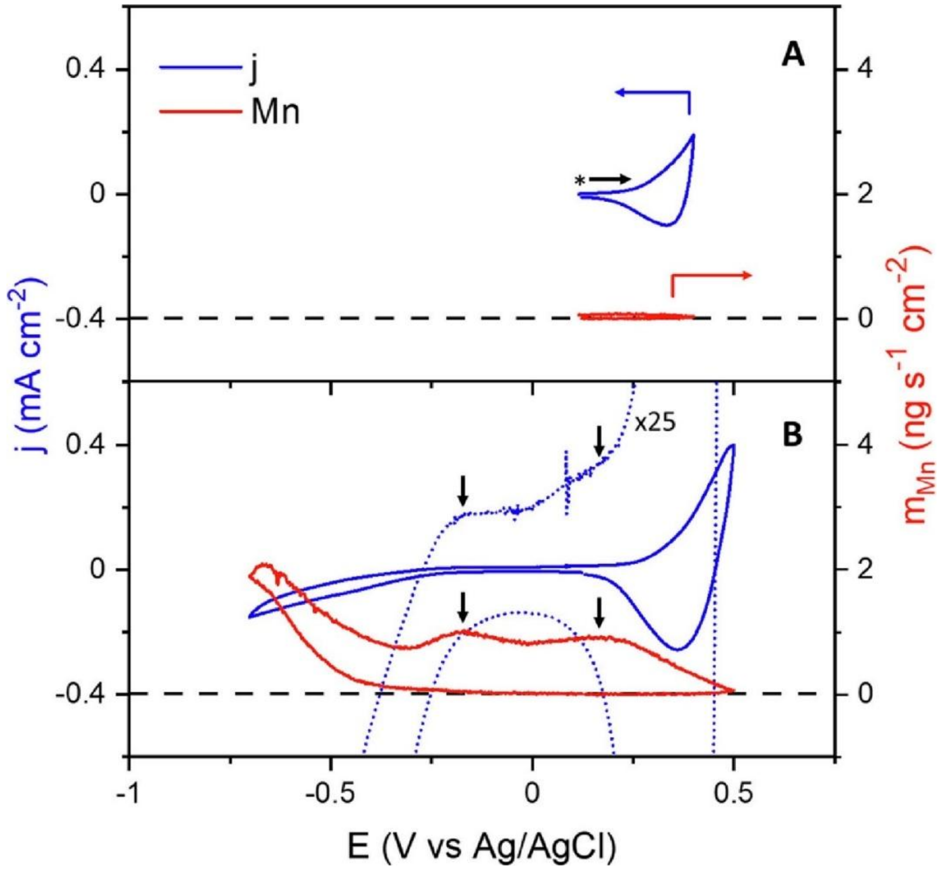

Figure 3-6. Cyclic voltammograms (blue traces, left axis) and instantaneous Mn dissolution rates (red traces, right axis) of drop-cast LMO in 0.2 M Li_2SO_4, exploring the negative potential region where overlithiation takes place (panel B), after brief anodic potential excursion to passivate the surface (panel A). The starting potential is indicated with an asterisk. Scan rate 2 mV s^{-1}, 1.5 mL min^{-1} flow rate.

To investigate the behaviour under conditions of overlithiation or, in battery science terminology, overdischarge, a fresh LMO electrode was first passivated by brief anodic polarisation, Figure 3-6A, before going to more negative potentials, Figure 3-6B. As the potential passes -0.1 V, a nonzero cathodic current is accompanied by reactivation of manganese dissolution, increasing exponentially before tailing off at -0.7 V. During the return scan, the instantaneous Mn dissolution remains significant, with peaks at -0.2 V and +0.2 V, and only falls below the detection limit when the potential is increased above 0.5 V, similar as in Figure 3-3 and Figure

3-4; this behaviour was consistent during subsequent cycles. We note that the Mn dissolution in the overlithiation region is an order of magnitude more intense than in the delithiation region discussed earlier. This is most striking in Figure 3-6A, where the dissolution-passivation feature is almost invisible on the vertical scale that is relevant for Figure 3-6B, and may be a further indication that the anodic behaviour is limited to the surface, while the cathodic behaviour involves the bulk of the electrode. The dissolution peaks correspond to 1.8 µA cm^{-2} at -0.18 V and 1.6 µA cm^{-2} at 0.15 V, almost an order of magnitude lower than electrochemical features at 7.4 µA cm^{-2} and 14 µA cm^{-2} respectively.

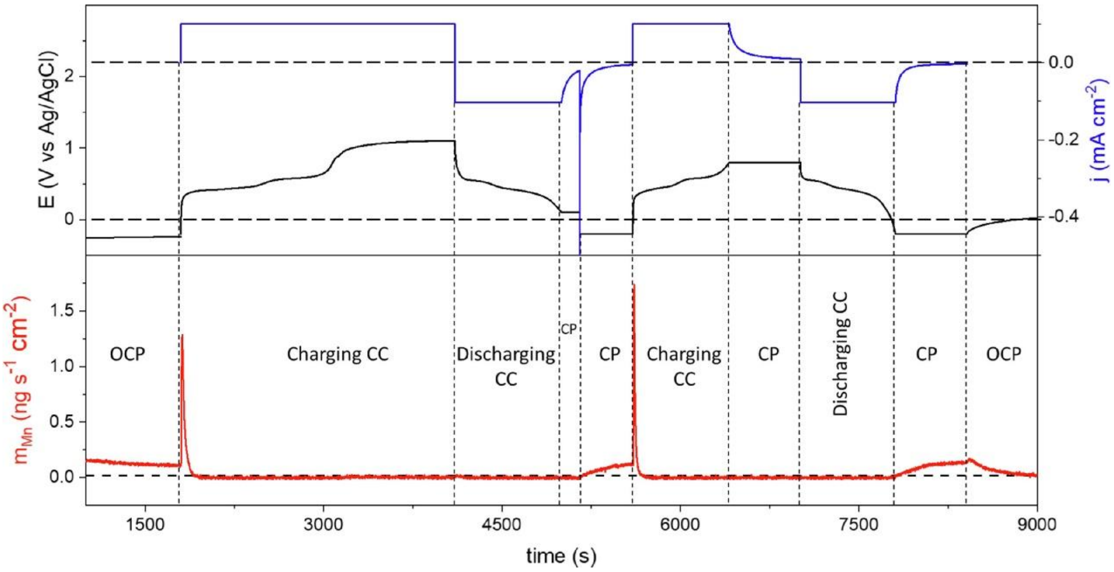

Figure 3-7. Galvanostatic charging-discharging of drop-cast LMO electrode (top) and instantaneous Mn dissolution rate (bottom) in 0.2 M Li_2SO_4. OCP, constant current (CC) and constant potential (CP) regions as indicated.

The Mn dissolution patterns discussed above were also confirmed using a galvanostatic charging-discharging protocol, Figure 3-7. Measuring in the same potential range by galvanostatic programming reveals the same dissolution pattern as observed in cyclic voltammetry, including manganese dissolution after initial delithiation. When the LMO electrode is switched from OCP to galvanostatic charging after 1600 s, a sharp dissolution peak accompanies the electrode potential rising from -0.1 V to 0.4 V, before decaying below the detection limit. Integration of the peak yields a total mass loss of manganese during this event of 21.6 ng cm^{-2}.

After the two phase transition potential plateaus from delithiation,[123] a third plateau at 1.1 V appears at 3000 s, which may correspond to oxygen evolution on the LMO electrode,[124] however without detectable Mn dissolution. At this point, galvanostatic discharging was started using the same but opposite current density, until a potential of 0.1 V was reached at 4900 s; this end-of-discharge potential was held for 300 s to allow the electrode to homogenise at the knee-point. To investigate under which conditions Mn dissolution rekindles, the potential was stepped down at 5200 s to -0.1 V, the OCP value just before initial charging. Immediately, the Mn dissolution resumes, and over time again approaches 0.1 ng s^{-1} cm^{-2} while the cathodic current density for lithium insertion approaches zero. The dissolution rate at 0% SoC is therefore consistent, and not dependent on whether the corresponding potential is assumed spontaneously (as true OCP) or is imposed.

A second charging cycle starts at 5600 s, again with an initial spike in manganese dissolution rate to above 1 ng s^{-1} cm^{-2}, shortly followed by passivation. The total manganese mass loss during the spike at 5600 s is 27.8 ng cm^{-2}, close to the mass loss determined from the first dissolution peak at 1600 s and from the cyclic voltammogram in Figure 3-2. A potentiostatic segment (6500-7000 s, at 100% charge) does not cause dissolution. Only a return to -0.1 V, at the end of discharge at 7800 s, restarts manganese dissolution. When potential control is released at 8100 s, the OCP increases towards 0 V while Mn dissolution tails off, suggesting that the LMO electrode was not fully lithiated before being relaxed, and therefore immune to dissolution.

To further investigate the pH dependence of Mn dissolution, two fresh LMO electrodes were prepared and their dissolution was compared in the acidified (pH = 3) and alkalized (pH = 9.5) electrolytes, Figure 3-8. In both electrolytes, the characteristic Li (de)intercalation peaks of LMO remained observable.

At pH = 3, the Mn dissolution was kept significant and fluctuated between 10-30 ng s^{-1} cm^{-2} during the whole 30 min OCP, Figure 3-8(A), suggesting that the chemical dissolution is promoted by the low pH value. It only dropped down below the detection limit after LMO reached its first oxidation peak, Figure 3-8(C) No Mn dissolution above the detection limit was found during the rest of the Li extraction even when the potential was scanned to 1.4 V. The dissolution was reactivated after the potential was scanned back below 0.97 V and grew immediately to ~12 ng s^{-1} cm^{-2}, followed by fluctuations between 6-14 ng s^{-1} cm^{-2} until the first oxidation peak of LMO in the flowing cycle. The Mn dissolution in the second cycle showed an identical trend but slightly lower values.

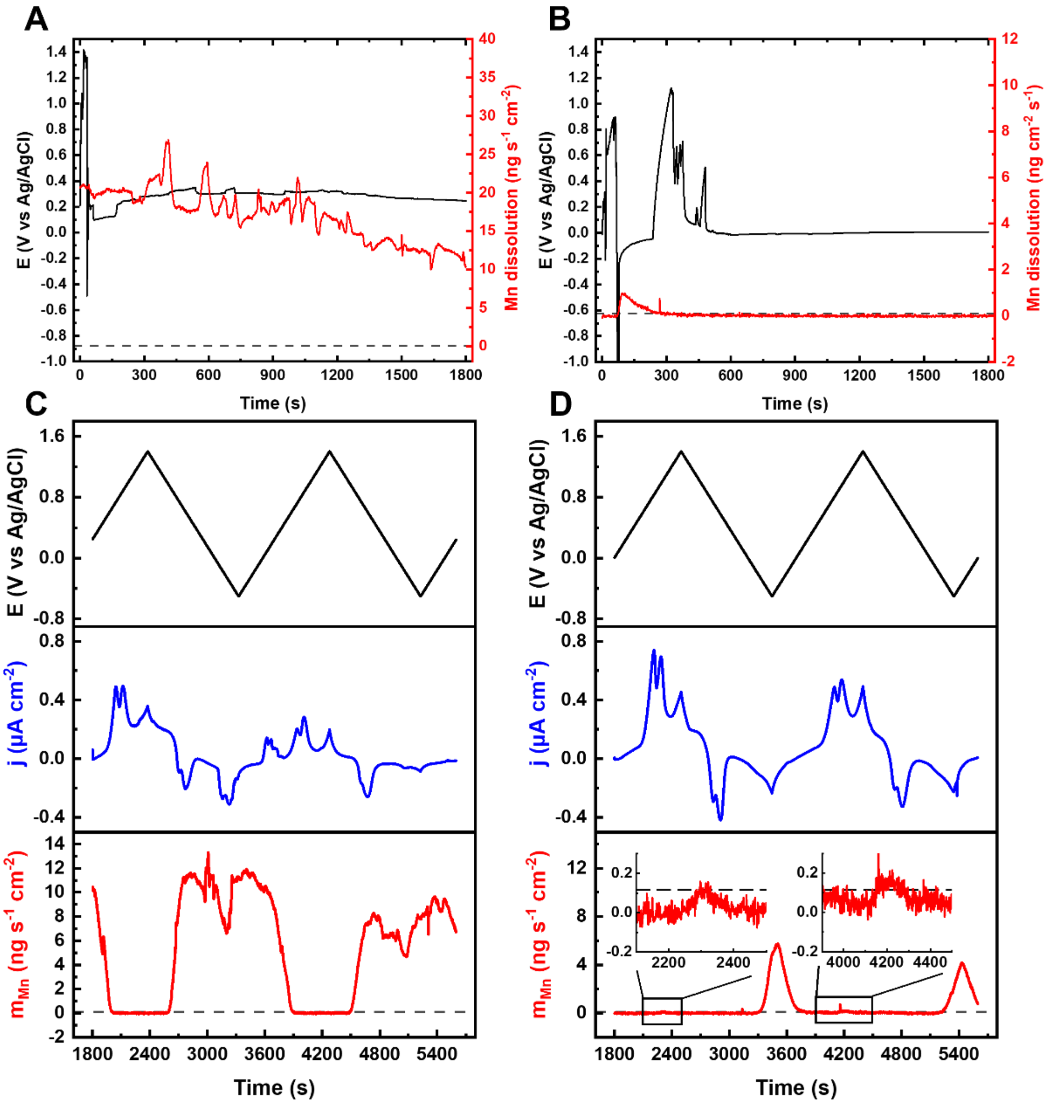

Figure 3-8. Mn dissolution rate of drop-cast LMO in (A) 0.2 M Li_2SO_4 pH = 3 (adjusted by concentrated H_2SO_4) and (B) 0.2 M Li_2SO_4 pH = 9.5 (adjusted by concentrated NaOH) during a 30 min-OCP period. The dissolution during CV: potential (top), current density (middle), and Mn dissolution rate (bottom) as a function of time in (C) 0.2 M Li_2SO_4 pH = 3 and (D) 0.2 M Li_2SO_4 pH = 9.5. The insets in (D) are the zoom-in of the highlighted area. Scan rate: 2 mV s^{-1}, flow rate: 1.5 mL min^{-1}.

At pH = 9.5, though a dissolution peak up to 1 ng s^{-1} cm^{-2} was observed upon wetting, it decreased below the detection limit after 280 s, Figure 3-8(B) No detectable Mn dissolution was found during the charging and overcharging except for a tiny growth that was found when LMO was scanned to its second Li extraction peak, as shown in the insets of Figure 3-8(D) bottom panel. In the overdischarging region, noticeable Mn dissolution was detected as long as the potential was scanned below -0.22 V, and the dissolution peak values in both cycles were found slight after the negative vertex potential.

3-4 Discussion

Central in the understanding of Mn dissolution from its oxides is its oxidation state, and our data in delithiated and overlithiated regimes show this effect immediately. In LMO ($LiMn^{III}Mn^{IV}O_4$) at full lithiation, the average Mn oxidation state is 3.5, and Mn dissolution from this material is typically explained by invoking Hunter's mechanism of acid-mediated disproportiation, Equation 3-4:[35]

$$2LiMn_2O_4 + 4H^+ \rightarrow 3\lambda\text{-}MnO_2 + Mn^{2+} + 2Li^+ + 2H_2O \qquad \text{Equation 3-4}$$

where Mn(III) forms highly soluble Mn(II) and insoluble Mn(IV) species. As the electrode potential increases and delithiation starts, the equation predicts a decreasing rate of dissolution, proportional with the increasingly sparse Mn(III) sites at the surface.

Our data, however, both potentiostatic and galvanostatic measurements in the pure 0.2 M Li_2SO_4, show a marked increase in dissolution rate upon initial charging, immediately followed by Mn dissolution becoming undetectable, very much like a classic anodic dissolution-passivation transition during metal passivation. This observation alone indicates that Hunter's mechanism in isolation cannot explain the observed behaviour.

Furthermore, Hunter's mechanism is acid-driven, and DFT calculations have shown that this pathway becomes energetically unfavourable above pH 4-5, such as in the pure 0.2 M Li_2SO_4 and pH = 9.5 0.2 M Li_2SO_4 electrolytes used in this study.[125] The dramatic increase in Mn dissolution during initial delithiation of LMO, followed by an even more abrupt end to the dissolution as the potential is made more positive, may indicate a dissolution-precipitation mechanism, or a compositional or phase change of the electrode surface layer, the nature of which is as yet unclear. A detailed understanding of these surface changes will require in-depth surface analyses.

Our data in the electrolytes with different pH showed two main dissolution areas, that are, when LMO approached the end of charging and when LMO is overdischarged. When the LMO approaches the end of charging, dissolution was only detected in neutral and pH = 9.5 electrolyte, suggesting the following process happened, Equation 3-5:

$$\mathrm{Li_aMn_2O_4} \rightarrow \mathrm{aLi^+} + \mathrm{MnO_2} + \mathrm{Mn^{x+}} + (\mathrm{x}+\mathrm{a})\mathrm{e^-} \quad (\mathrm{a} < 1) \qquad \text{Equation 3-5}$$

The dissolution during the end of discharge and overdischarge region was found to be strongly promoted when using pH = 3 electrolyte compared with the other two electrolytes, suggesting the process is likely to be dependent on pH, Equation 3-6:

$$\mathrm{3LiMn_2O_4} + \mathrm{Li^+} + (9-2\mathrm{x})\mathrm{e^-} + \mathrm{8H^+} \rightarrow \mathrm{2Li_2Mn_2O_4} + \mathrm{2Mn^{x+}} + \mathrm{4H_2O} \qquad \text{Equation 3-6}$$

In studies on $LiPF_6$-containing LMO batteries, post-mortem elemental analysis of the lithium anode suggested that the greatest Mn dissolution took place for batteries stored below 30% SoC and above 90% SoC, with a middle region (30% to 80% SoC) where manganese dissolution was low but not zero, and that smaller LMO particle sizes yielded more dissolution.[126] Some of the discrepancy between manganese dissolution in aqueous and non-aqueous electrolytes may be explained by Mn(II) and Mn(III) stability in aqueous Li_2SO_4, especially at medium to low pH, and non-aqueous $LiPF_6$ electrolyte, as Mn(III)-containing dissolution products have been identified in non-aqueous electrolyte by EPR,[48] and Mn(III) dissociation pathways in presence of F^- may be possible.[49]

In the present study, we did not observe Mn dissolution within the (de)intercalation window itself, or even 0.4 V beyond the second phase transition peak of lithium deintercalation, as opposed to Wang et al. and Zhao et al.[42,44] However, in most dissolution experiments,[42,44–46] or indeed in standard lithium-ion coin cells, stainless steel is used as a current collector, where manganese can constitute up to 10% of the mass depending on the alloy. Some manganese detected in the electrolyte may therefore be a current-collector-induced artefact and not originate from the active electrode material.

Mn dissolution was again detected at very positive potentials, past full deintercalation of Li^+ from the λ-MnO_2 host structure. In $LiPF_6$-carbonate electrolytes, the delithiated λ-MnO_2 surface is found to be unstable and breaks down to Mn_3O_4 ($Mn^{II}Mn^{III}{}_2O_4$) which contains a higher proportion of Mn(III) and also free Mn(II), both of which could lead to more dissolution.[34,127] This degradation, however, was found at a less positive potential (4.3 V vs Li^+/Li) compared to our findings and may not explain our observation. Another phase transition to O3-layered MnO_x structure or O^{2-} redox at 5.1 V vs Li^+/Li which corresponds to significant overcharging has also been identified.[128] This potential range corresponds better to the dissolution rates observed in Figure 3-3, about 1 V positive of the first phase transition peak in the voltammograms, suggesting that we reached the onset of this phase transition at 1.2 V vs Ag/AgCl, with concurrent oxygen evolution from the electrode. In both cases, these surface species disappear after discharge, possibly due to dissolution. Although Mn dissolution from the degradation process at 4.3 V vs Li^+/Li was not observed here, this could be due to an insufficient detection limit of the ICP-OES setup. Moving forward, it may be possible to isolate and study in more detail individual Mn dissolution processes by tuning electrolyte and solvent.

Overlithiation (at potentials negative from the initial OCP) produces very different while active Mn dissolution behaviour, in line with RRDE collection experiments[44] and increased capacity fade and dissolution due to the lower average Mn oxidation state in $Li_2Mn^{III}{}_2O_4$,[129] promoting Mn(III) disproportiation. For these overlithiated structures, DFT calculations found Hunter's mechanism to remain energetically favourable up to pH 8,[125] which may explain the increased dissolution rate upon cathodic polarisation we observe. In non-aqueous electrolytes, spiking the electrolyte with Mn^{2+} causes a decrease in reductive peak intensity, another argument in support of this interpretation.[130] Tetragonal $Li_2Mn_2O_4$ therefore appears consistently more unstable compared to $LiMn_2O_4$.

While our measurements confirm the instability of fully lithiated and especially overlithiated LMO electrodes, the large discrepancies between reported Mn dissolution in aprotic electrolytes and the current work also show that electrolyte nature and composition have a major impact on battery electrode stability. Furthermore, careful design of charging/discharging profiles to avoid the electrode from entering potential regions characterized by intense Mn dissolution, may be a viable alternative to the use of surface coatings or artificial CEIs in optimising battery life.[106]

Our data reveal very detailed dissolution information, and also suggest whether dissolution events or regions are related to a surface state or process, such as superficial oxidation, or to bulk properties of the electrode under study, such as structural strain from Li^+ intercalation, which constitutes most of the measured current. In the battery field, the vast majority of efforts are aimed at increasing performance through careful optimisation of bulk synthesis, with extensive characterization of crystallography, etc. Every electrode material, however, interacts with its environment through its surface, so that the details and properties of the latter are of overwhelming importance, including those of the double layer after the electrode-electrolyte interface has been established, and possible additional phases have formed (SEI, CEI). For fundamental energy-minimising reasons, the structure of a solid surface necessarily differs from that of the bulk, sometimes leading to striking surface reconstructions, affecting its reactivity, even in the absence of dangling bonds. For this reason, the importance of experimental and theoretical surface science investigations of battery electrode materials can hardly be overestimated.

3-5 Conclusion

By coupling a flow-through electrochemical cell to an ICP-OES, we have obtained detailed Mn dissolution data from a drop-cast $LiMn_2O_4$ (LMO) electrode in aqueous 0.2 M Li_2SO_4, as a function of both time and potential/state of charge. Fully lithiated LMO, with an average Mn redox state of 3.5, readily dissolves when contacted by 0.2 M Li_2SO_4, but initial charging that precedes delithiation abruptly stops further detectable dissolution, until well past fully delithiated λ-MnO_2. In marked contrast with aprotic electrolytes, we found no correlation between dissolution and the lithium insertion-extraction process. Dissolution resumes on returning to the initial potential of pristine LMO, and increases exponentially in the overlithiation region. Besides, dissolution was clearly detected not only in the acidic condition, but also in neutral and alkaline electrolytes, though increasing the pH decreased the overall amount of Mn dissolved Our results provide access to much more detailed dissolution information than post-mortem battery analysis allows, enabling targeted materials screening and informing best practices in charging/discharging profiles. In particular, our data suggests that suitable potential conditioning of electrodes may mitigate dissolution, as an alternative or additional measure to the use of protective surface films or incorporation of dopants.

As an outlook, the very detailed, real-time dissolution information to which our method gives access allows us to investigate in a straightforward manner the effect of many variables: electrode material particle size, presence of dopants, film thickness (differentiating between “thin film” or “thick film” regimes, depending on whether the entire film participates in the behaviour or only superficially[131]). Demonstrated here for a drop-cast electrode, the *in-situ* flow-through droplet cell allows investigation of commercial electrodes and materials with minimal modifications, but also single crystals and thin films produced using pulsed laser deposition methods,[132] which make in-depth surface characterization easier.

Chapter 4. Revisiting the role of Mn^{3+} disproportionation for Mn dissolution from spinel $LiMn_2O_4$ as a Li-ion battery cathode

As stated in previous chapters, Mn dissolution is one of the biggest factors that limit the wider application of Mn-containing Li-ion cathodes. With an increasing number of degradation phenomena that the widely accepted Mn^{3+} disproportionation mechanism cannot explain, we here investigated more the Mn dissolution mechanism of $LiMn_2O_4$ (LMO). Online ICP-OES is a powerful technique for real-time dissolution detection with extraordinary detection limit but cannot give information regarding the dissolving species. Thus, RRDE was employed together with online ICP-OES for quantitative real-time electrolyte analysis of Mn dissolution detection and speciation, which is essential for understanding the dissolution mechanism. Our results suggest that Mn^{3+} is the dissolving species when LMO approaches the end of charging, while Mn^{2+} dissolves when LMO is overdischarged in the first cycle. In the following scans, another dissolution period that contains both Mn^{2+} and Mn^{3+} is found during the Li^+ extraction from LMO. Our results refine the use of Hunter's mechanism in explaining Mn dissolution from Li-ion cathodes and demonstrate the capability of RRDE for quantitative real-time study of transition metals dissolution in Li-ion batteries and beyond.

4-1 Introduction

The dissolution of Mn^{2+} during chemical delithiation of LMO in an acidic aqueous solution was first proposed by Hunter,[35] Equation 4-1, and effectively involves disproportionation of Mn(III) into +II and +IV forms:

$$2\mathrm{LiMn_2O_4} + 4\mathrm{H^+} \rightarrow 3\lambda\text{-}\mathrm{MnO_2} + \mathrm{Mn^{2+}} + 2\mathrm{Li^+} + 2\mathrm{H_2O} \qquad \text{Equation 4-1}$$

This mechanism was then introduced into battery research and used for explaining the Mn dissolution behaviour in various Mn-containing cathodes,[36,39] but encountered an increasing number of questions in recent years.

Hanf et al. observed Mn^{3+} as the main dissolving species from $LiNi_{0.5}Mn_{1.5}O_4$ (LNMO) in aqueous buffer solutions with the presence of a TM-ion-scavenging agent, and solely Mn^{2+} in the organic carbonates-based electrolyte by soaking the sample powder and then using capillary electrophoresis with ultraviolet-visible (UV-vis) detection. Their results showed that Mn dissolution was accelerated at elevated temperature. Although this method can quantify both Mn^{2+} and Mn^{3+} in a single run, it is hard to use for other TMs like Co or Ni due to their instability with the complexing agent. Besides, such *ex-situ* detection cannot reveal the dependence of dissolution on potential, state of charge, etc.[133]

Zhao et al. used 4-(2-pyridylazo) resorcinol (PAR) as a UV-vis probe for *in-situ* monitoring of Mn^{2+} dissolution in the typical Li-ion carbonate electrolyte during cyclic voltammetry. They observed changing Mn^{2+} signal during cycling. The excellent selectivity of the PAR probe enabled them to observe Mn^{2+} dissolution but its capability with other Mn species and other TM elements remains undiscovered.[134]

Wang et al. modified a Swagelok cell and detected LMO dissolution responses, in a 1 M $LiPF_6$ EC/DMC 1/1 (v/v) electrolyte, from non-Mn^{2+} species, which they believed was caused by Mn^{3+}. Their results showed a peak dissolution signal feature around 3.8 V (started upon charging) during the first charging, which then decreased to the background value together with the characteristic LMO oxidation peaks appearing. In the following discharging, they saw weak dissolution signals again when LMO was discharged to 3.9 V below. In the second and third cycles, they only detected background level signals, which they attributed to the surface state changes of LMO during the first cycle.[43] However, as they attribute the oxidation current on their Pt sensing electrode to Mn^{3+} oxidation, their sensing electrode was very likely poisoned in the following cycles, as MnO_2 was very likely the product or one of the products.

Wang et al. used RRDE collection in the study of Mn^{2+} dissolution from LMO and LNMO, where they saw dissolution throughout the entire (dis)charging of the materials though with varying intensity. Their setup is similar to our study in this chapter, but their applied ring potential was so negative that not only Mn^{2+} but also other Mn species could be reduced (and thus detected).[45,46,135]

The Halalay group combined electron paramagnetic resonance (EPR), ICP-AAS, and X-ray absorption near-edge spectroscopy (XANES) *ex-situ* analysis and claimed that Mn^{3+} is the main dissolving species from LMO and Mn^{2+} from LNMO.[136,137] However, their assumption that all Mn^{2+} is EPR-visible and Mn^{3+} is EPR-silent is under debate.[138]

Allen et al. analyzed *ex-situ* TMs dissolution from LMO, LNMO, and $LiNiO_2$ (LNO) by solution nuclear magnetic resonance (NMR) and ICP-optical emission spectroscopy (ICP-OES). Their results show that all TMs dissolve as +2 oxidation states.[50]

Rynearson et al. performed *ex-situ* qualitative TMs dissolution analysis and speciation from LMO, LNMO, NMC811, and LMRNMC by X-ray absorption spectroscopy (XAS) and XANES. Their results showed that the average Mn oxidation state from the electrolyte of a cycled (for 100 cycles) LMO||graphite cell is 2.62 ± 0.04, and they suggested that Mn^{3+} is the main dissolving species directly from LMO, and the Mn^{2+} was generated by the subsequent disproportionation or reduction of Mn^{3+} in the electrolyte in a longer time scale.[51]

In this chapter, we first studied the redox properties and kinetics of Mn^{2+} and Mn^{3+}, which are the two main dissolving species, by using RRDE, Koutecky-Levich (KL) analysis, Cottrell analysis, electrochemical impedance spectroscopy (EIS) and Raman spectroscopy. Then, we combined RRDE and online ICP-OES for real-time detection and speciation of Mn dissolution from LMO. Aqueous 0.2 M Li_2SO_4 electrolyte was used for the capability of the ICP-OES torch, where LMO can maintain similar cyclability to that in carbonates electrolytes and is not affected by cathode-electrolyte interphase (CEI) formation.[103] Our results suggest different dissolution mechanisms during charging and discharging, that is, surface Mn^{3+} dissolves during delithiation and the dissolution of Mn^{2+} upon lithiation probably involves the bulk of LMO. Our results prove the ability of RRDE for real-time quantitative analysis of TMs dissolution in battery studies.

4-2 Experimental details

4-2.1 Chemicals preparation

All the aqueous solutions prepared were using ultrapure water (MilliQ, Millipore, 18.2 MOhm cm, total organic carbon < 2 ppb).

The 0.2 M Li_2SO_4 solution was prepared by dissolving lithium sulfate monohydrate (ACS reagent, ≥99.0%, Sigma-Aldrich) into ultrapure water. Ultrapure 96% H_2SO_4 from Supelco was used to adjust the pH of the 0.2 M Li_2SO_4 solution.

For the Mn dissolution detection, $LiMn_2O_4$ (LMO) powder, Super-P carbon, and PVDF were added to DMSO (2 mL) in a 25:6:4 mass ratio for a total solids mass of 35 mg. The mixture was sonicated for 30 min and shaken in a vortex mixer (Vortex Genie 2, Scientific Industries) for 5 min for better dispersion, followed by drop-casting 6 μL of the mixture onto the GC disc electrode of the RRDE, which was then dried under low vacuum overnight.

4-2.2 Electrochemical measurements

A RRDE from Pine Research Instrumentation was used in this chapter and it has a glassy carbon (GC) disc electrode with an outer diameter of 5.0 mm, and a Pt ring electrode with an inner diameter of 6.5 mm and an outer diameter of 7.5 mm. The theoretical collection efficiency N of RRDE with this geometry is 25%. The redox reaction of hexacyanoferrate (II)/(III) redox couple was used to validate the $N_{apparent}$ of the RRDE used in this chapter, which is 28.3±0.4%.

Before each measurement, the RRDE was polished by 1.0 and 0.05 μm homogenized alumina suspension (Buehler), followed by a thorough rinse with ultrapure water and drying by N_2. To ensure the surface state is identical for each measurement, a wide potential range, which covers the potential range of interests, cyclic voltammogram (CV) was applied in the blank supporting electrolyte solution for both the GC disc and Pt ring once polished.

The RE used for the measurements in this chapter was a Leak-Free Ag/AgCl/3.4 M KCl electrode (Innovative Instruments) and the CE was a Pt coil. The electrolyte was purged by Ar to remove the effect of air for at least 5 min before each measurement. All the glassware was cleaned using boiling nitric acid 20% (diluted from >65% reagent grade, Sigma-Aldrich), followed by copious rinsing. A BioLogic BP-300 potentiostat was used for the electrochemical measurements.

4-2.3 Raman spectroscopy

The Raman spectrometer used in this thesis is a Renishaw inVia confocal Raman microscope that features 532 nm and 785 nm lasers, with 15 mW and 20 mW maximum power, respectively. The spectra were recorded by WiRE software and processed by SpectraGryph (version 1.2) software.

4-2.4 Online ICP-OES measurements

The ICP-OES was an Agilent 5100 dual-view instrument fitted with a Seaspray nebuliser and double-pass cyclonic spray chamber. The type 2 flow cell, discussed in chapter 2 and 3, was used for all the measurements in this chapter.

4-3 Results & Discussion

4-3.1 Electrochemistry of possible dissolved Mn species

For the Mn dissolution from the LMO cathode, the main debates are focused on whether Mn^{2+}

or Mn^{3+} is the main dissolving species. Thus, it is essential to study the redox properties of both to explore whether reactions at the Pt ring can be used for speciation.

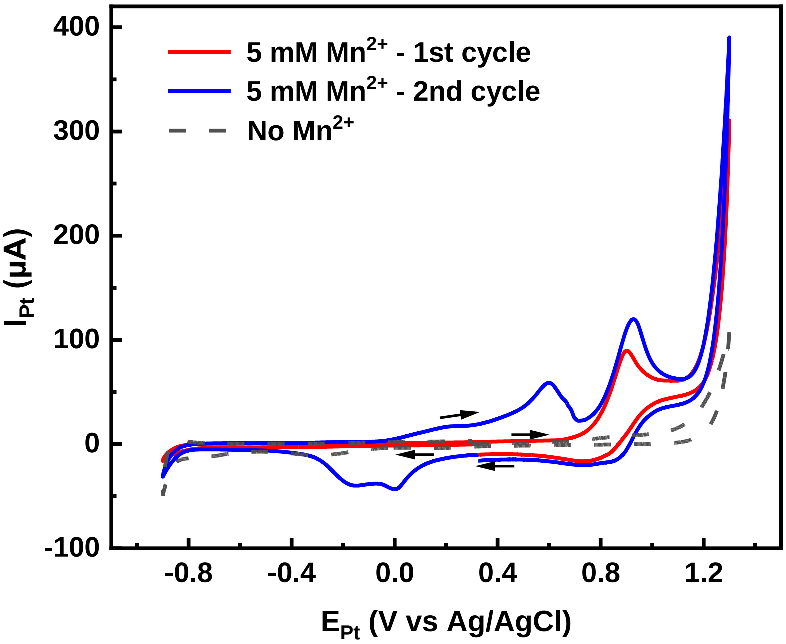

Figure 4-1. CV of 5 mM Mn^{2+} at the Pt ring electrode in 0.2 M Li_2SO_4, 10 mV s^{-1}, without rotation. The red trace is the first cycle and the blue trace is the second cycle. The voltammogram starts at OCP (~0.4 V) in the negative direction.

Figure 4-1 shows the cyclic voltammogram of Mn^{2+} on the stationary Pt ring electrode. No significant reduction current was found during the first cathodic scan as Mn^{2+} requires far more negative potential (i.e. at least -1.655 V vs Ag/AgCl) to be reduced to metallic Mn.[139] At -0.9 V, we see the onset of hydrogen evolution. In the following anodic scan, only one oxidation peak is observed at 0.9 V, before oxygen evolution is observed at 1.3 V. The electrode visibly turned brown after the first oxidation peak, suggesting the formation of MnO_2.[140–144] Three cathodic waves are observed during the second cathodic scan, at ca. 0.78 V, 0 V, -0.15V, which we ascribe to the reduction of Mn(IV) formed during the anodic scan.[145] This voltammogram indicates that aqueous Mn^{2+} has no redox activity within the potential range from -0.7 V to 0.6 V vs Ag/AgCl on bare Pt , providing suitable potentials for the detection of other soluble Mn species at the ring.

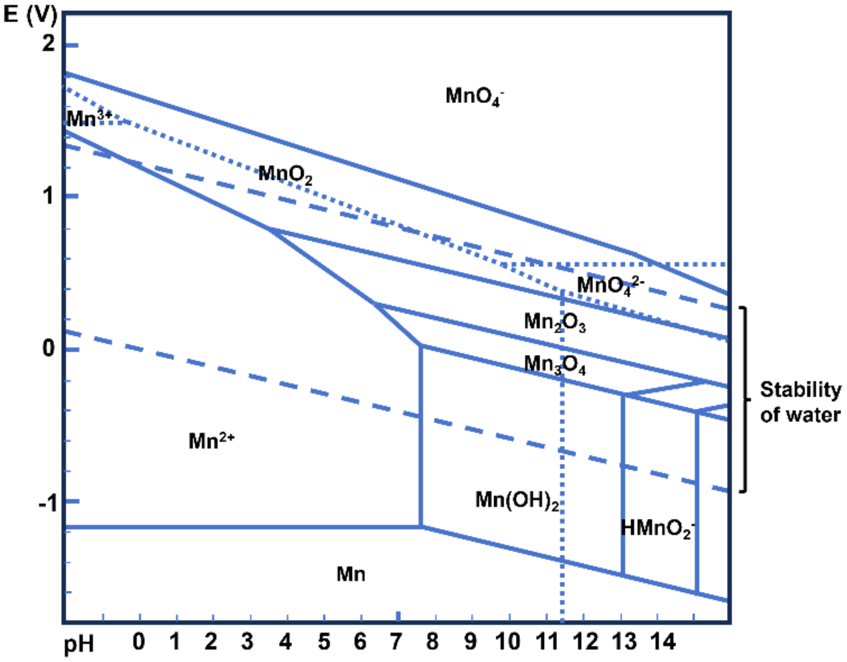

Figure 4-2. Pourbaix diagram of Mn. Potential-pH thermodynamic equilibrium of Mn-water system at 25°C, with soluble Mn species of concentration 10^{-3} M.[146]

The Pourbaix diagram for manganese, Figure 4-2, shows that possible soluble Mn species can exist in neutral to acidic solutions includes MnO_4^-, Mn^{3+}, and Mn^{2+}.[146] However, when the LMO is positively scanned, the MnO_2 is expected to form as Li is extracted from the structure, and the formation of MnO_4^- from MnO_2 requires at least 0.2 V more positive potential than oxygen evolution reaction in pH≤7 aqueous electrolyte, which is beyond the potential range of interest in this study, thus the formation of permanganate can therefore be excluded.

Mn^{3+} is another candidate as a dissolving species from Mn-containing LIB cathodes. It is thermodynamically unstable and can chemically disproportionate in aqueous electrolytes very quickly in the absence of any stabilizing ligand, which brings great difficulty in preparing and studying its electrochemical performance.[147–150] Although lowering the pH of the electrolyte may slightly prolong the lifetime of Mn^{3+},[144] the redox path between Mn^{2+}, Mn^{3+}, and Mn^{4+} may be altered.[151] Adding proper ligands can effectively stabilize Mn^{3+},[152] but can again shift its redox potential. Besides, different charge-discharge mechanisms of the LMO as a LIB cathode may also be caused by changing the pH or adding ligands. Thus, locally generating Mn^{3+} through oxidising Mn^{2+} on the disc electrode of an RRDE and studying its properties on the ring electrode is preferred.

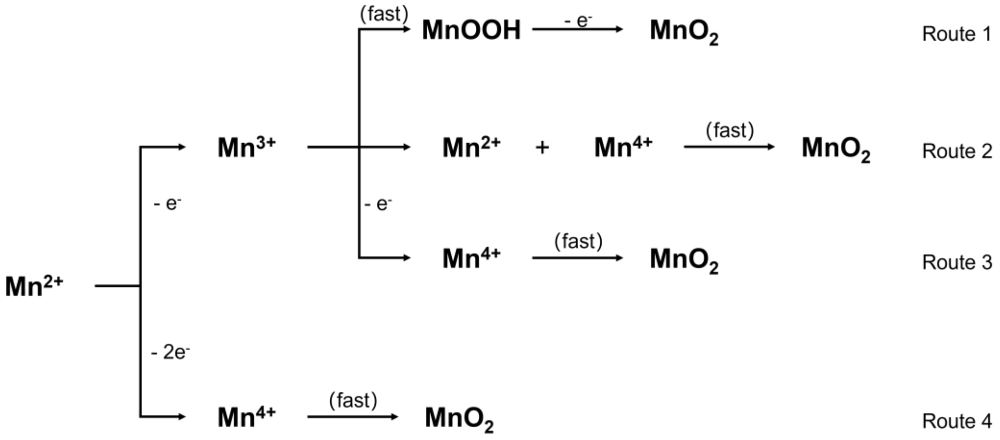

Figure 4-3. Summary of possible Mn^{2+} oxidation pathways from literatures.[140,142–144,151]

Possible Mn^{2+} oxidation pathways in neutral to acidic electrolytes suggested by literature are summarized in Figure 4-3.[140,142–144,151] Studies in both strongly acidic and alkaline electrolytes all identified dissolved Mn^{3+} on the ring electrode, implying that Mn^{3+} generated on the disc during the oxidation of Mn^{2+} is very likely to be detected on the ring in our neutral to acidified electrolytes.[143,153] We therefore conducted a series of RRDE experiments to generate the Mn^{3+} locally and investigate its redox activity.

As shown in Figure 4-4, in the pure 0.2 M Li_2SO_4 electrolyte, the Mn^{2+} oxidation current has an onset potential of 0.59 V and reaches the first plateau at 0.9 V. The plateau lasts until 1.1 V and then the current rises again and reaches the second plateau at 1.4 V. The corresponding ring current has the same onset potential as the disc but reaches the first peak value at 0.85 V. Then, it slightly drops until 1.2 V and increases again until 1.43 V. As Mn^{4+} can barely survive in the liquid electrolytes and Mn^{2+} does not have redox activity at the chosen ring potential, all the ring current detected is ascribed to reduction of Mn^{3+}. As two current plateaus are found, it is very unlikely that Route 4 in Figure 4-3 is followed for the first plateau.

With decreasing pH of the electrolyte, achieved by adding increasing amounts of sulfuric acid, the onset potentials of Mn^{2+} oxidation shift positively. The plateau currents maintain almost the same value until the pH of the electrolyte goes down to 2.04 (10 mM H_2SO_4) and gradually decreases when the pH gets below 2. Moreover, in low pH conditions (pH below 2), the current plateaus become peaks, which drop with the pH, suggesting the oxidation current is no longer limited by diffusion but kinetics.

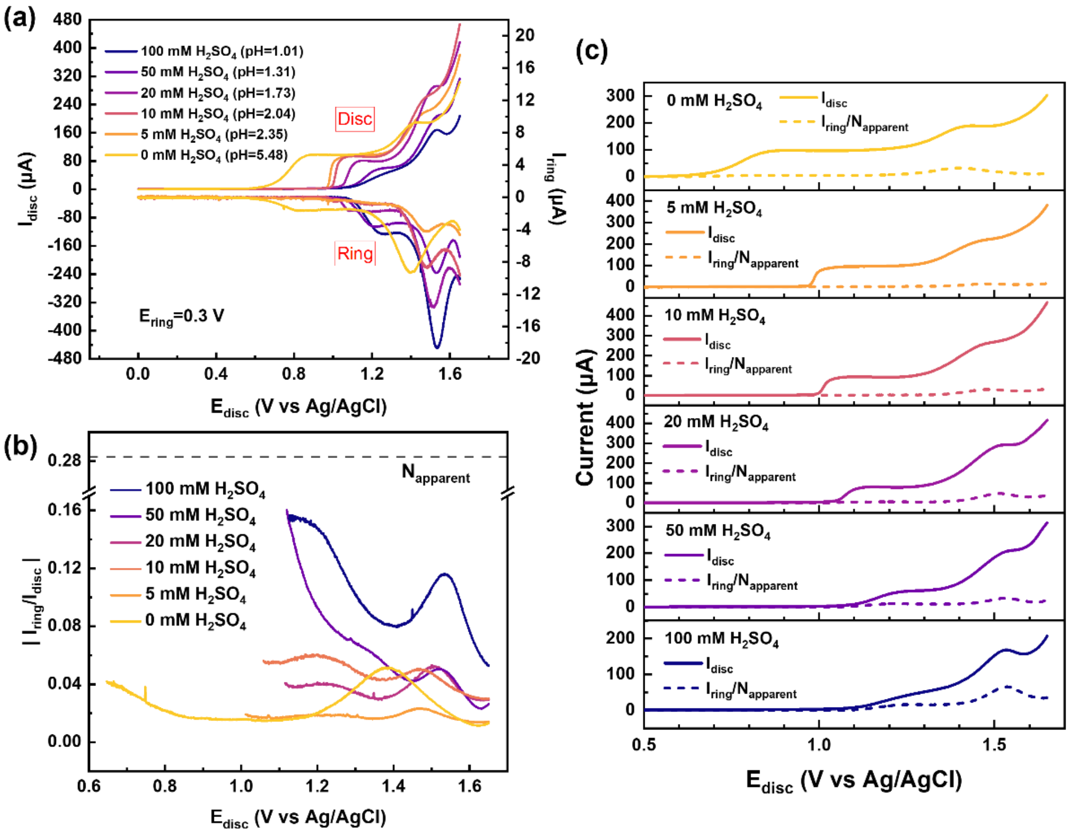

Figure 4-4. (a) Rotating Pt ring-GC disc voltammograms in 0.2 M Li_2SO_4 + 1 mM Mn^{2+} at different pH values. Rotation rate: 400 RPM. Potential scan rate: 10 mV s^{-1}. All positive currents are disc currents; all negative currents are ring currents. E_{ring} was held at 0.3 V vs Ag/AgCl. (b) The corresponding absolute value of I_{ring}/I_{disc} shown in (a), the dashed line represents the $N_{apparent}$ of this RRDE. (c) Comparison of I_{disc} and the absolute value of $I_{ring}/N_{apparent}$.

When the pH of the electrolyte is decreased, the ring currents during the first current plateau on the disc first decrease (from 0 mM H_2SO_4 to 10 mM H_2SO_4) and then become more pronounced (from 10 mM H_2SO_4 and more acidic conditions), meaning that either the survival time of Mn^{3+} first decreases then increases with decreasing pH value or the kinetics of the following reaction that consumes Mn^{3+} is changed by pH or these two combined. As shown in Figure 4-4(b) and (c), though the $|I_{ring}/I_{disc}|$ value in the electrolyte with 100 mM H_2SO_4 is higher than the one in 0.2 M Li_2SO_4, the data points in between them did not show a clear trend, indicating that both the lifetime of Mn^{3+} and the kinetics of the following reaction are altered by the pH value. Moreover, when disc potential was higher than 1.6 V, the $|I_{ring}/I_{disc}|$ value in all electrolytes decreased noticeably, suggesting that increasingly Mn became Mn^{4+} (and thus MnO_2), which built the film on the disc instead of reaching the disc. Besides, only in the two most acidic solutions, more than half of the disc product is detected around the onset of the first current plateau, which dropped down very soon as the disc potential increased, Figure 4-4(b) and (c). In all the investigated electrolytes, the ring currents always have the same onset potential as the disc current, though no plateau but two peaks are observed.

Raman spectroscopy on the disc electrode was then investigated to compare the difference of the deposited product on the electrode after the first and second plateau of the LSV curve of Mn^{2+} oxidation in pure 0.2 M Li_2SO_4 in Figure 4-4.

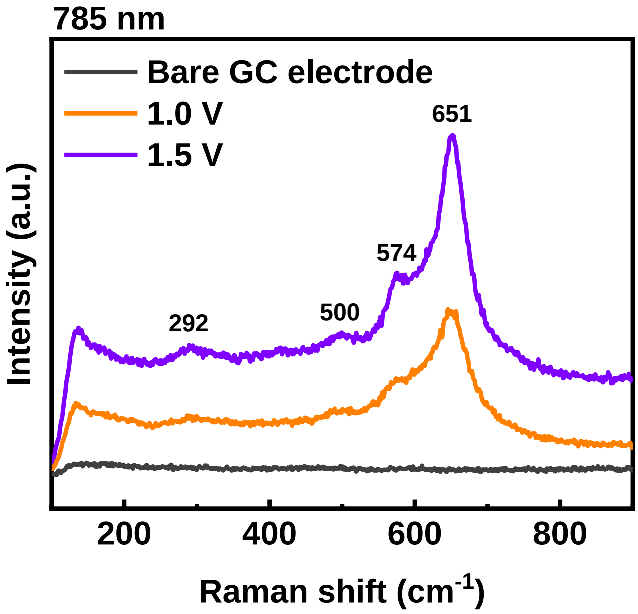

Figure 4-5. Raman spectra of the deposited film on the GC electrode after LSV of 1 mM Mn^{2+} from 0.3 V to 1.0 V (orange curve) or 1.5 V (purple curve) in 0.2 M Li_2SO_4, 10 mV s^{-1}. A fast rotation rate (2500 RPM) was applied to maximize the flux and the subsequent deposits for better Raman signals. Spectra from a bare GC electrode surface was added for comparison. All spectra were measured by 785 nm laser and taken under the same laser settings.

All three spectra show only two peaks at 1313 cm^{-1} and 1606 cm^{-1} beyond 900 cm^{-1} Raman shift, which result from the D-band and G-band from glassy carbon, respectively.[154] Thus, only spectra from 100 to 900 cm^{-1} are shown here, Figure 4-8(b). Films deposited at 1.0 V and 1.5 V showed peaks at the identical Raman shifts, though all peaks in the latter had higher intensities. Before taking the Raman spectra, a denser film was observed visually through the optical microscope after scanning the GC to 1.5 V. The most intense peak in both spectra is located at 651 cm^{-1}, which could possibly come from: 1) the $Mn^{2+}O_4$ tetrahedra ν_1 mode stretching vibration from α-Mn_3O_4; 2) the Mn-O ν_1 stretching vibration of $Mn^{4+}O_6$ octahedra from γ-MnO_2; 3) the combination of the two. The second intense peak at 574 cm^{-1} is assigned to the Mn-O ν_1 stretching vibration of $Mn^{3+}O_6$ octahedra from γ-MnO_2. Other weak peaks at 500 cm^{-1} and 292 cm^{-1} are attributed to ν_4 and ν_5 mode vibration of MnO_6 octahedra, respectively.[155–157] Overall, the Raman results suggest that the chemical composition of the films deposited after the first and second current plateaus are identical, which mainly contain γ-MnO_2 and may be mixed with some α-Mn_3O_4. No peak observed is assigned to MnOOH, thus, the oxidation of Mn^{2+} in pure 0.2 M Li_2SO_4 is very unlikely through Route 1 in Figure 4-3.

To understand the dominating process that contributed to the two plateaus, Koutecky-Levich analysis was conducted for the first plateaus in pure 0.2 M Li_2SO_4 and in 0.2 M Li_2SO_4 with 10 mM H_2SO_4 electrolytes, Figure 4-6. Each measurement was done after polishing the RRDE and both electrodes' state was checked by a quick CV scan in blank 0.2 M Li_2SO_4 without any Mn^{2+}.

In pure 0.2 M Li_2SO_4, Figure 4-6(a), the current grows proportionally with $\omega^{1/2}$ and maintains a classic sigmoidal shape up to 1600 RPM. When the electrode rotates faster than 2500 RPM, the current slightly decreases after passing by 0.9 V, and the spaces between the current traces get smaller with increasing rotation speed. In 0.2 M Li_2SO_4 with 10 mM H_2SO_4, Figure 4-6(e), the current shows a plateau-like shape only with the slowest rotation. With increasing rotation, a current peak at E_{disc} = 1.1 V becomes more obvious. Possibilities include the current being limited by a very sluggish reaction kinetics, or two reactions happening simultaneously between 1.0 to 1.2 V and their currents overlapping each other, or a combination of the two situations together. In both cases, it is possible that the scan rate used (10 mV s^{-1}) is too high to allow the current to reach the steady-state. However, slower scan rates may result in the Mn^{3+} becoming undetectable, as the ring current caused by Mn^{3+} shown in Figure 4-4 is already quite low.

As shown in Figure 4-6(b) and (f), the maximum current was taken to be considered as the limiting current for the reaction that dominated the first current plateau. For the reaction in 0.2 M Li_2SO_4 the limiting current at five rotation rates show a good linear relationship. However, in 0.2 M Li_2SO_4 with 10 mM H_2SO_4, only limiting current from the three slower rotation rates can be fitted linearly, meaning that up until 1600 RPM the reaction was still controlled only by diffusion, while when rotating faster, the reaction was limited by the kinetics.

When a single-step redox reaction with slow kinetics happens on a rotating disc electrode, if its plateau current is only limited by mass transport, then the relationship between the limiting current I_{lim} and several characteristics of the system can be described by Levich equation, Equation 2-15. The current I that is mixed controlled by kinetics and mass transport (i.e. the current before reaching the plateau) should follow the Koutecky-Levich equation, Equation 2-16,

By substituting the Equation 2-15 into Equation 2-16, Equation 4-2 can be obtained,

$$\frac{1}{I} = \frac{1}{I_k} + (\frac{1}{0.201nFAD^{2/3}\upsilon^{-1/6}C})\omega^{-1/2} \qquad \text{Equation 4-2}$$

Through plotting I_{lim} vs $\omega^{1/2}$ and $1/I$ vs $\omega^{-1/2}$, Levich and Koutecky-Levich equations are widely used for getting diffusion coefficient D and others including kinetic current I_k, electron transfer rate constant k, etc. if n is known and constant. Therefore, on the contrary, n could be calculated if the value of D is known.[76]

In pure 0.2 M Li_2SO_4, the current at E_{disc} = 0.9 V is assumed to be the plateau current since the current will maintain its steady-state value in ideal cases. In 0.2 M Li_2SO_4 with 10 mM H_2SO_4, the current at E_{disc} = 1.1 V is assumed to be the plateau current if there was only a very sluggish reaction, and the current at E_{disc} = 1.19 V is used in the case that more than one reaction happened simultaneously but only one reaction reached the steady state. The D values calculated from the Levich equation are summarized in Table 4-1. Besides, the self-diffusion coefficient of Mn^{2+} from aqueous $MnSO_4$ solutions measured by Patil et al.[159] and the calculated n by using this value is also shown in Table 4-1.

In pure 0.2 M Li_2SO_4, the calculated value of D is closer to the literature value when assuming n = 2. Whereas in 0.2 M Li_2SO_4 with 10 mM H_2SO_4, the estimated n is closer to 1.

The Koutecky-Levich plot for the Mn^{2+} oxidation in pure 0.2 M Li_2SO_4 and 0.2 M Li_2SO_4 with 10 mM H_2SO_4 are plotted in Figure 4-6(c) and (g). For the former, only the data points from 400 to 2500 RPM were used since the data from 3600 RPM is clearly not linearly related to the other four points. The slope of the fitted line decreases dramatically with more positive potential.

For the latter, all 5 different rotation speeds are included, though they do not show clear linear trends and the slope for the fitted lines fluctuates with the rising potential.

The calculated n (by using the literature D) in both electrolytes from the Koutecky-Levich equation is plotted in Figure 4-6(d) and (h), and the calculated electron transfer rate constant k based on assuming a known n is listed in Table 4-2.

As shown in Table 4-2, in both electrolytes, the electron transfer rate constants k are considered to be medium to fast no matter the assumed electron transfer number n. This results in the fact that the shapes of the current in Figure 4-6(a) and (e) are partly not independent of rotation rate ω, and the slopes of the fitted line in the Koutecky-Levich plots as well as the subsequently calculated number of electrons transferred, are dependent of the electrode potential. The electron transfer number n is scattered between 0 to 2. Besides, in the case of Mn^{3+} is yielded, the instability of Mn^{3+} may cause the reverse reaction of $Mn^{2+} \rightarrow Mn^{3+}$ to become not negligible, which further results in inaccuracy when applying Koutecky-Levich analysis. Thus, it is hard to conclude the electron transfer number from this method on its own.

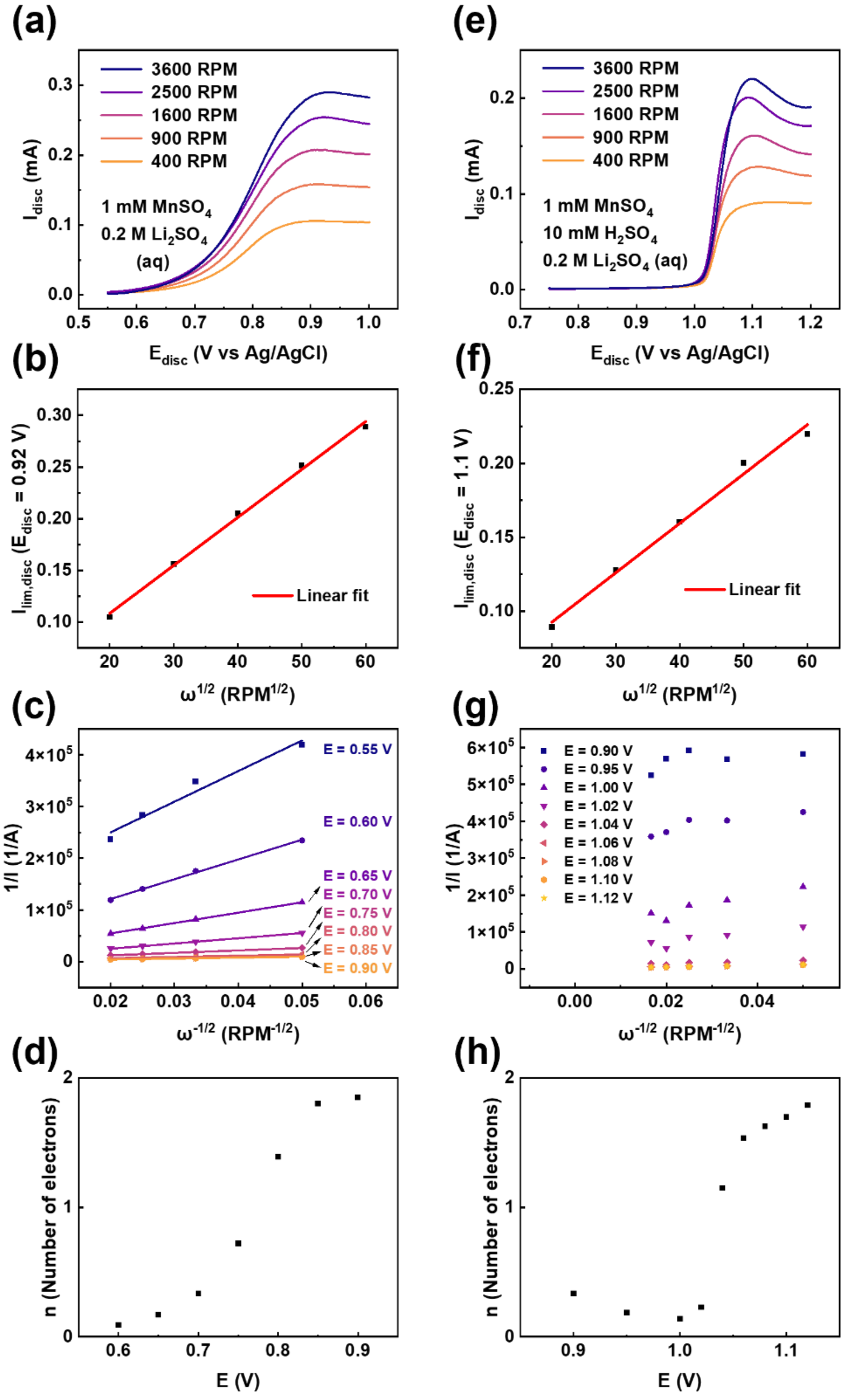

Figure 4-6. Rotating disc voltammograms of 1 mM Mn^{2+} on GC disc electrode in (a) 0.2 M Li_2SO_4 and (e) 0.2 M Li_2SO_4 with 10 mM H_2SO_4, anodic scan, 10 mV s^{-1}, rotation rates indicated in the graph. The Corresponding Levich plot for disc limit current in (a) and (e): (b) in 0.2 M Li_2SO_4 and (f) 0.2 M Li_2SO_4 with 10 mM H_2SO_4. Koutecky-Levich plot for Mn^{2+} oxidation curves: (c) in 0.2 M Li_2SO_4 at disc potential E_{disc} = 0.55 V, 0.60 V, 0.65 V, 0.70 V, 0.75 V, 0.80 V, 0.85 V, 0.90 V, and for (g) in 0.2 M Li_2SO_4 with 10 mM H_2SO_4 at disc potential E_{disc} = 0.90 V, 0.95 V, 1.00 V, 1.02 V, 1.04 V, 1.06 V, 1.08 V, 1.10 V, 1.12 V. Number of electrons transferred vs disc potential calculated from Koutecky-Levich analysis (d) in 0.2 M Li_2SO_4 and (h) in 0.2 M Li_2SO_4 with 10 mM H_2SO_4.

Table 4-1. Comparison of the diffusion coefficient D calculated from Levich equation by assuming a known electrons transfer number n.

	Pure 0.2 M Li_2SO_4	0.2 M Li_2SO_4 with 10 mM H_2SO_4	
$E_{plateau}$ (V)	0.90	1.1	1.19
	D (m^2 s^{-1})		
Assuming n = 1	1.34×10^{-9}	8.14×10^{-10}	5.38×10^{-10}
Assuming n = 2	4.75×10^{-10}	2.88×10^{-10}	1.90×10^{-10}
Literature Value	6.80×10^{-10} ($[Mn^{2+}]\approx1$ mM)[159]		
	Estimated n by using the literature D		
	1.57	1.13	0.86

Table 4-2. Calculated electron transfer rate constant k by assuming n is known and constant.

Pure 0.2 M Li_2SO_4						
E_{disc} (V)	0.65	0.70	0.75	0.80	0.85	0.90
k (cm s^{-1}) Assuming n = 1	3.72×10^{-3}	1.16×10^{-2}	1.95×10^{-2}	3.21×10^{-2}	7.28×10^{-2}	1.95×10^{-1}
k (cm s^{-1}) Assuming n = 2	1.86×10^{-3}	5.81×10^{-3}	9.76×10^{-3}	1.61×10^{-2}	3.64×10^{-2}	9.76×10^{-2}
0.2 M Li_2SO_4 with 10 mM H_2SO_4						
E_{disc} (V)	1.02	1.04	1.06	1.08	1.10	1.12
k (cm s^{-1}) Assuming n = 1	1.31×10^{-3}	6.67×10^{-3}	2.37×10^{-2}	4.40×10^{-2}	4.79×10^{-2}	3.75×10^{-2}
k (cm s^{-1}) Assuming n = 2	6.56×10^{-4}	3.34×10^{-3}	1.19×10^{-2}	2.20×10^{-2}	2.39×10^{-2}	1.88×10^{-2}

Figure 4-7(a) and (d) show the potential step experiment to the potential where Mn^{2+} oxidation reaches their first plateau current (in Figure 4-4) in both 0.2 M Li_2SO_4 and 0.2 M Li_2SO_4 with 10 mM H_2SO_4 electrolytes after holding the potential at OCP in each condition for 10 s. If the process is limited by mass transport only, the current I (A) and time t (s) should follow the Cottrell Equation, Equation 4-3:

$$I = nFAD^{1/2}C\pi^{-1/2}t^{-1/2} \qquad \text{Equation 4-3}$$

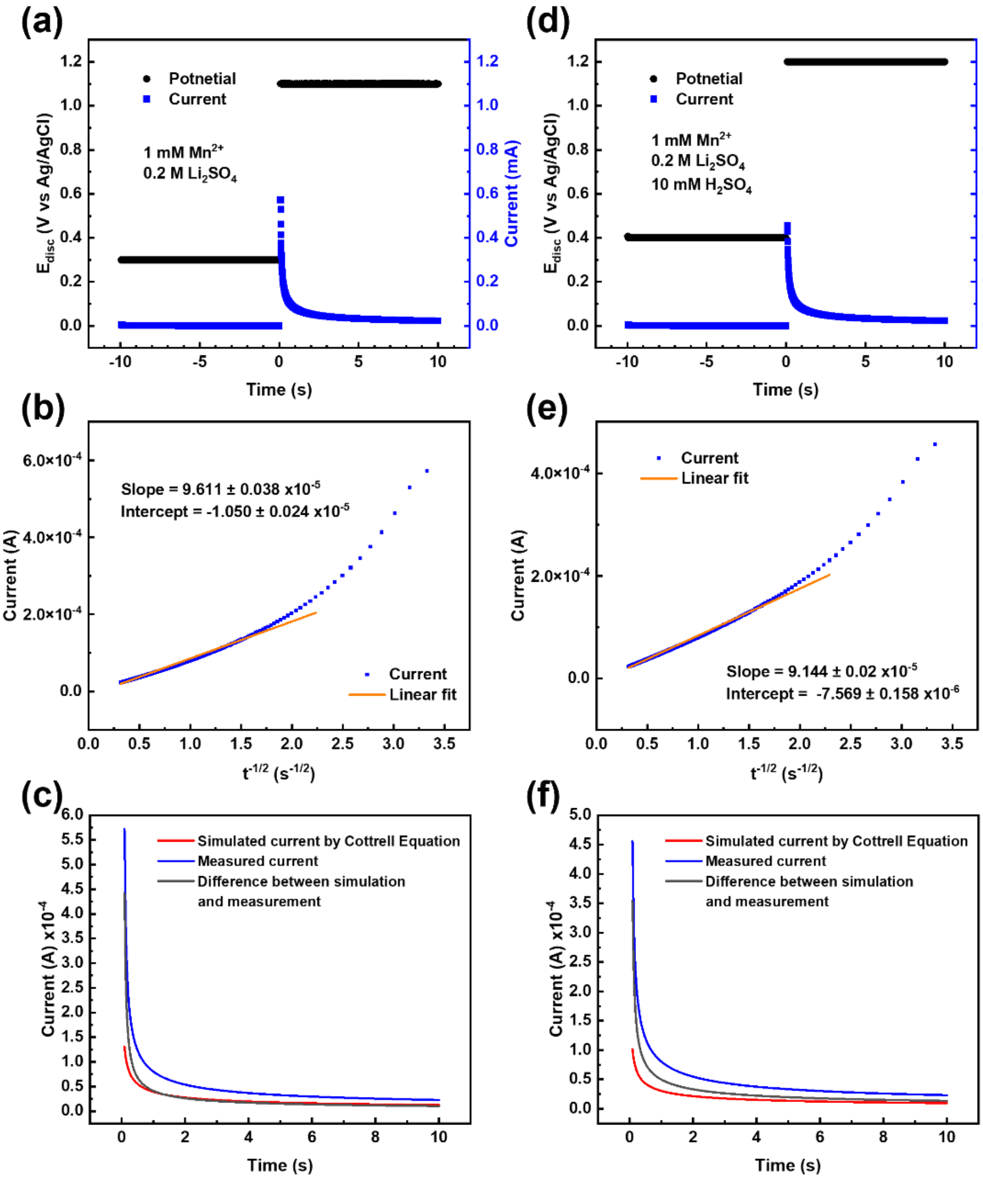

Figure 4-7. Potential step experiment of 1 mM Mn^{2+} on stationary GC disc electrode in 0.2 M Li_2SO_4: (a) potential and current vs time; (b) current and its linear fit vs $t^{-1/2}$ after stepping to the 1st plateau potential in Figure 4-4; (c) the comparison of simulated current by Cottrell Equation, the measured current, and their difference. Potential step experiment of 1 mM Mn^{2+} on stationary GC disc electrode in 0.2 M Li_2SO_4 with 10 mM H_2SO_4: (d) potential and current vs time; (e) current and its linear fit vs $t^{-1/2}$ after stepping to the 1st plateau potential in Figure 4-4; (f) the comparison of simulated current by Cottrell Equation, the measured current, and their difference.

By plotting the I vs $t^{-1/2}$, Figure 4-7(b) and (e), the diffusion coefficient D can be calculated through the slope, which are 8.09×10^{-9} m^2 s^{-1} and 7.32×10^{-9} m^2 s^{-1} in 0.2 M Li_2SO_4 and 0.2 M Li_2SO_4 with 10 mM H_2SO_4 electrolytes, respectively. In both electrolytes, the diffusion coefficient D values calculated from Levich analysis when assuming electron transfer number n = 1 are closer to the value obtained from Cottrell analysis, suggesting that a 1-electron transfer process (i.e. $Mn^{2+} \rightarrow Mn^{3+}$) is very likely dominating the first current plateau in Figure 4-4. However, as suggested by Figure 4-4(c), the processes during the first current plateau in both electrolytes are not only limited by mass transport, which makes the Cottrell analysis alone inconclusive.

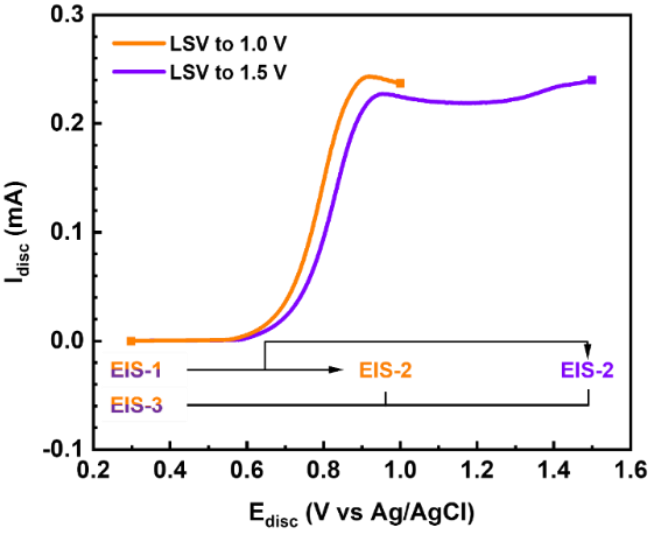

Figure 4-8. (a) Schematic experimental protocols for the EIS measurements. Rotation rates: 2500 RPM.

As such, considering the slope of the disc current before reaching the first plateau in Figure 4-4, the $Mn^{2+} \rightarrow Mn^{3+}$ electron transfer rate first increased (from 0 mM to 10 mM H_2SO_4, i.e., pH decreases from neutral to 2) and then decreased (from 10 mM to more H_2SO_4, i.e., pH below 2). Moreover, in both electrolytes shown in Figure 4-6, a current peak appears with fast rotation rates instead of a plateau, suggesting a film began to grow and block the electrode, which then decreased the electron transfer rate of $Mn^{2+} \rightarrow Mn^{3+}$. With the rotation rate increasing, the film deposited faster and more current decreases were observed. Additionally, as shown in Figure 4-7(c) and (f), in both electrolytes, the measured current is higher than the Cottrell Equation predicted current, suggesting that either the Mn^{2+} can be oxidised on this film at such potential, or generated Mn^{3+} oxidation is also contributing to the current detected in this experiment.

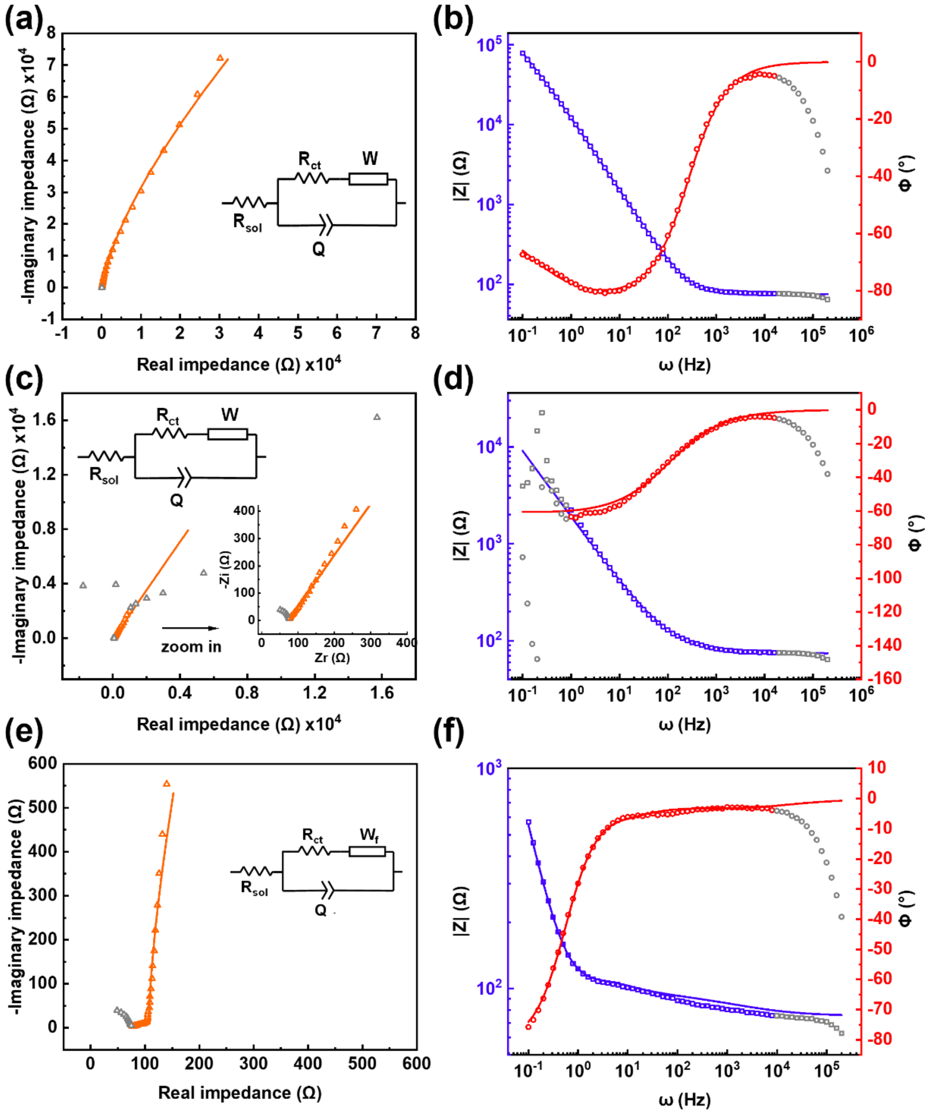

Figure 4-9. Comparison of EIS data at different E_{disc} before and after applying LSV on the disc from 0.3 V to 1.0 V: (a) Nyquist and (b) Bode plots of 1.0V-EIS-1 (E_{disc} = 0.3 V); (c) Nyquist and (d) Bode plots of 1.0V-EIS-2 (E_{disc} = 1.0 V); (e) Nyquist and (f) Bode plots of 1.0V-EIS-3 (E_{disc} = 0.3 V). The insets show the equivalent circuit used for data analysis. Rotation rates: 2500 RPM.

To further study the process that dominates the current plateau at 1.0 V and 1.5 V in pure 0.2 M Li_2SO_4 in Figure 4-4, EIS measurements were then performed in the frequency range from 0.1 Hz to 10 kHz to compare the two processes, Figure 4-8. All data can be fitted by a Randles equivalent circuit in addition to an infinite Warburg element W except for the data from 1.0V-

EIS-3, where a finite Warburg element W_f was used instead, Figure 4-9 and Figure 4-10. The element R_{sol} in the circuit represents the uncompensated solution resistance. R_{ct} is the resistance for the charge transfer process and Q is the constant phase element (CPE) that associates with the capacitance associated with the faradic process of the electrode surface under AC conditions.[160,161]

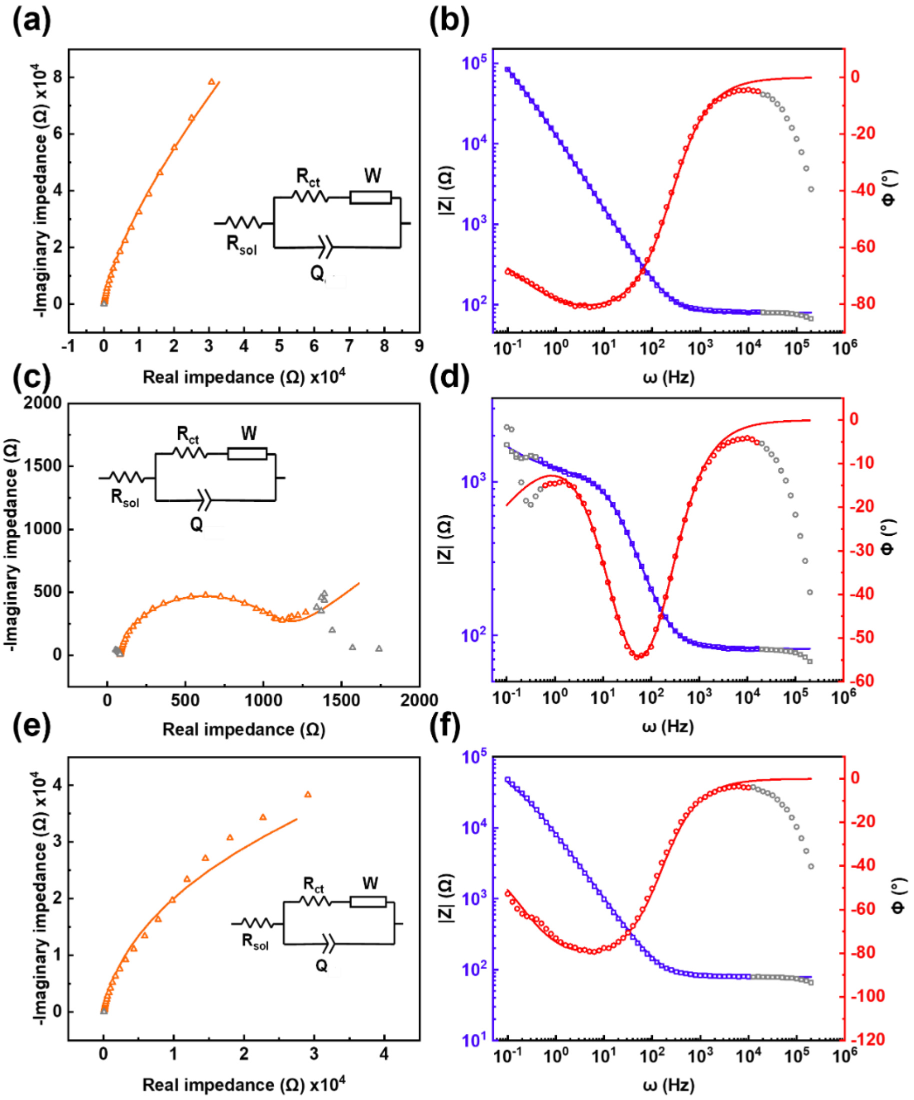

Figure 4-10. Comparison of EIS data at different E_{disc} before and after applying LSV on the disc from 0.3 V to 1.5 V: (a) Nyquist and (b) Bode plots of 1.5V-EIS-1 (E_{disc} = 0.3 V); (c) Nyquist and (d) Bode plots of 1.5V-EIS-2 (E_{disc} = 1.5 V); (e) Nyquist and (f) Bode plots of 1.5V-EIS-3 (E_{disc} = 0.3 V). The insets show the equivalent circuit used for data analysis. Rotation rates: 2500 RPM.

Compared with the initial state 1.0V-EIS-1, the Q increased more than an order of magnitude, and R_{ct} decreased around 4 orders of magnitude in 1.0V-EIS-3, suggesting the surface is changed after E_{disc} were scanned to 1.0 V. Whereas, for 1.5V-EIS-1 and 1.5V-EIS-3, the changes in Q and R_{ct} were less obvious, indicating that the electrode surface was either recovered slightly toward its initial state after went to 1.5 V. Compare 1.0V-EIS-2 with 1.5V-EIS-2, the R_{ct} of the latter is around 3 times smaller and Q is almost 10 times bigger, which confirmed that the dominating processes happening at disc potential of 1.0 V and 1.5 V are different. Overall, in the spectrum from scanning the disc potential to 1.0 V, the R_{ct} value keeps decreasing, meaning that there is still a redox process ongoing even when the E_{disc} is scanned back to 0.3 V (i.e. OCP). For the three from scanning E_{disc} to 1.5 V, the R_{ct} was first decreased two orders of magnitude, then grew up again, suggesting the redox process was no longer obvious when E_{disc} was back to 0.3 V.

Table 4-3. Parameters extracted from the EIS data through fitting with the equivalent circuits.

Element (unit)	1.0V-1	1.0V-2	1.0V-3	1.5V-1	1.5V-2	1.5V-3
Q ($\mu s^{\alpha}(\Omega\cdot cm^2)^{-1}$)	74.92	686.00	1914.21	70.43	74.89	107.58
α ($\Omega\cdot cm^2$)	0.92	0.70	0.57	0.93	0.93	0.93
R_{sol} ($\Omega\cdot cm^2$)	14.70	14.54	14.70	15.65	16.08	15.41
R_{ct} ($\Omega\cdot cm^2$)	18177.53	61.44	3.52	19043.03	194.66	9248.24
W / W_f ($k\Omega\cdot cm^2 (\sqrt{s})^{-1}$)	22.97	11.04	0.03	26.74	0.12	5.08
B_o ($\delta (\sqrt{D})^{-1}$)			0.35			
χ^2	0.03	0.12	0.05	0.02	0.03	0.12
C ($\mu F\ cm^{-2}$)	167.81	312.65	97.39	83.00	63.04	122.70
d (nm)		0.19	0.62		0.95	0.49

Assuming that the deposited film is evenly distributed on the electrode surface, the film thickness d can be calculated through Equation 4-4,[162]

$$C_{ct} = \varepsilon_0 \varepsilon_r \frac{A}{d} \qquad \text{Equation 4-4}$$

where $\varepsilon_0 = 8.85 \times 10^{12}$ (F m^{-1}) is the vacuum electric permittivity; ε_r is the relative permittivity for the film, which is 68.1 ± 1.6 for MnO_2;[163] A is the surface area of the electrode (m^2); C_{ct} (F m^{-2}) is the equivalent capacitance converted from CPE.

As summarized in Table 4-3, for the data sets obtained from scanning the E_{disc} to 1.0 V, the film begins to be deposited when the potential reaches 1.0 V, and the thickness of the film continues to increase even when the potential is scanned back to 0.3 V. For the data set obtained from scanning the E_{disc} to 1.5 V, d reaches the peak value at 1.5 V, then decreases when going back to 0.3 V, indicating that either the film dissolves or there might be crystal structure changes that happened, thus the film becomes more condensed. In both cases, the extremely small thickness of the film suggests that the electrode was only partially covered by the film.

Combining the results from these techniques, it is reasonable to conclude that the first plateau (1.0 V) of the LSV curve of Mn^{2+} oxidation in pure 0.2 M Li_2SO_4 in Figure 4-4 can be attributed to Route 2 in Figure 4-3. Whereas, the second plateau (1.5 V) is caused by Route 3. Therefore, Mn^{3+} can be generated through oxidising Mn^{2+} on the GC disc electrode and can survive a short time in the electrolyte in order to be detected by the Pt ring electrode. Moreover, any potential that is not positive than 0.3 V vs Ag/AgCl on the platinum ring electrode should be able to reduce Mn^{3+}.

4-3.2 Detection of Mn dissolution from LMO

To study the Mn dissolution from LMO, RRDE collection experiments were performed. Freshly prepared LMO was cycled between -0.8 V to 1.5 V, and showed identical voltammograms each time. Before and after applying CV on LMO, it is stabilized in a 10-minute' OCP period, while a constant potential is applied to the Pt ring electrode throughout the whole process. The LMO shows two pairs of Li^+ insertion/extraction peaks at 0.73/0.88 V and 0.59/0.72 V, which agrees well with literature value in the same electrolyte but different cell geometries, suggesting the current is mainly limited by the Li^+ diffusion in the LMO. [164,165]

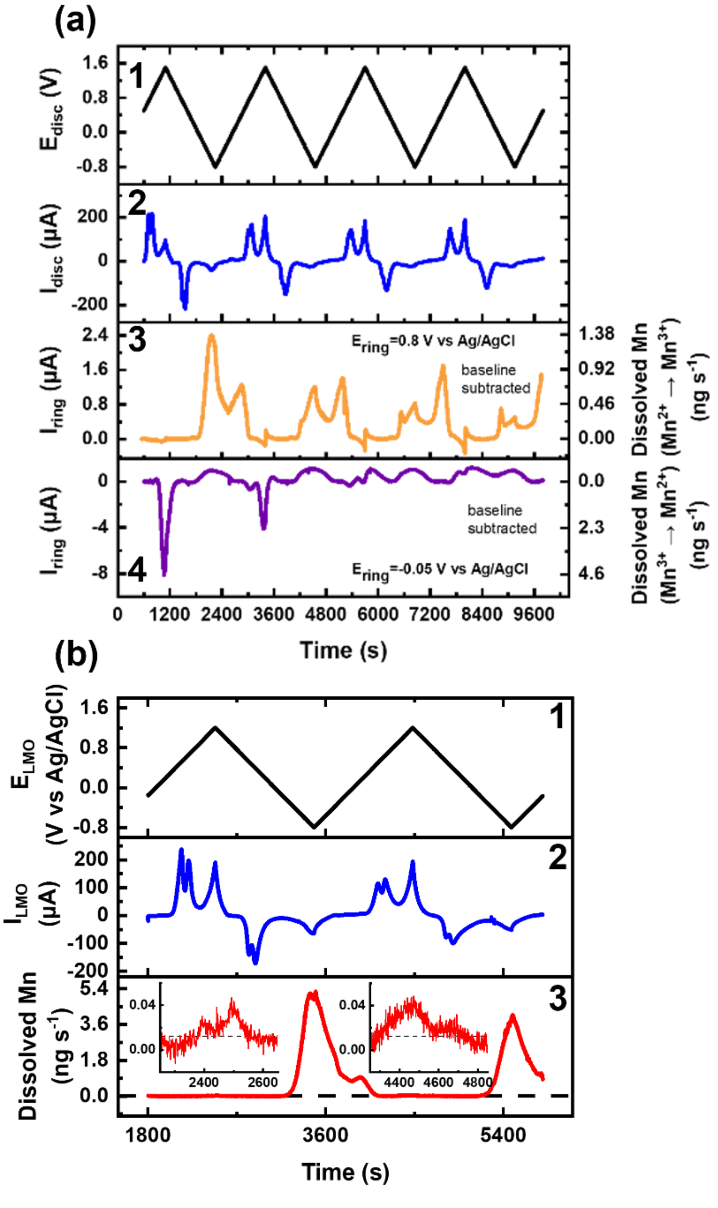

Figure 4-11. (a) RRDE collection experiments for detecting the Mn dissolution rate by applying CV on the LMO and chronoamperometry on the ring: (panel 1 and 2) Disc potential and current versus time, 2 mV s^{-1}; (panel 3 and 4) ring current, the corresponding ring potential are indicated in each panel. The electrode was kept rotating at 400 RPM. (b) Potential, current, and Mn dissolution of LMO detected by online ICP-OES.

The Mn dissolution rate m_{Mn} can be converted from the detected current via Equation 4-5,

$$m_{\mathrm{Mn}} = \frac{IM_{\mathrm{Mn}}}{zFA} \qquad \text{Equation 4-5}$$

where I is the instant current (A); M_{Mn} is the atomic molar mass of Mn (54.94 g mol^{-1}); z is the number of electrons transferred when detecting the dissolved Mn on the ring; and all other variables have the same meaning as stated before.

During the initial lithiation, no matter the held ring potential, no obvious ring current is detected that corresponds to the redox peaks of LMO, indicating no Mn dissolution. When the LMO is scanned positive than 1.1 V, Mn^{3+} is detected through the reduction current by holding the $\mathrm{E}_{\mathrm{ring}}$ = -0.05 V. The dissolution rate of Mn^{3+} reaches the maximum value of 4.44 ng s^{-1} when $\mathrm{E}_{\mathrm{disc}}$ = 1.45 V. Taking into account the collection efficiency of the electrode at this rotation rate, the true maximum value for dissolved Mn^{3+} should be 15.70 ng s^{-1}.

During the first cathodic scan, no obvious Mn dissolution was found until $\mathrm{E}_{\mathrm{disc}}$ passed 0 V, where Mn^{2+} was found by the ring oxidation current when holding the $\mathrm{E}_{\mathrm{ring}}$ = 0.8 V, and then the dissolved Mn^{2+} increased to its maximum of 1.37 ng s^{-1} when $\mathrm{E}_{\mathrm{disc}}$ = -0.61 V. Considering the collection efficiency of the RRDE used, the true maximum amount of the dissolved Mn^{2+} should be 4.84 ng s^{-1}. The dissolution rate after that shows a decreasing trend until the $\mathrm{E}_{\mathrm{disc}}$ scanned back to -0.2 V in the following anodic scan and reaches another peak of 2.51 ng s^{-1} when $\mathrm{E}_{\mathrm{disc}}$ = 0.41 V. After that, the Li^{+} insertion current starts growing, and the dissolution rate drops back to around zero when the current of LMO reaches its first peak.

In the following cycles, the two pairs of Li^{+} insertion/extraction peaks for LMO decrease gradually and shift toward each other until becoming not distinguishable in the 4th cycle. The O_2 evolution current at above 1.3 V becomes more obvious. As for the ring current, in the second cycle, the amount of dissolved Mn^{3+} in the overcharged region is reduced to about half of that in the first cycle, and becomes almost undetectable from the third cycle onwards.

Simultaneously, in the second and third cycles, a slight current shoulder caused by Mn^{3+} dissolution is detected together with the Li^+ extraction peaks of LMO. The Mn^{2+} dissolution peak that appears during the cathodic scan gradually decreases and splits into two peaks in the following cycles, one of which peaked at E_{disc} = -0.16 V, and the other one shifted towards the negative vertex potential. While the Mn^{2+} dissolution peak at E_{disc} = 0.41 V keeps rising and shifts positively together with the first anodic peak of LMO.

The same amount of LMO was drop-cast on a GC wafer electrode and the Mn dissolution was detected by the online ICP-OES system described in our previous work.[165] The Mn dissolution detected by the two methods shows identical trends, though the amounts are different.

The CV of LMO in the flow cell that coupled with ICP-OES shows identical redox peaks to that demonstrated in RRDE measurements, Figure 4-11.

The dissolved Mn detected by online ICP-OES upon the end of charging should correspond to the reduction current in the RRDE measurement when E_{ring} was held at -0.05 V, which is caused by Mn^{3+}. The amount of Mn detected by online ICP-OES is less than that detected by RRDE, which may be due to the following reasons: 1) A longer pre-OCP (30 min) was applied in the online ICP-OES measurement than in the RRDE measurement (10 min), which may allow more Mn^{3+} on LMO surface to dissolve or disproportionate already during OCP; 2) Since the main dissolving species Mn^{3+} can disproportionate rapidly once getting into the electrolyte as described by Figure 4-3 route 2, it may not able to survive to be detected by ICP-OES. Therefore, it is reasonable to estimate that only half of the dissolving Mn is detected in this region; 3) Mn oxides are good catalysts for water splitting,[166,167] it is possible that the generated O_2 can be reduced under such E_{ring}. The small oxidation waves are probably generated by the by-products of water splitting.

The first dissolution peak that initiated during the cathodic scan detected by online ICP-OES should correspond to the Mn^{2+} detected by RRDE, whereas the second peak corresponds the the mixture of Mn^{2+} and Mn^{3+}. The amount of Mn detected by online ICP-OES has the maximum value of 5.26 ng s^{-1} when E_{LMO} = -0.57 V in the first cycle, followed by another peak value of 0.95 ng s^{-1} when E_{LMO} = 0.36 V. Overall, the Mn dissolution during (over)discharging and the following initial charging detected by the two methods show the same characteristics including one peak close to the negative vertex potential and another peak just before the redox peak of LMO, though the total amount of Mn detected by online ICP-OES is slightly less than that detected by RRDE, which is probably resulted by the instability of Mn^{3+}.

$$\mathrm{Li_aMn_2O_4 \rightarrow aLi^+ + MnO_2 + Mn^{3+} + (3 + a)e^-} \quad (a < 1) \qquad \text{Equation 4-6}$$

$$\mathrm{3LiMn_2O_4 + Li^+ + 5e^- + 8H^+ \rightarrow 2Li_2Mn_2O_4 + 2Mn^{2+} + 4H_2O} \qquad \text{Equation 4-7}$$

$$\mathrm{2Li_bMn_2O_4 + 8H^+ + (4 - 2b + c)e^- \rightarrow (2b - c)Li^+ + 2Mn^{2+} + Li_cMnO_2 + 4H_2O} \quad (2 > b > 1 > c) \qquad \text{Equation 4-8}$$

$$\mathrm{2Li_bMn_2O_4 \rightarrow (2b - c)Li^+ + 2Mn^{2+} + Li_cMn_2O_4 + 2O_2 + (2b - c + 4)e^-} \quad (2 > b > 1 > c) \qquad \text{Equation 4-9}$$

$$\mathrm{2Li_cMn_2O_4 \rightarrow (2c - d)Li^+ + Mn^{2+} + Mn^{3+} + Li_dMnO_2 + (2c - d + 5)e^-} \quad (1 > c > d > 0) \qquad \text{Equation 4-10}$$

Our results suggest that during the first cycle, Mn^{3+} only dissolves when LMO approaches the end of charging, Equation 4-6, and Mn^{2+} starts to dissolve when LMO is overdischarged, Equation 4-7. In the subsequent anodic scans (from $Li_2Mn_2O_4$ to MnO_2), Mn^{2+} is kept released until LMO reaches its first oxidation peak again, Equation 4-8 or Equation 4-9. While the dissolved amount of Mn^{3+} starts to grow together with the first LMO oxidation peak, Equation 4-10.

Our results agree with some studies in $LiPF_6$-based carbonates eletrolytes, where their samples were taken from LMO-graphite cells cycled between 3.0-4.2 V (in our potential range, this should be 0.0-1.2 V vs Ag/AgCl), they believe that the ratio of dissolved Mn^{2+} to Mn^{3+} is close to 1:1.[51,136] While the NMR study shows that only Mn^{2+} dissolves, this is probably because their powder was only soaked in the electrolyte without any cycling.[50]

4-4 Conclusions

By using RRDE, KL analysis, EIS, and Raman, we studied the electrochemical behaviour of Mn^{2+} and Mn^{3+} in aqueous 0.2 M Li_2SO_4 electrolyte on GC and Pt electrodes. We confirmed the oxidation process of Mn^{2+} on a GC electrode is that $Mn^{2+}\rightarrow Mn^{3+}\rightarrow Mn^{2+}+MnO_2$, followed by $Mn^{2+}\rightarrow Mn^{3+}\rightarrow Mn^{4+}\rightarrow MnO_2$. Thus, Mn^{3+} was locally generated in a RRDE setup and studied. Then, the mechanism of Mn dissolution from LMO was analyzed by RRDE and online ICP-OES. Our results suggest that, in the first delithiation process, Mn^{3+} dissolves only when LMO approaches the end of charging (above 1.1 V vs Ag/AgCl, i.e. 4.1 V vs Li^+/Li). Mn^{2+} dissolution is initiated from the end of discharge, and can last until the $LiMn_2O_4$ is recovered from $Li_2Mn_2O_4$ and starts to delithiate again. While the Mn^{3+} dissolution launches again together with the first LMO oxidation peak.

Chapter 5. Dynamic phase transformation of $LiNi_{0.5}Mn_{1.5}O_4$ as Li-ion cathode observed by *operando* Raman spectroscopy

Spinel $LiNi_{0.5}Mn_{1.5}O_4$ (LNMO) is a promising alternative to $LiMn_2O_4$ (LMO) thanks to its high operation voltage and energy density. Meanwhile, with the addition of earth abundant Ni, the life span of the spinel is expected to be prolonged. However, the large-scale commercialization of LNMO is still limited by its premature ageing, including the decomposition of electrolyte, the dissolution of transition metal, and their subsequent influences on the electrode-electrolyte interfaces for both cathode and anode. A detailed understanding of the degradation process that happens on the cathode-electrolyte interphase (CEI) is the prerequisite for further material optimization. In this chapter, the chemical composition, morphology, crystal structure, and electrochemical properties of 2 commercial and 3 lab-synthesized LNMO are compared. Furthermore, their dynamic phase transformation during the initial cycle was investigated by *operando* Raman spectroscopy, aiming for insights into the CEI and its impact on the electrochemistry of LNMO. The experiments were initially designed to compare the electrochemical behaviour of LNMO and LMO in an aqueous electrolyte, as well as LNMO in both aqueous and organic electrolytes. However, LNMO exhibited very poor cyclability in the aqueous electrolyte, and further improvements could not be conducted due to time constraints.

I performed slurry mixing, coating, electrode preparation, coin cell assembly, electrochemical tests, X-ray diffraction analysis (XRD) of the powders, Raman spectroscopy for powders, and *operando* Raman cell assembly as well as the experiment conduction. The 3 lab-synthesized LNMO samples were gifts from Dr Li Zhang, who works in Dr Nuria Tapia-Ruiz's group at Imperial College London (UK). The scanning electron microscopy images were carried by Dr Bing Han from Dr Alexander Eggeman's group at The University of Manchester (UK). The X-ray diffraction was measured and analyzed with the help of Dr Zhenjiang Yu and Dr Hekang Zhu from Dr Xiao Hua's group at the Chemistry Department at Lancaster University. The *operando* Raman spectroscopy was set up with the help of Prof Yue Chen from Fujian Normal University (China).

5-1 Introduction

Spinel, represented by $LiMn_2O_4$ (LMO), is attractive thanks to its three-dimensional ion diffusion channels, which are expected to enable better lithium diffusion coefficient and structural stability.[168,169] However, resulting from the dissolution of transition metals together with other side reactions, LMO shows poor capacity retention, as discussed in the previous chapters. Replacing part of the Mn with other transition metals is assumed to be an effective way to enhance its performance.[170] Among the rest, spinel $LiNi_{0.5}Mn_{1.5}O_4$ (LNMO) is drawing increasing attention from researchers due to its high operation voltage (~4.7 V vs Li^+/Li), high theoretical energy density (650 W h kg^{-1}), low cost, good thermal stability, and environmental friendliness.[168,171] However, cycling and rate performances that are limited by premature ageing still require improvement for further commercialization

A better understanding of the degradation process and mechanism that occurs at the cathode-electrolyte interphase (CEI) is the key to improving batteries with LNMO cathodes.[172] Due to the high operating voltage, the electrolyte in cells with LNMO as the cathode is more likely to decompose than the electrolyte in that with other cathodes. Subsequently, both the CEI and the solid-electrolyte interphase (SEI) on the anode could be affected.[168,171,172]

Aurbach et al. confirmed the rise of the surface impedance of LNMO, which undertook prolonged cycling at 40-60 °C, resulting from the formation of LiF, C-F, $P-F_x$, and organic compounds-containing surface film by X-ray photoelectron spectroscopy (XPS). With the help of micro-Raman spectroscopy, they believed that the surface change of LNMO that cycled/stored at 60-70 °C was due to the dissolution of Mn and Ni and subsequent formation of λ-MnO_2.[173,174]

Kim et al. studied the Mn dissolution by storing the LNMO in the electrolyte (1 M $LiPF_6$ in ethylene carbonate (EC)/ ethyl methyl carbonate (EMC) with a 1:1 volume ratio) at 60 °C, and the electrolyte was then analyzed by ICP-MS. By using transmission electron microscopy (TEM) and time-of-flight secondary ion mass spectrometry (TOF-SIMS), they believed that the low concentration of NiO and MnO fragmentation ions and the presence of metal fluorides on the HF-etched (1% aqueous solution) LNMO surface is due to the Ni and Mn dissolution.[175]

Yang et al investigated the side reactions between LNMO and the electrolyte (1 M $LiPF_6$ in ethylene carbonate (EC)/ dimethyl carbonate (DMC)/ diethyl carbonate (DEC) in a volume ratio of 1:1:1) at different potentials between 4.0 V-5.3 V vs Li^+/Li. Their *ex-situ* X-ray photoelectron spectroscopy (XPS) and Fourier transform infrared spectroscopy with attenuated total reflectance (FTIR-ATR) results suggested that at potentials higher than 4.5 V, the EC could be oxidised to form poly(ethylenecarbonate) (PEC) on the CEI.[176]

Kim et al. compared the electrochemical behaviour of LNMO in half cell (with Li as the anode) and in full cell (with meso-carbon microbeads (MCMB) graphite as the anode) and suggested that the capacity fade in the full cell is led by both the dissolution of Mn, which is the dominating reason of the formation of SEI and subsequent Li^+ loss.[177]

Pieczonka et al. investigated the dependence of transition metal dissolution on the state of charge (SOC), temperature, storage time, and crystal structure of LNMO. By using the XPS depth profile, they found the deficiency of Ni and Mn on the cycled LNMO surface compared with the bulk, while Li showed a reversed trend. Their *ex-situ* X-ray fluorescence (XRF) spectrometry and gas chromatography (GC) results for the electrolyte suggested that both the Mn and Ni dissolution and the decomposition products of DEC grew with the increase of SOC, temperature, and storage time. In addition, the charged LNMO could be a catalyst for the electrolyte decomposition, while the products can in turn affect the Mn and Ni dissolution.[178]

Fehse et al. compared the bulk redox behaviour of ordered and disordered LNMO by *operando* dual-edge X-ray absorption spectroscopy and suggested that although the continuous oxidation of $Ni^{2+/3+/4+}$ and $Mn^{3+/4+}$ were observed in both, a better homogeneous of the reaction propagation was observed in the ordered LNMO. The transient formation of Ni^{3+} species showed positive dependence on the degree of local structural disorder in ordered LNMO compared with disordered LNMO.[179]

Overall, the degradation processes that happen at LNMO CEI play an essential role in the deterioration of the whole cell, and *operando* characterizations give important information for understanding these processes and the corresponding mechanism. Raman spectroscopy is an easy-access technique, which could provide extensive insights into the lattice symmetry, oxidation state, phase and grain information, defect, strains, etc. of the LNMO.[180,181]

Here, the chemical composition, morphology, crystal structure, and electrochemical properties of a series of LNMO were investigated by ICP-OES, scanning electron microscopy (SEM), X-ray diffraction (XRD), Raman spectroscopy, and galvanostatic (dis)charging. Two commercial LNMO (LNMO-S and LNMO-T) that were purchased from different suppliers were compared with three lab-synthesized samples, one of which was aimed for a disordered structure (LNMO-D) and the other two were doped by approximately 0.05 mol% of Fe (LNMO-Fe) and Mg (LNMO-Mg), respectively. Fe and Mg were chosen as the dopants to reduce the cost and enhance the structural stability.[238,239] The *operando* Raman spectroscopy was carried out during the initial charging and discharging of all 5 samples, and found that a fully delithiated phase could be formed reversibly to varying degrees on the surface of surfaces except for LNMO-Fe. No significant effect of the formation of this phase on the electrochemical performance of LNMOs was observed.

5-2 Experimental details

The 2 commercial LNMO powders were purchased from Sigman Aldrich (labeled as LNMO-S) and TOB New Energy (labeled as LNMO-T), respectively.

The powder XRD of all 5 samples was measured by a Rigaku SmartLab diffractometer equipped with a 9 kW Cu Kα source and a high-resolution vertical θ/θ 4-Circle goniometer plus D/teX-ULTRA 250 high-speed position-sensitive detector system. The powders were scanned from 5° to 90° for 30 min.

The SEM used in this chapter is a ZEISS GeminiSEM 2 field emission scanning electron microscope (FE-SEM), which features an energy dispersive X-ray spectrometry (EDS).

The electrode was prepared by mixing the LNMO powder: super P carbon (TOB New Energy): polyvinylidene fluoride (PVDF, TOB New Energy) in an 8:1:1 weight ratio in N-methylpyrrolidone (NMP, Sigma-Aldrich) using a Thinky mixer. The slurry was then coated on the Al foil by the doctor blade, followed by drying in an oven at 80℃ for 12 h and in a vacuum oven at 120℃ for another 12 h. The electrode was then cut into the desired size for the coin cell and the *operando* optical Raman cell. The 2032-coin cell parts were purchased from TOB New Energy. The Raman cell was an ECC-Opto-Std cell from EL-Cell, which is described in Chapter 2 in detail. The electrolyte used in all cells was a battery-grade lithium hexafluorophosphate solution (1.0 M $LiPF_6$ in EC/DMC=1/1 v/v) that was purchased from Sigma-Aldrich. The separator used in all cells were Whatman glass fiber.

A Neware battery testing system was used for all the electrochemistry tests in coin cell, and the electrochemical data during the *operando* Raman measurements were recorded by a BioLogic SP300 potentiostat. The Raman spectrometer used was a Renishaw inVia confocal Raman microscope that features 532 nm and 785 nm lasers, with 15 mW and 20 mW maximum power, respectively. The spectra were recorded by WiRE software and processed by SpectraGryph (version 1.2) software.

5-3 Results and discussion

5-3.1 Chemical composition and structure

Based on the distribution of Ni and Mn in the crystal structure, LNMO can usually be divided into ordered and disordered structures, though the two often coexist.[182] The former has a $P4_332$ space group, where Ni exists as Ni^{2+} and takes the 4a octahedra site, and Mn exists as Mn^{4+} and occupies the 12d site in the structure, Figure 5-1a. The latter has a space group of $Fd\bar{3}m$, where the Ni and Mn atoms randomly occupy the 16d site of the octahedra, Figure 5-1b.[183,184]

The molar ratio of the elements in each powder is determined by ICP-OES, Table 5-1. All the results are calculated by assuming the Mn content in each unit cell is 1.5. All samples show only small variations around the theoretical ratio of the material. The 3 LNMO samples without any dopants have similar Ni/Mn ratios, and the Li content negatively correlates to that of Ni. The addition of Fe and Mg reduces the concentration of Ni. Besides, the Mg concentration is slightly higher than that of Fe, though they were aimed for the same ratio.

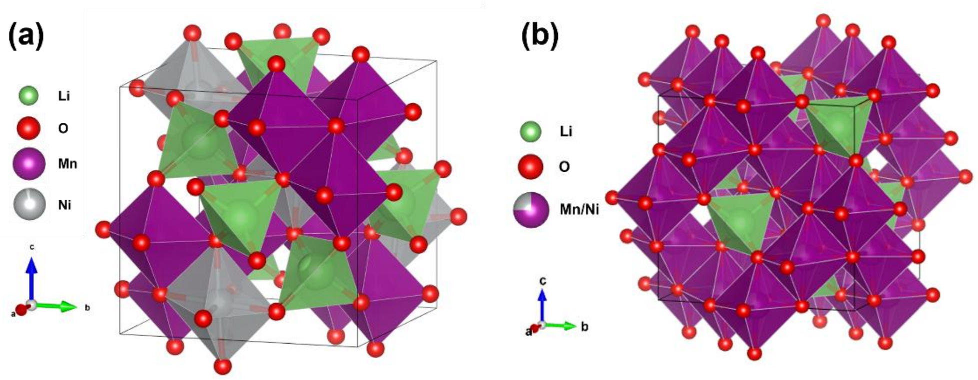

Figure 5-1. Schematic diagram of the crystal structure of (a) ordered ($P4_332$)[185] and (b) disordered ($Fd\bar{3}m$)[186] LNMO.

Table 5-1. Element ratio of the commercial and as-prepared LNMO powders detected by ICP-OES (assuming Mn = 1.5).

		Li	Ni	Mn	Fe	Mg
Commercial samples	LNMO-S	1.14	0.56	1.5		
	LNMO-T	1.25	0.54	1.5		
Lab-synthesized samples	LNMO-D	1.15	0.55	1.5		
	LNMO-Fe	1.14	0.48	1.5	0.051	
	LNMO-Mg	1.10	0.48	1.5		0.056

Figure 5-2 shows the SEM images of the 5 LNMO powders with different magnifications. The lab-synthesized LNMOs show different morphology from that of the commercial samples. LNMO-S demonstrates a spherical shape and relatively larger particle size compared with others and the surface of each sphere is very rough. The grain of LNMO-T was a mixture of octahedron, prism, and dodecahedron analogues and some flakes could be observed on its surface. The grains of the 3 lab-synthesized LNMOs are similar and all have irregular shapes.

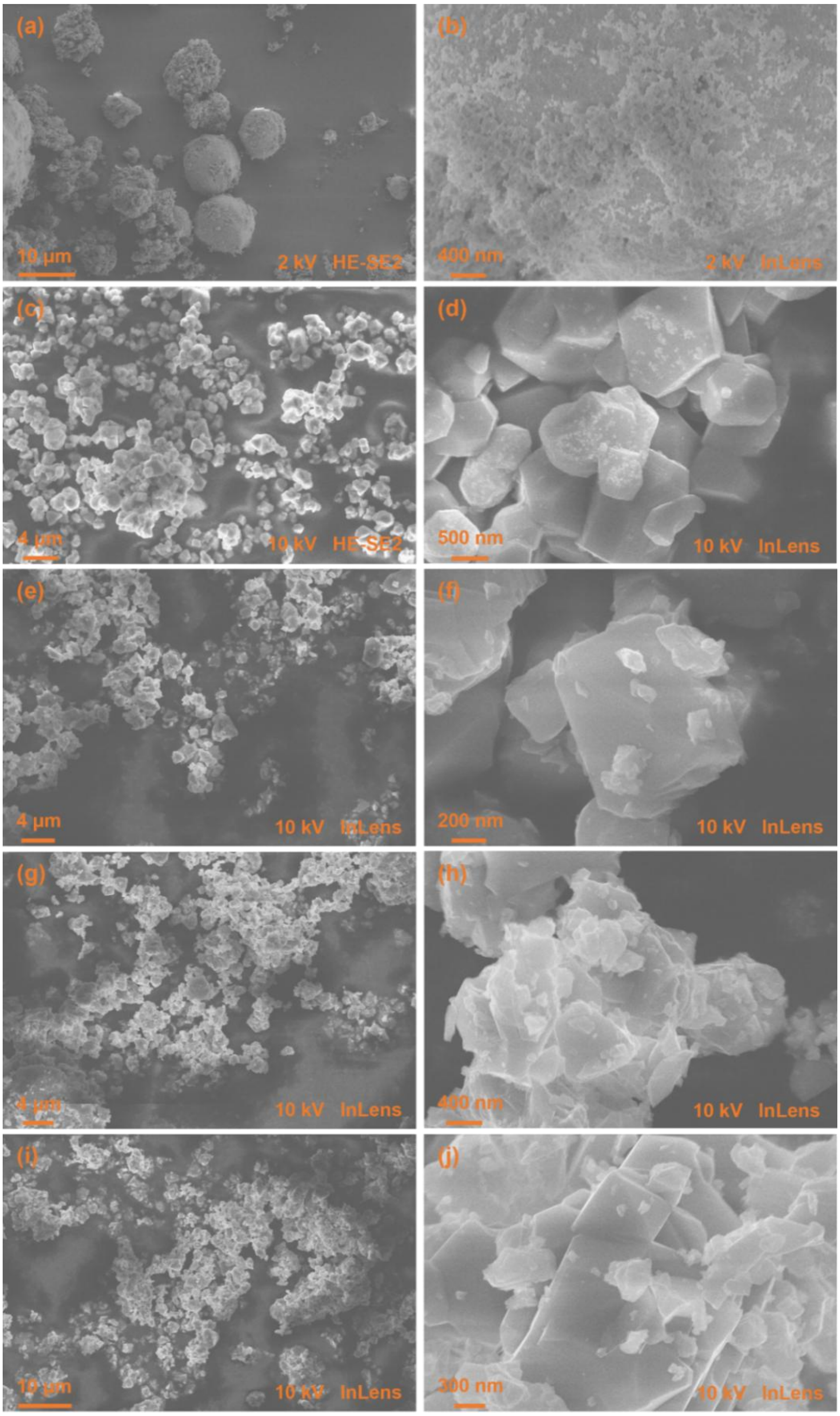

Figure 5-2. SEM images of the LNMO powders: (a-b) LNMO-S; (c-d) LNMO-T; (e-f) LNMO-D; (g-h) LNMO-Fe; (i-j) LNMO-Mg.

Powder XRD of the LNMO powders is shown in Figure 5-3. All 5 powders have sharp Bragg peaks and are in good agreement with the typical ordered or disordered spinel LNMO phases, suggesting good crystallinity.[187]

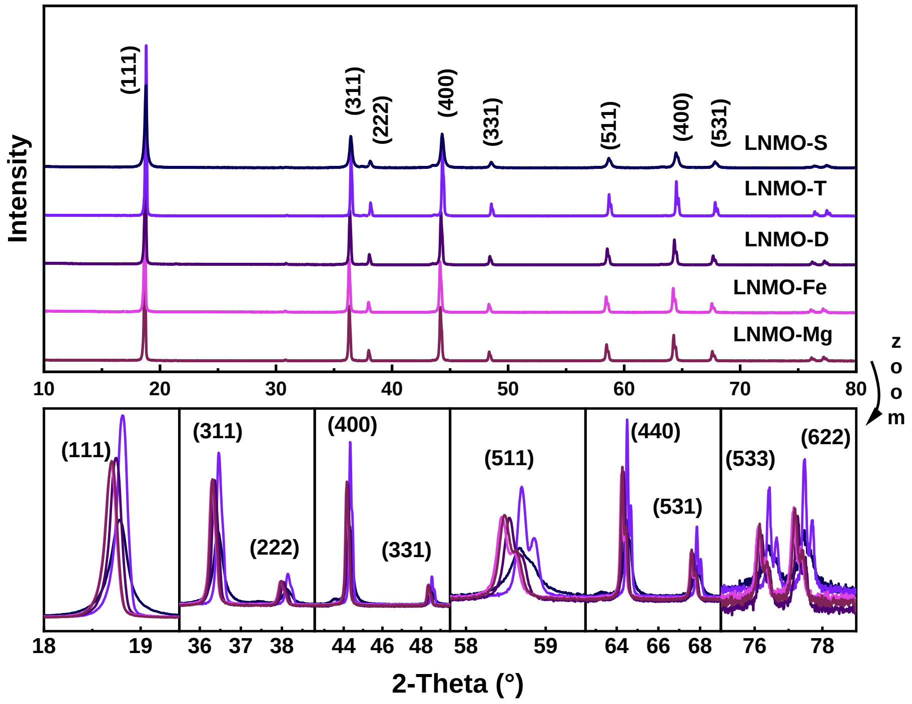

Figure 5-3. XRD data of the LNMO powders. Zoomed-in peaks are shown in the bottom panels.

Among all the powders, LNMO-T gives the most intense signal in all peaks, whereas LNMO-S shows the lowest and broader peaks. Compared with the commercial powders, the diffraction peaks of the lab-synthesized samples shifted to smaller angles, indicating larger lattice parameters, Table 5-2. This could be an indication that more Mn^{3+} (0.643Å) exists in the structures since it has a larger radius than Mn^{4+} (0.530 Å).[183]

Based on the Rietveld refinement of the XRD results, the main peaks of all the 5 LNMO powders can be indexed into the $Fd\bar{3}m$ space group, meaning that all samples are mainly dominated by the disordered structure in long-range. Except for the LNMO-Mg, the other LNMOs showed minor peaks at around 37.5°, 43.5°, 63°, which were caused by the undesired $Li_xNi_{1-x}O_2$ or NiO impurities.[188,189]

Table 5-2. Unit cell parameter of the LNMOs calculated from the Rietveld refinement of the XRD results.

	Unit cell parameter (a=b=c, Å)	Error (Å)
LNMO-S	8.16466	0.00018
LNMO-T	8.16369	0.00004
LNMO-D	8.17951	0.00005
LNMO-Fe	8.18677	0.00004
LNMO-Mg	8.18209	0.00004

Due to the similarity of Ni and Mn diffraction coefficients, it is hard to distinguish the ordered and disordered phases by XRD. Thus, Raman spectroscopy is employed to study the symmetry of the crystals, Figure 5-4.

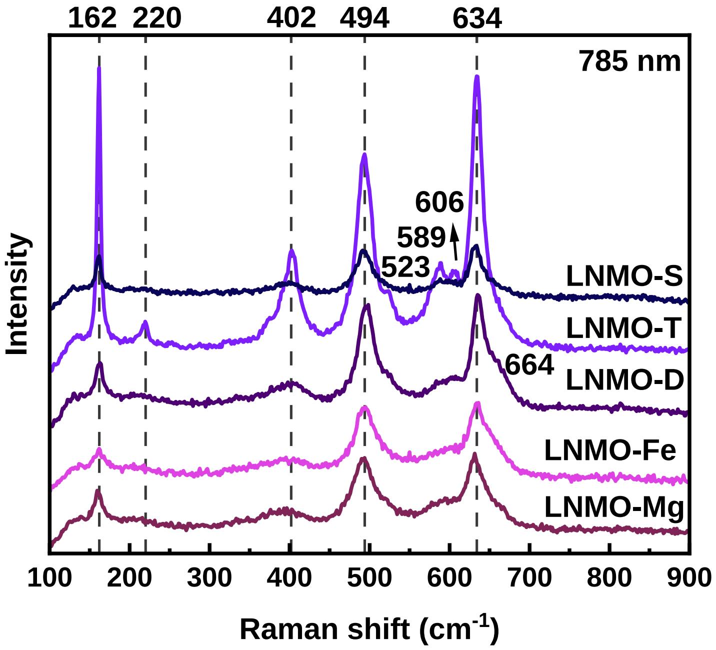

Figure 5-4. Raman spectra of the LNMO powders.

The most intense peak located at 634 cm^{-1} corresponds to the MnO_6 octahedra A_{1g} mode stretching vibration. The weak shoulder at 664 cm^{-1} beside this peak can be assigned to 16d site Ni/Mn-O bending vibration with $F_{2g}(3)$ symmetry, which could therefore indicate the disordered phase.[181] The peaks at 589 cm^{-1} and 606 cm^{-1} are the characteristics of the ordered LNMO phase and can be assigned to E symmetry and A_1 symmetry, respectively.[190,191] The peak at 402 cm^{-1} is caused by Ni^{2+}-O stretching vibration with E_g symmetry.[181] The peak at 494 cm^{-1} together with its tiny shoulder at 523 cm^{-1} can be assigned to $F_{2g}(2)$ mode pure Ni-O stretching vibration, and their position and intensity are suggested to be dependent on the oxidation state of Ni.[181,192] The bands at 162 cm^{-1} and 220 cm^{-1} can be assigned to $F_{2g}(1)$ mode translational lattice vibration, which could indicate the ordered LNMO phase.[181,190,193]

All 5 powders have peaks with similar bands but different intensities. In general, LNMO-T has the most intense peaks, meaning the highest crystallinity among others. The peaks at 162 cm^{-1}, 220 cm^{-1}, 589 cm^{-1}, and 606 cm^{-1} suggest that the LNMO-T has more ordered structures compared with others. The band at 664 cm^{-1} is only observable from the spectra of the 3 lab-synthesized samples, indicating the formation of disordered phases. The peaks around 634 cm^{-1} of the five samples are arranged in the order of LNMO-Mg < LNMO-S < LNMO-T < LNMO-D < LNMO-Fe from small to large shift, suggesting the lengths of the Mn-O bond also follow this order from long to short.[192] It is hard to distinguish the dopants from the spectra, meaning that they are not likely aggregated in the surface but spread in the bulk.

5-3.2 Electrochemistry

5-3.2.1 LNMO-S

LNMO-S shows three plateaus during the initial (dis)charging, one at around 4.0 V and others at around 4.7 V vs Li^+/Li, Figure 5-5(a). Though it reached 146.15 mAh g^{-1} during the initial charging, which is almost the theoretical capacity, its first discharge capacity was only 108.07 mAh g^{-1}. The plateau near 4.0 V could be attributed to Mn^{3+}/Mn^{4+} redox reaction, whereas the others around 4.7 V are usually contributed by $Ni^{2+/3+/4+}$.[183,194] The amount of Mn^{3+} in the structure can be inferred by the capacity contribution from 3.80 V to 4.25 V, which was 10.65% during charging and 6.34% during discharging in this sample, indicating that more than half of Mn^{3+} oxidation is not reversible in the 1st cycle.[182,183]

The differential capacity curve (dQ/dV vs. E) can demonstrate clearer trends of the galvanostatic (dis)charge curve and is usually comparable with the cyclic voltammetry, Figure 5-5(b).

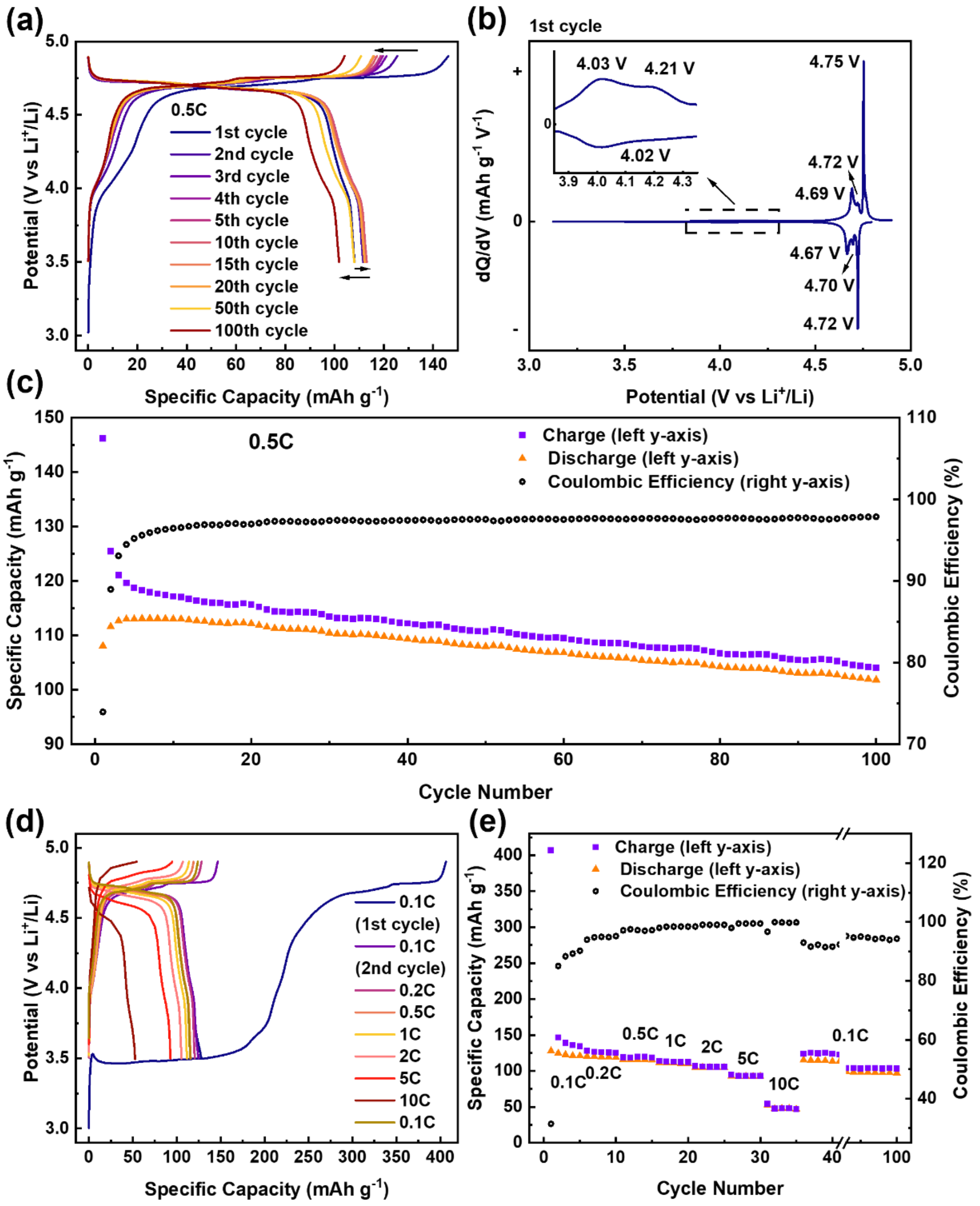

Figure 5-5. Cycling performance of LNMO-S. (a) Selected galvanostatic (dis)charging curves of LNMO-S at 0.5C and (b) its corresponding differential capacity curve for the 1st cycle. (c) Specific capacity and coulombic efficiency (CE) of LNMO-S cycled between 3.5 V to 4.9 V at 0.5C. Rate performance of LNMO-S, (dis)charge the cell at 0.1C, 0.2C, 0.5C, 1C, 2C, 5C, and 10C for 5 cycles each, then 0.1C for another 65 cycles. (d) Selected (dis)charge curves and (e) specific capacity and CE of each cycle.

The 4.0 V plateau shows two peaks during charging and one during discharging. The 4.7 V plateau split into three pairs of peaks, located at 4.69 V/4.67 V, 4.72 V/4.70 V, 4.75 V/4.72 V. The first two are attributed to Ni^{2+}/Ni^{3+} and the last is from Ni^{3+}/Ni^{4+}.[190] The separation of the two oxidation (or reduction) peaks in the dQ/dV curve caused by the two Ni redox couples around the 4.7 V region could reveal the ratio between the ordered and disordered phases, since the Li-ion insertion energies are different for the two. Shin et al. suggested that the smaller the separation, the higher the degree of the ordered structure.[195] LNMO-S demonstrates a 60 mV separation between the two Ni redox pairs, suggesting the disordered phase is dominating the structure.[181,183] This separation remained unchanged even after 100 cycles of (dis)charging at 0.5C, indicating good structural stability.

In the following cycles, Figure 5-5(a) and (c), the length of the 4.0 V plateau during charging decreases noticeably in the first four cycles and becomes stable after that. The overall charging capacity dropped slowly until 104.03 mAh g^{-1} in the 100th cycle. The discharge capacity increased from the 1st to the 8th cycle to 113.09 mAh g^{-1} and then decreased slowly to 101.81 mAh g^{-1} in the 100th cycle, which still retained 94.21% capacity of that in the initial cycle. The coulombic efficiency (CE) grows rapidly in the first eight cycles from 73.94% to 96.16%, followed by slight fluctuations between 96-98%.

As for the rate performance, Figure 5-5(d) and (e), the potential of the cell dropped slightly after it was first charged beyond 3.5 V at 0.1C, followed by a plateau around 3.5 V. After that, the 4.0 V and 4.7 V plateaus were observed. In the following cycles, with increased C-rate, the 4.0 V plateau stayed almost identical up to 2C and only decreased when charged faster than 5C. However, the length of the 4.7 V plateau kept reducing clearly, leading to reduced overall (dis)charging capacity. Though the (dis)charge capacity decreases with the growing C-rate, the coulombic efficiency increases. Returning to 0.1C after 10C, the charge and discharge capacities recovered to 123.89 mAh g^{-1} and 115.20 mAh g^{-1}, respectively, and maintained less than 18% capacity decay in subsequent cycles.

5-3.2.2 LNMO-T

LNMO-T demonstrates three plateaus during initial charging, Figure 5-6(a). The capacity caused by $Mn^{3+/4+}$ shows a plateau at around 4.0 V and accounts for 9.33% of the initial charging capacity, while that from $Ni^{2+/3+/4+}$ redox pairs show two plateaus around 4.7 V vs. Li^+/Li. During initial discharging, the capacity contributed by the Mn redox pair accounts for only 2.28% of the overall capacity, making the 4.0 V plateau almost unobservable, and it remains similar contributions in the following cycles.

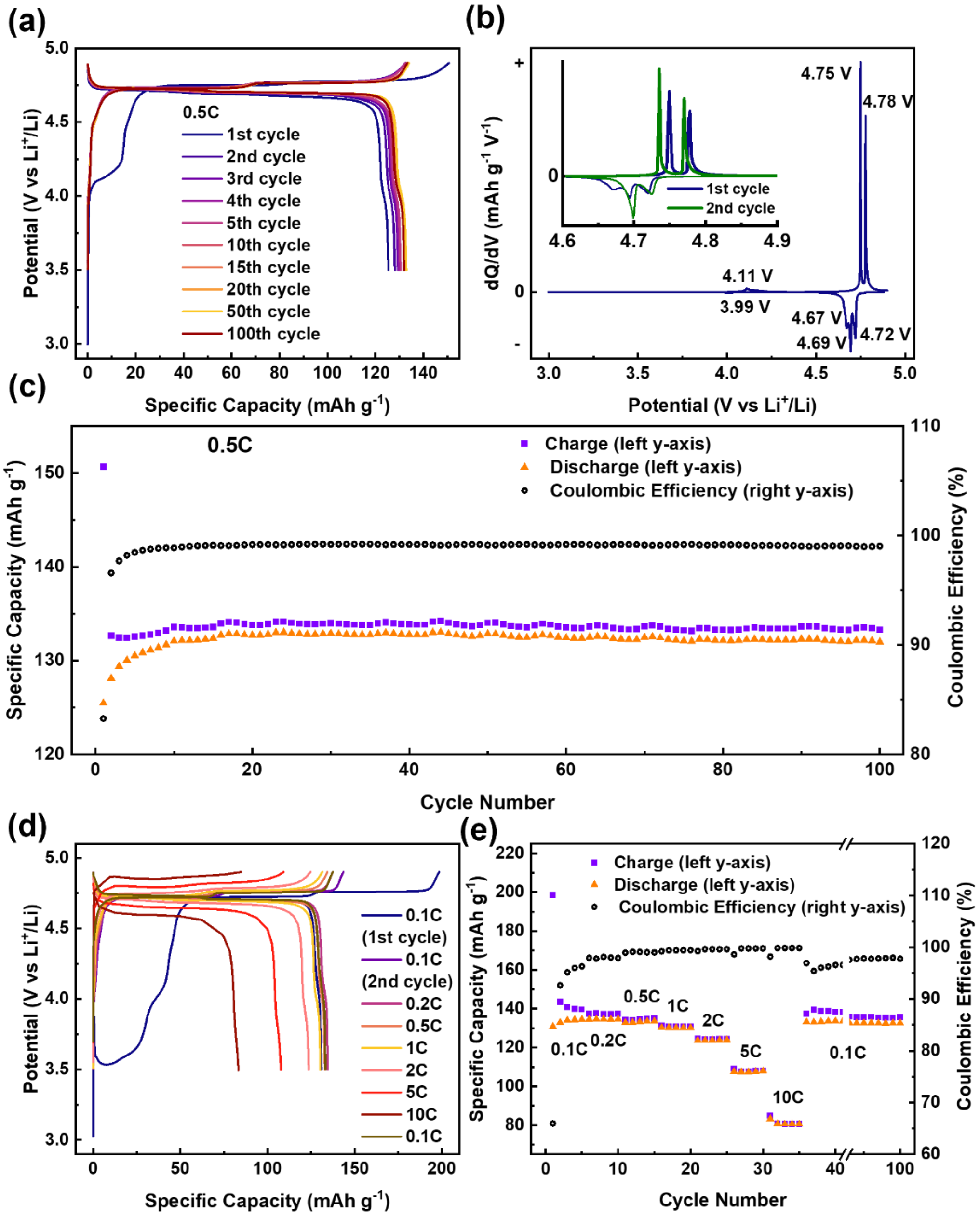

Figure 5-6. Cycling performance of LNMO-T. (a) Selected galvanostatic (dis)charging curves of LNMO-D at 0.5C and (b) the differential capacity curve for the 1st and part of the 2nd cycle. (c) Long-term cycling performance of LNMO-T cycled between 3.5 V to 4.9 V, 0.5C. Rate performance of LNMO-S, (dis)charge the cell at 0.1C, 0.2C, 0.5C, 1C, 2C, 5C, and 10C for 5 cycles each, then 0.1C for another 65 cycles. (d) Selected (dis)charge curves and (e) specific capacity and coulombic efficiency of each cycle.

In the dQ/dV curve, Figure 5-6(b), the 4.0 V plateau shows one peak at 4.11 V/3.99 V. The 4.7 V plateau was split into two oxidation peaks and three reduction peaks, all of which are very sharp. The separation between the two oxidation peaks is 30 mV, suggesting a high ratio of the ordered structure. In the 2nd cycle, the oxidation and reduction peaks near 4.7 V shifted toward each other, indicating an enhanced bulk electronic and ionic conductivity.[195]

In the long-term, Figure 5-6(a) and (c), the charging capacity dropped from 150.67 mAh g^{-1} in the 1st cycle to 132.64 mAh g^{-1} in the 2nd cycle, then slightly increased to 133.58 mAh g^{-1} until the 10th cycle and remained stable around that value. The discharging capacity grew slowly from 125.45 mAh g^{-1} in the 1st cycle to 132.09 mAh g^{-1} in the 10th cycle and showed very little variation after that. Therefore, the coulombic efficiency after the 10th cycle stayed within 99.0±0.2%.

When (dis)charging with different C-rates, LNMO-T shows a potential drop, followed by a plateau near 3.5 V after it was first charged above 3.8 V at 0.1C. Then, the 4.0 V and 4.7 V plateaus became observable again. With increasing C-rate, the length of the 4.7 V plateau gradually decreased, leading to reduced overall capacity. The capacity was restored after returning to 0.1C from fast (dis)charging.

5-3.2.3 LNMO-D

When cycled at 0.5C, Figure 5-7(a), three plateaus can be observed from the (dis)charging curves of LNMO-D. The $Mn^{3+/4+}$ plateau around 4.0 V is more pronounced than in the previous 2 samples and contributed to 12.33% and 10.82% of the initial charging and discharging capacity, respectively. This plateau results in the redox peaks at 4.06 V/3.94 V during the 1st cycle in the dQ/dV plot, Figure 5-7(b), and in the following cycles, the potential difference between them became smaller. The $Ni^{2+/3+/4+}$ contribution demonstrates plateaus near 4.7 V and leads to the redox peaks at 4.71 V/4.68 V and 4.77 V/ 4.72 V in the dQ/dV plot. The Ni redox peak position remained unchanged in the long term. The separation between the two Ni oxidation peaks is 60 mV, indicating a more pronounced disordered structure.

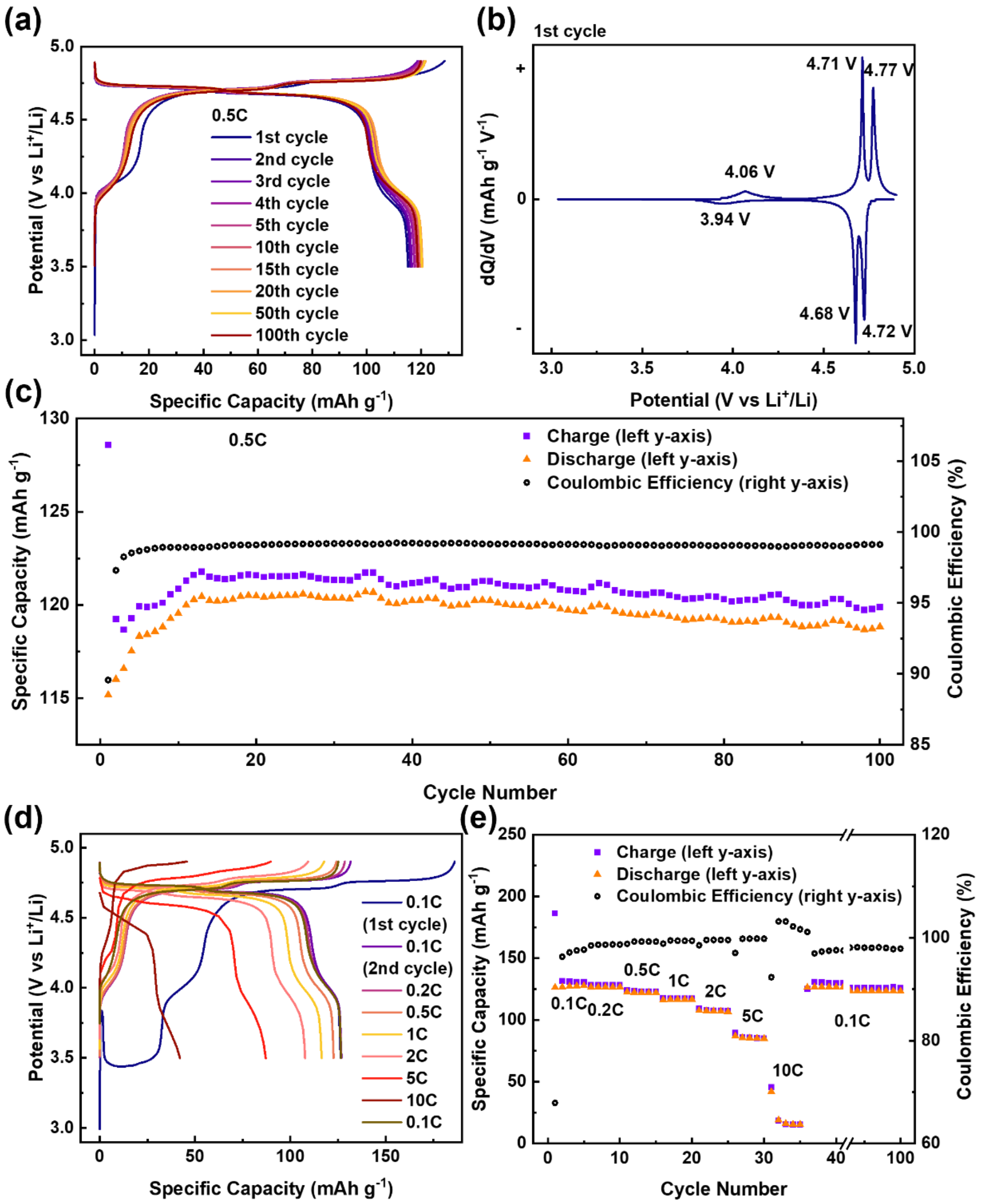

Figure 5-7. Cycling performance of LNMO-D: (a) Selected galvanostatic (dis)charging curves at 0.5C and (b) the differential capacity curve for the first cycle. (c) Long-term cycling performance of LNMO-D cycled between 3.5 V to 4.9 V, 0.5C. Rate performance of LNMO-D, (dis)charge the cell at 0.1C, 0.2C, 0.5C, 1C, 2C, 5C, and 10C for 5 cycles each, then 0.1C for another 65 cycles. (d) Selected (dis)charge curves and (e) specific capacity and coulombic efficiency of each cycle.

In the long-term, the charging capacity dropped from 128.59 mAh g^{-1} in the 1st cycle to a minimum value of 118.66 mAh g^{-1} in the 3rd cycle, then increased to 121.79 mAh g^{-1} in the

13th cycle and fluctuated close to this value afterwards. Meanwhile, the discharging capacity increased from 115.16 mAh g^{-1} in the 1st cycle to 120.45 mAh g^{-1} in the 13th cycle and then stayed around that value. The CE was kept within 99.0±0.2% from the 4th cycle.

The rate performance of LNMO-D is shown in Figure 5-7(c) and (d). A plateau around 3.5 V was observed after LNMO-D was first charged above 3.8 V at 0.1C, followed by the plateaus around 4.0 V and 4.7 V. The length of the 4.0 V plateau began to decrease when charged faster than 0.5C. Meanwhile, the 4.7 V plateau gradually decreased with a growing C-rate. The (dis)charge capacity was recovered after returning back to 0.1C from 10C and remained stable.

5-3.2.4 LNMO-Fe

When (dis)charged at 0.5 C, Figure 5-8(a), LNMO-Fe demonstrates one plateau at 4.0 V, contributed by Mn$^{3+/4+}$ redox couple, and two consecutive plateaus close to 4.7 V, contributed by Ni$^{2+/3+/4+}$ redox couples. The capacity attributed to Mn$^{3+/4+}$ reactions accounts for 16.27% of the initial charging capacity and 17.22% of the initial discharging capacity, and it shows a pair of peaks at 4.06 V/4.00 V in the dQ/dV plot, Figure 5-8(b). The redox reaction of Ni$^{2+/3+}$ and Ni$^{3+/4+}$ caused the peaks at 4.72 V/4.66 V and 4.77 V/4.73 V, respectively. The separation between the two Ni oxidation peaks is 50 mV, suggesting that the dominating phase is disordered. Both pairs of Ni peaks shifted toward each other in the 2nd cycle and remained in almost the same position after that, suggesting better bulk electronic and ionic conductivity from the 2nd cycle onward.

In the long-term, the charging capacity shows a similar trend to that of LNMO-D, dropping from 134.79 mAh g^{-1} in the 1st cycle to 126.74 mAh g^{-1} in the 4th cycle, then growing to 128.32 mAh g^{-1} in the 17th cycle, and then decreasing to 124.51 mAh g^{-1} with slight fluctuations. The discharge capacity increased by 4.38% from 121.89 mAh g^{-1} in the 1st cycle to the 17th cycle, and then followed a trend identical to that of the charging capacity. The CE shows a growing trend from 90.42% in the 1st cycle to the 7th cycle, then stayed within 99.1±0.1%.

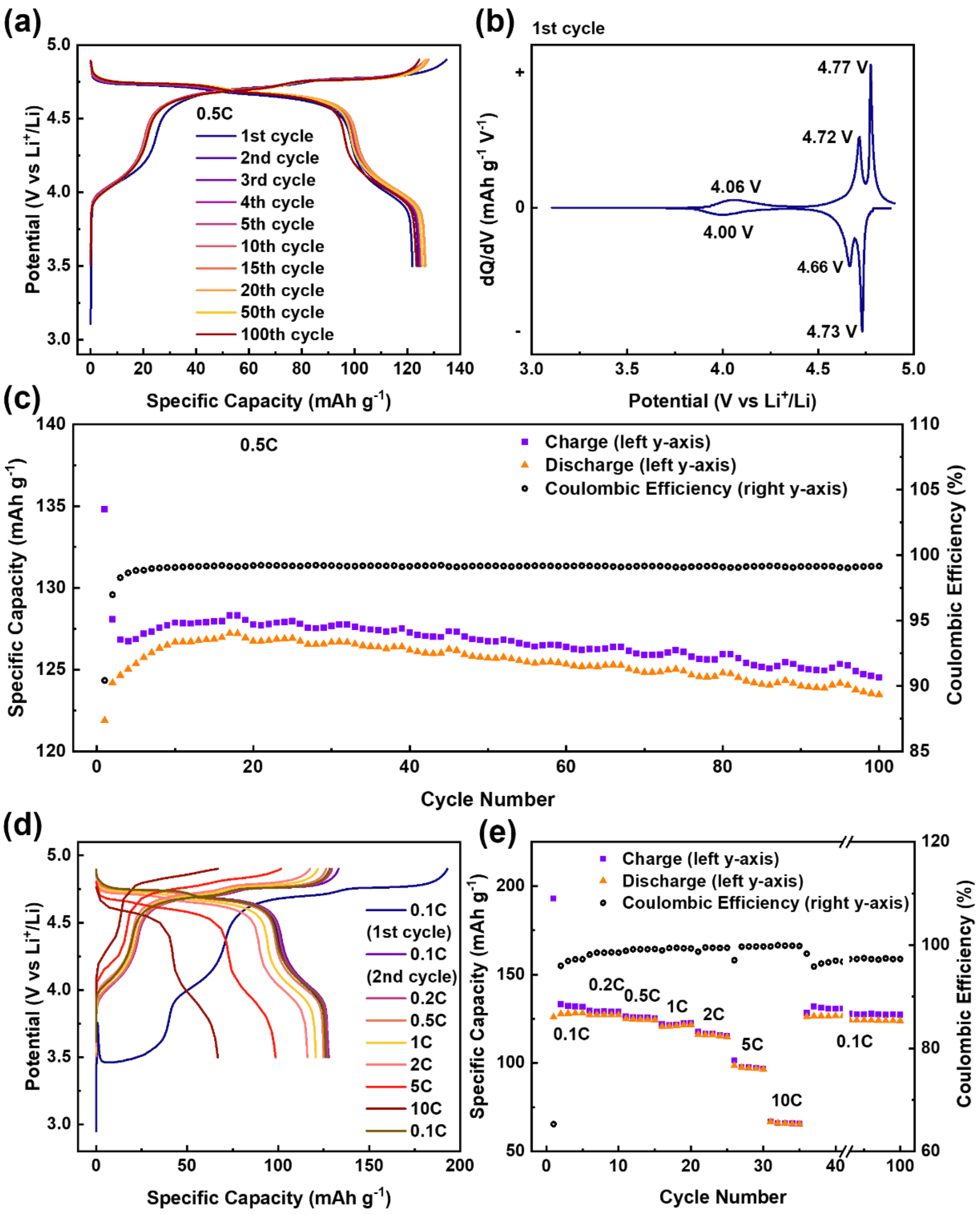

Figure 5-8. Cycling performance of LNMO-Fe. (a) Selected galvanostatic (dis)charging curves at 0.5C and (b) the differential capacity curve for the first cycle. (c) Long-term cycling performance of LNMO-Fe cycled between 3.5 V to 4.9 V, 0.5C. Rate performance of LNMO-Fe, (dis)charge the cell at 0.1C, 0.2C, 0.5C, 1C, 2C, 5C, and 10C for 5 cycles each, then 0.1C for another 65 cycles. (d) Selected (dis)charge curves and (e) specific capacity and coulombic efficiency.

When (dis)charged with changing C-rate, Figure 5-8(c), the potential of the sample dropped sharply after it was first charged above 3.7 V. After that, the plateaus near 3.5 V, 4.0 V, and 4.7 V are observed. The 4.0 V plateau remained unchanged when (dis)charged at 0.1C and 0.2C, but started to decrease when (dis)charged at 0.5C and faster. The 4.7 V plateau was gradually shortened by the increased C-rate. Both the discharge capacity and the CE returned to their initial levels when the rate was returned to 0.1C from 10C.

5-3.2.5 LNMO-Mg

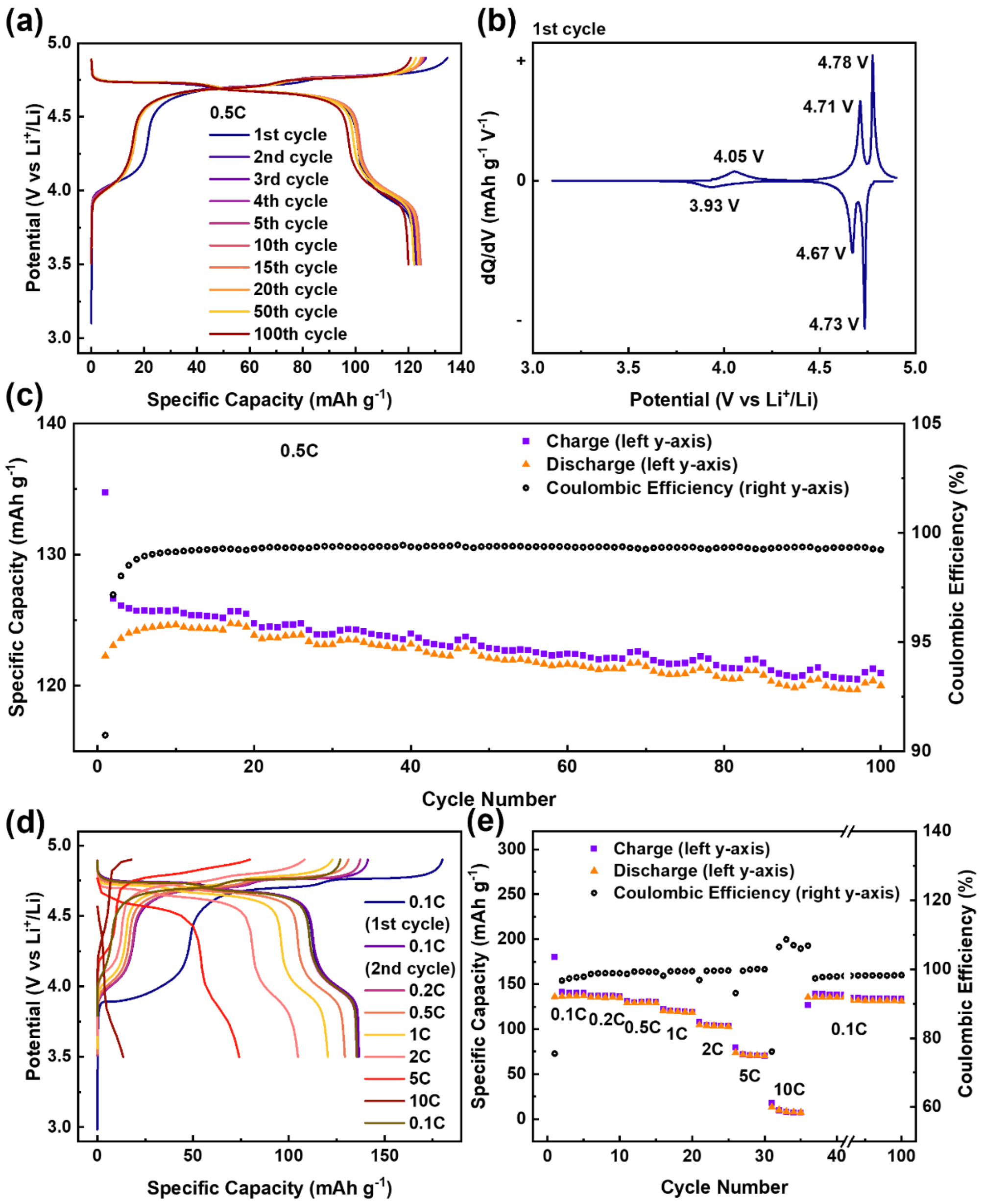

Figure 5-9. Cycling performance of LNMO-Mg. (a) Selected galvanostatic (dis)charging curves at 0.5C and (b) the dQ/dV curve for the 1st cycle. (c) Long-term cycling performance of LNMO-Mg cycled between 3.5 V to 4.9 V at 0.5C. Rate performance, (dis)charge the cell at 0.1C, 0.2C, 0.5C, 1C, 2C, 5C, and 10C for 5 cycles each, then 0.1C for another 65 cycles. (d) Selected (dis)charge curves and (e) specific capacity and CE.

LNMO-Mg behaves similarly with LNMO-D and LNMO-Fe when (dis)charged at 0.5C, Figure 5-9(a). The redox reaction of $Mn^{3+/4+}$ accounted for 15.11% and 15.84% of the initial charging and discharging capacity, respectively, and resulted in the 4.05 V/3.93 V peaks in the dQ/dV plot, Figure 5-9(b). This pair of peaks showed a smaller potential difference from the 2nd cycle onward. The 4.7 V plateau was from $Ni^{2+/3+/4+}$ redox species and contributed to the peaks at 4.71 V/4.67 V and 4.78 V/4.73 V in the dQ/dV curve. The dominating phase in LNMO-Mg is disordered as the separation of the two Ni oxidation peaks is 60 mV.

In the long-term, the charging capacity shows an overall decreased tendency, whereas the discharging capacity grew slightly from 122.27 mAh g^{-1} in the 1st cycle to 124.66 mAh g^{-1} in the 10th cycle, and then reduced with slight oscillation. Meanwhile, the CE increased from the 1st to the 20th cycle and remained at $99.4\pm0.1\%$ after that.

As for the rate performance, Figure 5-9(d) and (e), the LNMO-Mg did not show the 3.5 V plateau but only the 4.0 V and 4.7 V plateaus. The $Mn^{3+/4+}$ redox couple contributed more than 25% of the initial charging capacity but only up to 12.7% in the following cycles. The length of the 4.0 V plateau decreased only when (dis)charging faster than 0.5C, but that for the 4.7 V plateau was sensitive to the increasing C-rate. When returning back to 0.1C from 10C, both the discharge capacity and CE were recovered.

5-3.2.6 Comparison of the 5 samples

When cycled at 0.5C, all 5 samples show 4.0 V and 4.7 V plateaus that are attributed to $Mn^{3+/4+}$ and $Ni^{2+/3+/4+}$ redox reactions but with different ratios. The contribution of the former in the initial cycle decreases in the order of LNMO-Fe > LNMO-Mg > LNMO-D > LNMO-S > LNMO-T, meaning that the content of the Mn^{3+} also decreases in such order, which agrees with the XRD results. This suggests that the doping increased the content of Mn^{3+}.

From the dQ/dV plots, all 5 samples demonstrate one pair of redox peaks around 4.0 V, though the oxidation peak of LNMO-S split into two. Two pairs of redox peaks near 4.7 V were observed, though both the $Ni^{2+/3+}$ oxidation and reduction peaks of LNMO-S split into two and the reduction of Ni^{3+} in LNMO-T split. The peak separation of the two Ni oxidation reactions infers that the 5 samples have a decreasing degree of ordered structure in the order of LNMO-T > LNMO-Fe > LNMO-S = LNMO-D = LNMO-Mg.

After 100 cycles at 0.5C, the discharging capacity of the 5 samples shows retention above 94% in the order of LNMO-T > LNMO-D > LNMO-Fe > LNMO-Mg > LNMO-S from high to low.

When cycled at changing C-rate, except for LNMO-Mg, the other 4 samples demonstrate a potential drop after the initial charging and an extra plateau close to 3.5 V. All 5 samples show good structural stability since the capacity and CE can be restored when returning to 0.1C from 10C.

Overall, regardless of the C-rate, the initial charging and discharging always show noticeable irreversible capacity due to the formation of the CEI, which plays a critical role in the overall performance of the battery. [196] Therefore, *operando* Raman spectroscopy was employed to study the dynamic chemical environment change in the initial cycle.

5-3.3 *Operando* Raman spectroscopy

The Raman spectra were recorded throughout the initial (dis)charging cycle at 0.5C of all the 5 LNMO samples. The open circuit potential (OCP) was recorded for 4 minutes before and after the initial cycle of each sample. Each spectrum was accumulated 20 times of 5-second sampling and followed by a rest. Overall, the change of the interface was recorded every 118±1 s.

The Raman bands of the LNMOs before cycling as well as their assignments are discussed in session 3.1 and summarized in Table 5-3.

Table 5-3. Raman bands and their assignments of the LNMOs before cycling.

Raman shift (cm^{-1})	Assignment
162	Translation mode of lattice vibration
220 (200-235 wave)	Translation mode of lattice vibration
402 (360-430 wave)	Ni^{2+}-O (E$_g$)
494	Ni-O (F$_{2g}$)
523	Ni-O (F$_{2g}$)
591 (580-600 wave)	Mn^{4+}-O
609 (600-620 wave)	Ni^{2+}-O
634	Mn-O octahedra (A$_{1g}$)
664	Ni/Mn-O (F$_{2g}$)

5-3.3.1 LNMO-S

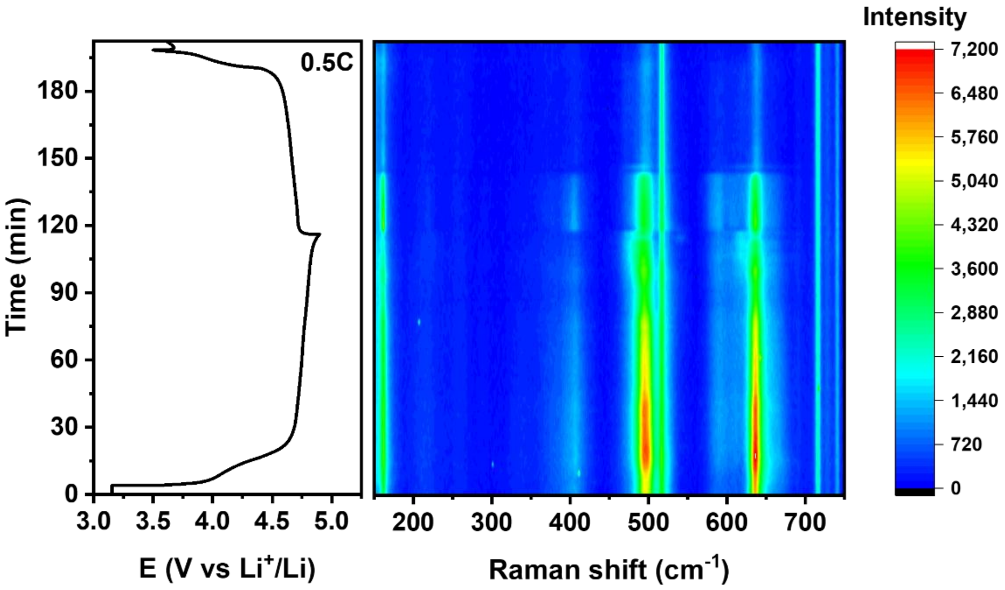

Figure 5-10. *Operando* Raman spectra of the first cycle of LNMO-S (dis)charged at 0.5C. (Dis)charge curve (left) and Raman spectra (right) are displayed.

As shown in Figure 5-10, during the OCP before charging, LNMO-S demonstrates peaks at 162, 220, 402, 494, 634 cm^{-1}, and their assignments are listed in Table 5-3. The 580-620 cm^{-1} wave was vaguely observed. Additionally, bands at 517, 716, and 742 cm^{-1} were detected, which we assigned to δ(O-C-O) in DMC solvent, δ(C=O) of the EC ring, and PF_6^-, respectively,[190] and they remained constant throughout the measurements.

The (dis)charging curve in the optical cell demonstrates identical features with that in coin cells, including the 4.0 V and 4.7 V plateaus, suggesting that the LNMO-S behaves identically in the two cell configurations.

During charging, all peaks first showed a growing trend until 4.629 V, at which time the peaks at 220, 402, 494, and 634 cm^{-1} reached their maximum values and the band around 664 cm^{-1} could be vaguely observed. This suggests that the LNMO-S has the highest crystallinity upon the end of Mn$^{3+/4+}$ oxidation and before Ni species oxidation. The 664 cm^{-1} band suggests the increase of the 16d sites Ni/Mn-O bonds from the disordered phase. Then, all peaks slightly decreased until 4.757 V, where LNMO-S just passed its Ni$^{3+/4+}$ oxidation peak in the dQ/dV plot, Figure 5-5(b). After that, all peaks remained similar in shape and intensity until 4.776 V, followed by all peaks continued to decline until 4.803 V and slightly rebounded until 4.816 V. Then, all peak intensities declined until 4.883 V with slight fluctuations.

As soon as the cell was charged above 4.846 V, a new peak at 538 cm^{-1} was detected and grew rapidly. It disappeared after the LNMO-S was scanned back to 4.754 V. In the meantime, the peaks at 162, 402, 494, and 634 cm^{-1} show an opposite changing trend to the 538 cm^{-1} peak, which is decreasing first followed by growth. This new peak can be assigned to the symmetric vibration of Ni^{4+}-O bonds from the fully delithiated $Ni_{0.5}Mn_{1.5}O_4$ phase. [190,197] No obvious peak was observed between the two at 497 cm^{-1} and 538 cm^{-1} that corresponds to Ni^{3+}-O stretching vibration,[181] indicating that the Ni in the spinel were mainly Ni^{2+} and Ni^{4+}.

When the cell was charged above 4.800 V, a peak at 619 cm^{-1} was developed from the 580-620 cm^{-1} wave and only went back to its initial state after the cell was discharged to below 4.754 V. Soon after this 619 cm^{-1} peak was detected, the 494 cm^{-1} peak became broader and was later recovered together with the 619 cm^{-1} band. Right after that, the 162 cm^{-1} band reached its maximum value again and the 590 cm^{-1} band evolved from the 580-620 cm^{-1} wave. As suggested by Zhu et al.,[198] we attribute the peaks at 619 cm^{-1} and 590 cm^{-1} to Ni^{2+}-O and Mn^{4+}-O, respectively, and their separation is only observable in the ordered phase. The more intense 162 cm^{-1} peak also suggests an increased F_{2g} vibration of the ordered phase. The broadening of the

494 cm^{-1} peak suggests the inhomogeneity of the Ni-O bond length, which could be caused by either the offset of Ni from the octahedra caused by Li extraction, or the increased structural strain. Its recovery indicates a better uniformity of the Ni-O bond length after slight lithiation.

All peaks were then showing a decreasing trend until the end of discharge. After the initial (dis)charge, only the peaks at 162, 494, and 634 cm^{-1} were still observable, and their intensities were reduced by 63%, 81% and 83%, respectively, suggesting the largely reduced overall crystallinity after the initial cycle.

5-3.3.2 LNMO-T

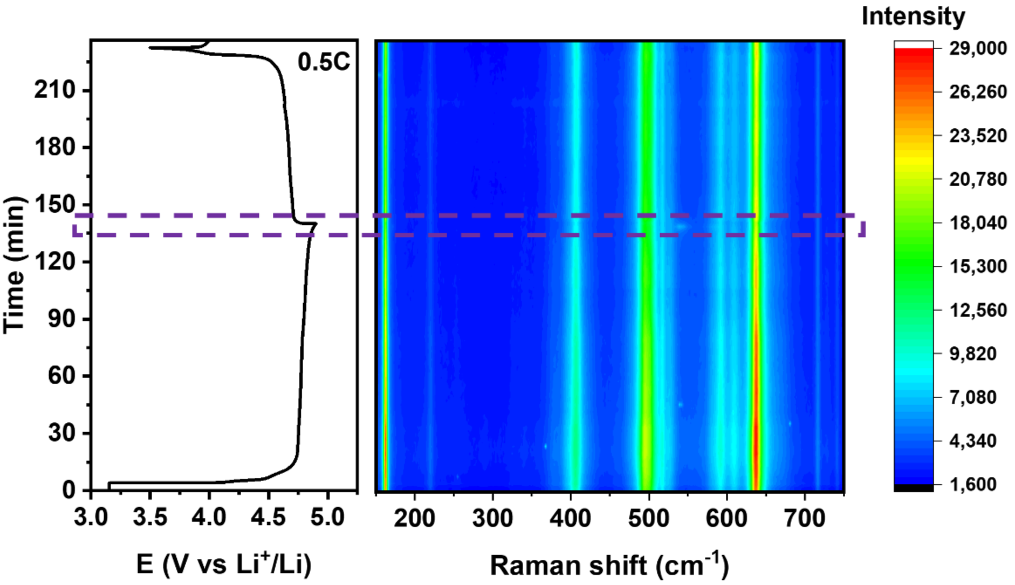

Figure 5-11. *Operando* Raman spectroscopy of the initial charging and discharging for LNMO-T at 0.5C. (Dis)charge curve (left) and Raman spectra (right). The purple rectangular highlights the peak from the newly formed bond.

The (dis)charging curve of LNMO-T in the optical cell has identical features to that in coin cells, Figure 5-11. During initial (dis)charging, the bands from LNMO-T at 162, 220, 402, 494, 523, 589, 606, and 634 cm^{-1} show only changes in their intensity, while the electrolyte peaks remained unchanged. All peaks demonstrate a slight increase trend once the charging began until 4.758 V, where the LNMO-T has just passed its $Ni^{2+/3+}$ oxidation peak in the dQ/dV curve, and show high intensities afterwards. When charged above 4.879 V, a new peak at 538 cm^{-1} is detected with 2-4% decreases of the peaks at 162, 494, and 634 cm^{-1}. This new peak can be assigned to the symmetric vibration of Ni^{4+}-O bonds from the fully delithiated $Ni_{0.5}Mn_{1.5}O_4$ phase. At such potential, most of the Ni in the structure has been oxidised to Ni^{4+} based on the dQ/dV curve, Figure 5-6(b), and this phase only lasts until LNMO-T was discharged below 4.712 V, which is the potential just before the Ni$^{3+/2+}$ reduction peak in the dQ/dV graph. After that, the original bands recovered to a slightly lower intensity compared to their initial stats and remained with small variations. Overall, the structure of the LNMO-T is very stable during its initial (dis)charge.

5-3.3.3 LNMO-D

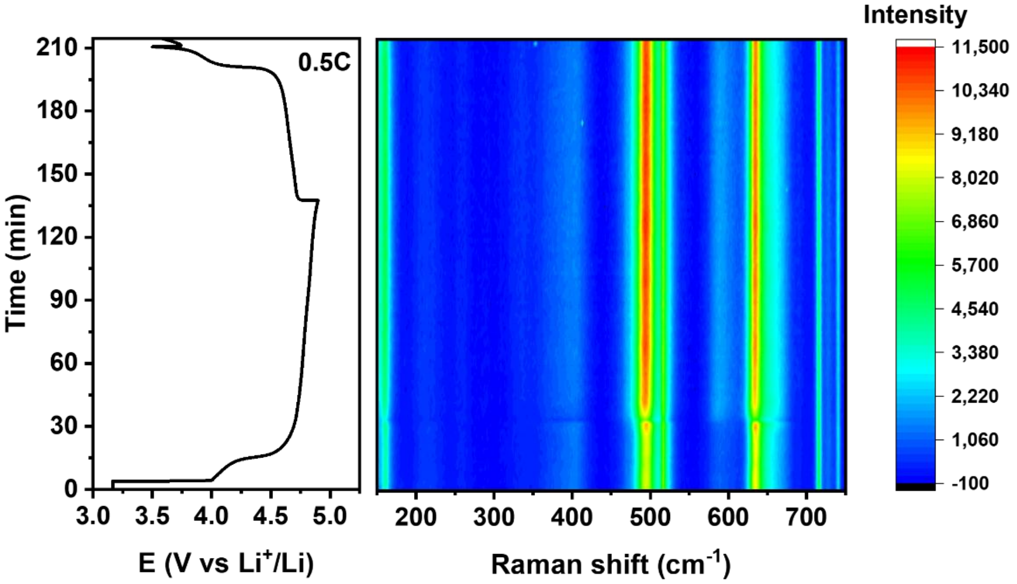

Figure 5-12. *Operando* Raman spectroscopy of the initial galvanostatic charging and discharging for LNMO-D at 0.5C. (Dis)charge curve (left) and Raman spectra (right).

During initial (dis)charging, LNMO-D showed peaks at 162, 220, 402, 494, 634, and 664 cm^{-1} from the spinel and peaks at 517, 716, and 742 cm^{-1} caused by the electrolyte, Figure 5-12. The signals from the spinel demonstrated a growing trend upon charging until 4.711 V, where the LNMO-D just passed its Ni$^{2+/3+}$ oxidation peak in the dQ/dV plot. Then, the intensity of all peaks slightly dropped, which is very likely due to a temporary instability of the laser. After that, the 664 cm^{-1} shoulder became more pronounced, and all other peaks quickly recovered and continued to grow to their highest values, followed by slight fluctuation since then. From charged above 4.732 V until the end of discharge, only changes in intensity of the peaks at 162, 494, and 634 cm^{-1} were found to have fluctuation in their intensity of no more than 15%, which suggests slight variations in the crystallinity of the spinel. No detectable changes were observed from other peaks. Overall, LNMO-D showed an increasing crystallinity during the oxidation of Mn$^{3+/4+}$ and increased concentration of the disordered phase during the oxidation of Ni$^{2+/3+}$, followed by good structural stability for the rest of the first cycle.

5-3.3.4 LNMO-Fe

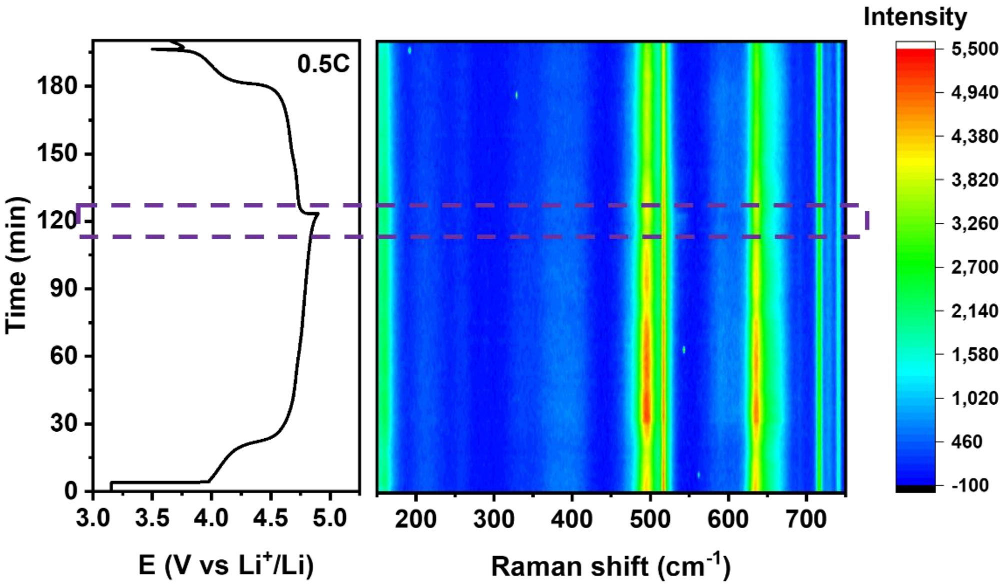

Figure 5-13. *Operando* Raman spectroscopy of the first galvanostatic (dis)charging and cycle for LNMO-Fe at 0.5C. (Dis)charge curve (left) and Raman spectra (right). The purple rectangular highlights the signal 531-550 cm^{-1} from the newly formed bond.

During OCP before charging, peaks at 162, 402, 494, 634, and 664 cm^{-1} were detected from the LNMO-Fe and the peaks at 517, 716, and 742 cm^{-1} were caused by the electrolyte, Figure 5-13.

The peaks from LNMO-Fe first showed a decreasing trend after charging started until 4.347 V, well past the $Mn^{3+/4+}$ oxidation peak in the dQ/dV curve, Figure 5-8(b). Then, the peaks experienced an increase in intensity until 4.699 V and maintained small fluctuations until 4.769 V. In the dQ/dV plot, this corresponds to the onset potential of $Ni^{2+/3+}$ oxidation until the peak potential of $Ni^{3+/4+}$ oxidation. Before growing again, all peaks dropped slightly and reached a local minimum at 4.792 V, where LNMO-Fe passed the $Ni^{3+/4+}$ oxidation peak in the dQ/dV curve. Between charged above 4.855 V and discharged until 4.782 V, a slight shoulder around 531-550 cm^{-1} was observed without noticeable sacrifice of the other peaks, which is very likely due to the Ni^{4+}-O bond formed due to the delithiation. After this shoulder recovered, all peaks dropped until discharged to 4.715 V, at which the $Ni^{4+/3+}$ reduction was completed. No obvious change in peak intensity was observed after that.

5-3.3.5 LNMO-Mg

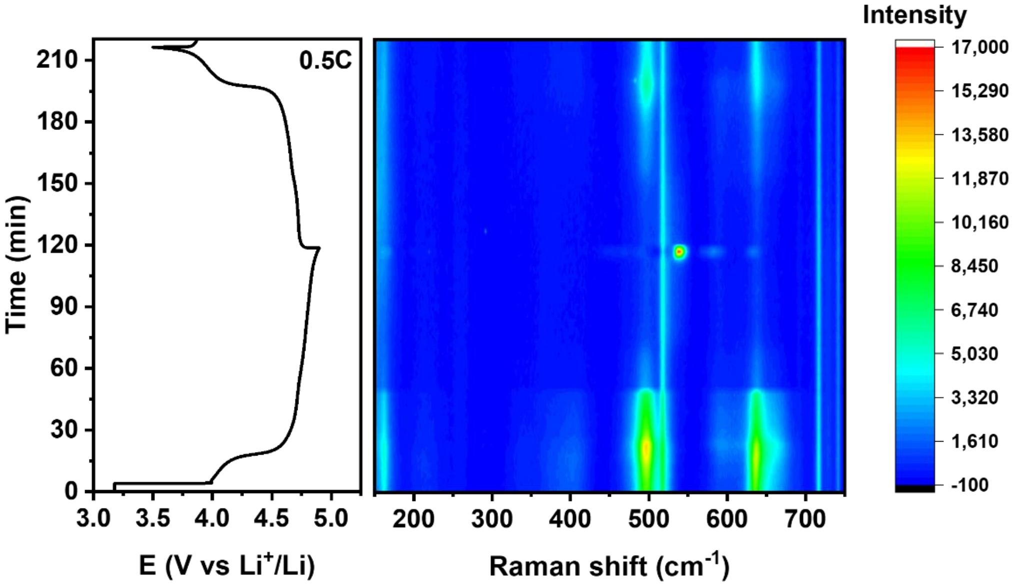

Figure 5-14. *Operando* Raman spectroscopy of the first galvanostatic (dis)charging and cycle for LNMO-Mg at 0.5C. (Dis)charge curve (left) and Raman spectra (right).

Before charging, LNMO-Mg shows peaks at 162, 402, 494, and 634 cm^{-1} and waves around 600 and 664 cm^{-1}, Figure 5-14. The electrolyte peaks at 517, 716, and 741 cm^{-1} were also detected.

Upon charging, the intensity of the peaks/waves at 162, 494, 600, 634, and 664 cm^{-1} grew smoothly and reached the maximum value when the cell was charged to between 4.226 and 4.598 V, at which point their intensities increased by 18%, 33%, 80%, 15%, and 54%, respectively. Then, all peaks from LNMO-Mg along with the 517cm^{-1} peak decreased gradually until 4.722 V, followed by a sharp drop until 4.730 V, suggesting reductions of crystallinity of the electrode and concentration of DMC close to the interface. According to the dQ/dV plot, Figure 5-9(b), most Ni^{2+} in the structure was oxidised to Ni^{3+} during this period. After that, while other peaks remained stable, the peak at 162 cm^{-1} became almost unobservable and the 494 and 634 cm^{-1} peaks kept decreasing until their intensity got down to 10% of their original intensity. In the meantime, the wave around 600 cm^{-1} evolved to a peak at 589 cm^{-1}.

Table 5-4. Summary of the Raman peaks from LNMO formed at high voltage.[181,190]

Raman shift (cm^{-1})	Assignment
164	Translation mode of lattice vibration (T_{2g})
459	Mn-O (E_g)
489	Mn-O (T_{2g})
538	Ni^{4+}-O (F_{2g})
583	Mn-O (A_{1g})
633	Mn-O (T_{2g})

From 4.777 V, a new peak at 538 cm^{-1} began to grow, followed by the evolution of peaks at 164, 459, 489, 538, 583, and 633 cm^{-1}, and their assignment is summarized in Table 5-4. These peaks showed maximum intensity between charged above 4.885 V and discharged back to 4.780 V, at which the 517 cm^{-1} peak also decreased by 13% compared with its intensity before the new electrode peaks formed, and recovered rapidly after discharge below 4.746 V.

As the discharge continued, the peaks/waves at 162, 220, 402, 494, 600, 634, and 664 cm^{-1} first underwent a reverse trend as observed during charging, and recovered to 74%, 47%, 40%, 63%, 46%, 66% of their original intensity when discharged to 4.177 V. Then, the 497 cm^{-1} peak and 600 cm^{-1} wave slightly decreased until the end of discharge.

5-4 Conclusion

The chemical composition, morphology, and crystal structure of the 5 LNMO samples were compared. The 3 pure LNMO samples demonstrated similar compositions, and the Fe and Mg dopants mainly replaced the Ni. The morphology of the 2 commercial samples was more regular, while the particle size of the 3 lab-synthesized samples was distributed widely. Though the XRD results were not able to suggest the structural differences between the 5 samples, their Raman spectra can suggest the relative ordered/disordered phase ratios.

Though the 5 samples showed different electrochemical behaviour because of their different Mn^{3+} concentration and ordered/disordered ratios, their long-term stability was good.

By using *operando* Raman spectroscopy, the dynamic chemical environment of the cathode-electrolyte interface of the 5 LNMO samples was revealed. All samples showed identical (dis)charging features with their behaviour in the coin cells, suggesting that the optical cell configuration and the Raman laser do not have noticeable impacts on the electrochemical performances of the LNMOs.

Compared with other samples, LNMO-D showed the least changes, that is, its Raman peaks demonstrated only intensity growth upon the charging until it slightly passed the $Ni^{2+/3+}$ oxidation and remained stable after that. No new band formation was observed during the entire initial charge and discharge. During the oxidation of Mn^{3+}, the crystallinity of all samples except for LNMO-Fe demonstrated growing trends. After that, when approaching the end of charging, signals around 538 cm^{-1} with different intensities were detected in addition to the original peaks for sample LNMO-S, LNMO-T, and LNMO-Fe, suggesting that part of the Ni on the surface exists as Ni^{4+}. It is worth noting that, all the original peaks of LNMO-Mg disappeared with the formation of a series of new bands when charged to above 4.777 V, meaning that its surface was completely converted into a fully delithiated $Ni_{0.5}Mn_{1.5}O_4$ phase, which was restored to the initial phase during the subsequent discharge process.

Overall, no obvious $Ni^{2+/3+/4+}$ conversion was observed during the corresponding current plateaus. The Ni^{4+}-O signal became observable only after the LNMOs were charged to above 4.77 V, that is, after most of the Ni in the crystals were oxidised. This may be because the lithium ions in the bulk continuously migrated to the surface, causing the Ni on the surface to be oxidised at last. During the subsequent discharge process, all samples were restored to their original peaks with different extents. No additional phase (i.e. CEI) was observed after the initial charging and discharging for all samples. *Operando* Raman spectroscopy experiments were successfully conducted to compare the phase transformation of the cathode and the electrolyte of 5 LNMOs during their initial cycle, where most CEI is believed to form in the literature. However, the assistance of other techniques (such as X-ray techniques) are required to link the relationship of the surface and the bulk behaviour.

Chapter 6. Dynamic stability of oxygen evolution reaction (OER) electrocatalysts

Parts of the results in this Chapter are published as:

Kutlusoy, T., Divanis, S., Pittkowski, R., Marina, R., Frandsen, A. M., Minhova-Macounova, K., Nebel, R., Zhao, D., Mertens, S. F. L., Hoster, H., Krtil, P., & Rossmeisl, J. (2022). Synergistic effect of p-type and n-type dopants in semiconductors for efficient electrocatalytic water splitting. *Chemical Science*, *13*(46), 13879–13892. DOI: 10.1039/D2SC04585K.

In this Chapter, the stability of several OER electrocatalysts during different electrochemical conditions was studied. We investigated both the substituted TiO_2 semiconductors for OER electrocatalysis in acidic media and La-based perovskites as OER electrocatalysts in alkaline electrolytes.

For the substituted TiO_2 sample, I conducted, processed, and analyzed the online ICP-OES measurements together with Dr Rebecca Pittkowski (University of Copenhagen, Denmark) for studying the dynamic stability of the electrocatalysts under different electrochemical (EC) conditions. The synthesis, computational work, as well as initial electrochemical characterization, were done by our collaborators at the University of Copenhagen, Denmark.

For the La-based perovskites samples, I performed, processed, and analyzed the online ICP-OES experiments to study the dynamic stability of the electrocatalysts under different EC conditions together with Dr Da Xing and Mr Leander Kucklick (University of Duisburg-Essen, Germany). The synthesis and initial electrochemical studies were done by our collaborators at the University of Duisburg-Essen, Germany.

6-1 Introduction

Large-scale development of renewable energy is crucial for the sustainability of various industries.[4] Replacing fossil energy with green energy represented by wind and solar energy can effectively reduce carbon emissions and the global climate problems it brings.[1–3] However, since these renewable energy forms can only be produced intermittently, it is difficult to meet the needs of human society, so other forms of energy and corresponding conversion or storage systems need to be developed.

Molecular hydrogen is one of the most promising candidates for green energy because its combustion products do not contain any carbon. So far, the main production method for molecular hydrogen is by steam reformation of natural gas or other fossil fuel, such as propane, diesel, etc., which can only generate low-purity hydrogen and such a process cannot help with the dependence on fossil fuel.[199–201] In such a context, electrocatalytic water splitting for hydrogen generation attracts attention.[13,16]

Electrocatalytic water splitting involves converting electricity into chemical energy by splitting the water into molecular hydrogen and molecular oxygen. This process can happen in both acidic and alkaline conditions but both are limited by the sluggish kinetics of the oxygen evolution reaction (OER).[202] Though efforts have been made to develop the electrocatalysts for OER, their reactivity and stability still require further improvement to be commercialized.

The conductivity of the electrolyte strongly affects the Ohmic losses caused by charge transportation in the electrolysis. Therefore, water electrolysis is often carried out under strong acid or strong alkaline conditions thanks to their excellent conductivity. The anodic OER process in acidic electrolytes can be described by Equation 6-1,

$$2H_2O \rightarrow 4H^+ + O_2 + 4e^- \qquad \text{Equation 6-1}$$

and the process in alkaline electrolyte by Equation 6-2.

$$4OH^- \rightarrow O_2 + 2H_2O + 4e^- \qquad \text{Equation 6-2}$$

No matter the working environment, ideal electrocatalysts should perform not only excellent activity but also good stability so that the whole electrolysis system can work long enough to meet the requirements of applications. In the meantime, the cost, or in other words the reserve on earth, is expected to be as low as possible.

6-1.1 In acidic electrolytes

In acidic conditions, the cathodic hydrogen generation tends to have a more facile kinetic barrier, together with higher current densities and voltage efficiencies.[61] However, further research is still needed to develop affordable electrocatalysts with good activity and stability.[60]

To date, only Ir and Ru-based oxides show good balances between activity and stability in acidic electrolytes,[58,203,204] while others tend to degrade rapidly. But the scarce reserves of Ir and Ru lead to high costs, which makes their scale-up unrealistic. Therefore, developing novel electrocatalysts with better stability at a reasonable cost that works in acidic media remains urgent.

Under acidic conditions, OER consists four coupled electron-proton transfer reactions, Equation 6-3 to Equation 6-6,

$$H_2O + * \rightarrow HO * + e^- + H^+ \qquad \text{Equation 6-3}$$

$$HO * \rightarrow O * + e^- + H^+ \qquad \text{Equation 6-4}$$

$$O * + H_2O \rightarrow HOO * + e^- + H^+ \qquad \text{Equation 6-5}$$

$$HOO * \rightarrow * + O_2 + e^- + H^+ \qquad \text{Equation 6-6}$$

where the asterisk (*) represents the active site at the surface of the electrocatalyst. In other words, the $HO*$, $O*$, and $HOO*$ are the intermediates absorbed on the active sites of the electrocatalysts.

Ideally, the free energy of adsorption of all these intermediates to the electrocatalyst surface should be that all the above processes happen at the equilibrium potential of 1.23 V in the described sequence and thus each step is driven by 1.23 eV. Therefore, the difference in the adsorption energy of the intermediate species HO* and HOO* should be 2.46 eV. However, one of the biggest challenges for most electrocatalysts is that these two species seem to have a similar binding way with the electrocatalyst surface, resulting in a constant adsorption energy difference of 3.2 eV and an unpreferred scaling relation between the two intermediates.[205–207] So far, to the best of our knowledge, very rare electrocatalysts can overcome this challenge to properly reduce the required overpotential while showing good stability and reasonable cost.

To eliminate the dependence of OER electrocatalysts on Ir- and Ru-based oxides, here, we propose to activate semiconducting materials, such as TiO_2, aiming for a better balance of activity and stability to be candidates for OER electrocatalysts. Semiconductors usually have inherent good stability due to their wide bandgap, which in turn results in low electrocatalytic activity as it requires high energy to be excited.[208,209] Our strategy relies on doping semiconductors to increase their OER activity and TiO_2 is chosen to be a model material,[209–214] section 6-3.1 , and our work was initiated through a series of computational works by our collaborator.

TiO_2 was doped by n-, p-type, and their combination dopants for their activation toward better OER electrocatalytic activity and is the first work to apply this strategy to electrocatalysis to the best of our knowledge.[215–217]

For semiconducting oxides, any computational approach needs to avoid finite-size effects leading to computational artefacts.[205] With the elimination of the artefacts caused by finite-size effects, the evaluation of the heavily doped semiconductor (i.e. TiO_2 in this chapter) electrocatalyst's activity and the determination of their position on the theoretical OER activity volcano diagram becomes possible through computational methods.[205,230,231]

The poor conductivity of semiconductors can be improved by n-type dopants, while the p-type dopants increase the possibility of the semiconductor to form a hole in the valence band. Figure 6-1 demonstrates the schematic diagram of the doped rutile TiO_2's structure, which was doped by n-type dopant (V), p-type dopants (Rh), and co-substituted (V&Rh), as well as their projected density of states (pDOS).

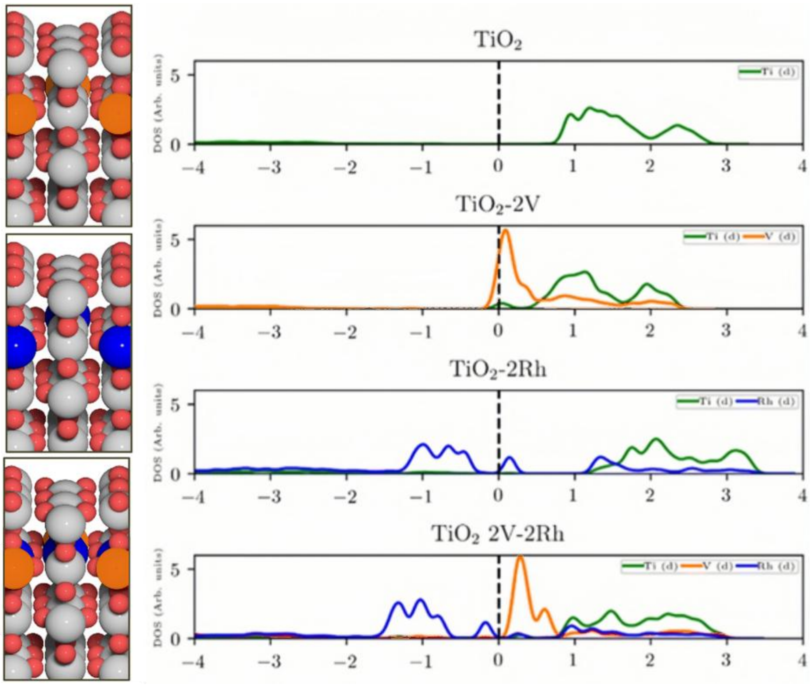

Figure 6-1. Left: schematic diagram of the atomic structures of the substituted TiO_2: the orange spheres represent V and the blue ones represent Rh. Right: the projected density of states (pDOS), from top to bottom: pristine TiO_2, V- substituted TiO_2, Rh- substituted TiO_2, and co-substituted TiO_2. The dashed line represents the Fermi level.

Both single-type dopants-substituted and co-substituted TiO_2 show new states in the bandgap, which may interact with water molecules thanks to their occupancy. In the case of the co-substituted TiO_2, a new narrow electronic band may be formed across the Fermi level, which enables their electronic structure similar to a conductor. In such a way, both the conductivity and the activity toward electrocatalysis of the semiconductor can be effectively improved.

The effect of the dopants and their position on the theoretical OER activity volcano diagram was assessed by density functional theory (DFT) calculation, Figure 6-2(a) and (b). Our results suggest that only co-substitution is beneficial for OER activity because n-type dopants cause accumulation of the strongly absorbed species, and blockage of the surface, while p-type dopants did not alter the reactivity in an obvious manner.

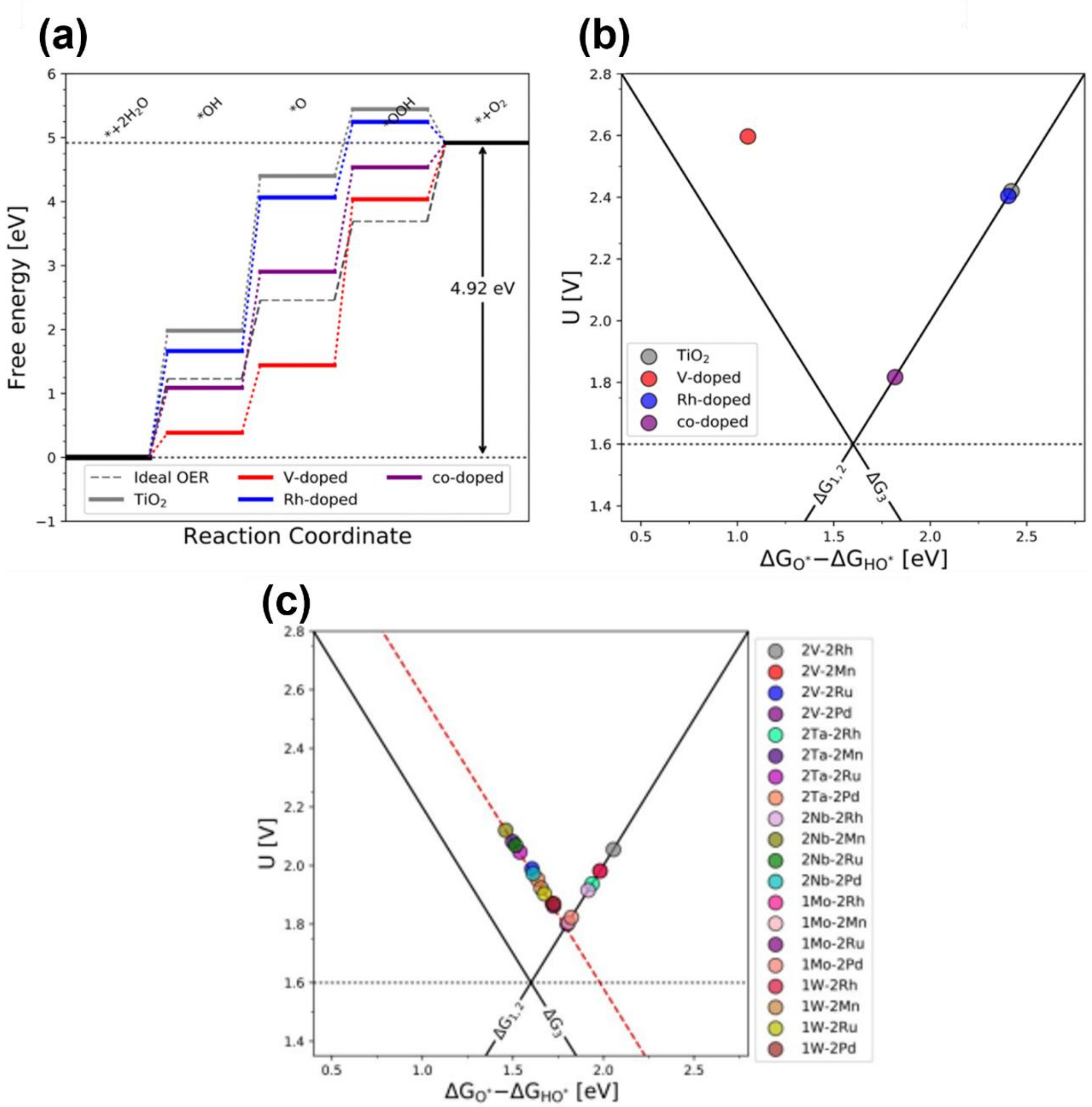

Figure 6-2. (a) Free energy diagram of pristine TiO_2, V-doped TiO_2 (n-type), Rh-doped TiO_2 (p-type), and co-doped TiO_2. (b) The OER activity volcano of the pure and doped TiO_2 shown in (a). (c) Co-substituted TiO_2 with different n- and p-type dopant pairs. The dashed line represents the energy interdependency of the HO* and HOO* intermediates.

Through a series of computational works, we broadened the concept of co-substitution to several elements, including V, Nb, Ta, Mo, and W as n-type dopants, and Rh, Mn, Pd, and Ru as p-type dopants. All the combinations showed increased OER activity compared with pristine TiO_2 as all the required overpotential of co-substituted TiO_2 is lower than that of the pristine TiO_2, Figure 6-2(b) and (c).

To validate the theoretical calculation results, experiments were then conducted. Single-substituted and co-substituted TiO_2 were synthesized by spray-freeze freeze-dry approach, and the substitution degree of all samples was 20% of cationic positions in either one dopant or two dopants in identical ratio.

The structure, which was analysed by XRD, of the as-synthesized samples conforms to that of the anatase TiO_2 polymorph, while their absorption in the visible region showed notable differences. The as-synthesized co-substituted samples demonstrated continuous absorption over relatively broad interval of energies in their UV-Vis spectrum, spanning from circa 2.0 to 2.25 eV, which is consistent with DFT calculations.

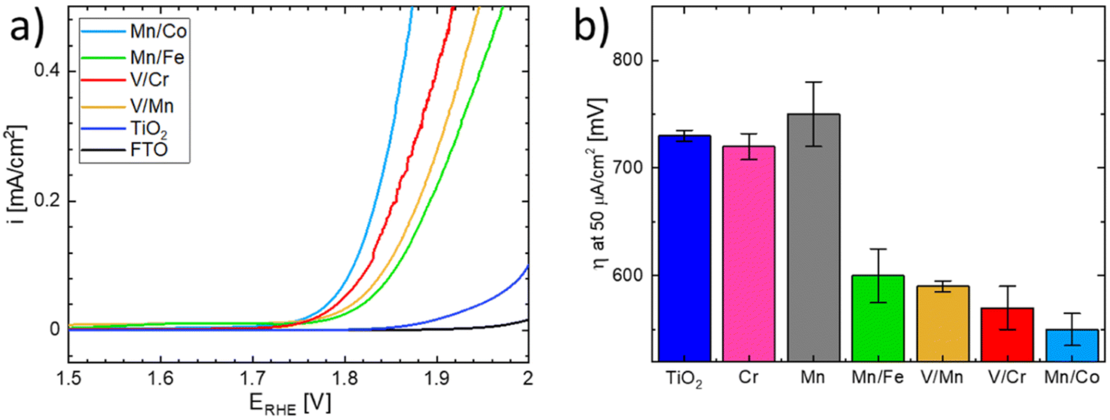

Figure 6-3. (a) Linear sweep voltammograms of pristine TiO_2 and substituted TiO_2 measured on an FTO current collector. Supporting electrolyte: 0.1 M $HClO_4$. Scan rate: 5 mV s^{-1}. (b) Comparison of the overpotential required to reach a current density of 50 μA cm^{-2} for single- and co-substituted TiO_2. The shown values are the mean of three individual measurements.

Through electrochemical characterizations in an acidic electrolyte, the OER activity of the samples was compared by their overpotential required to reach a current density of 50 μA cm^{-2}, Figure 6-3. The single-substituted samples showed almost no improvement in the OER activity compared with pristine TiO_2, while the activity of co-substituted samples was enhanced, as the overpotential decreased by up to 180 mV for Mn/Co doping. Among all samples, the Mn/Co co-substituted sample required the least overpotential.

6-1.2 In alkaline electrolytes

In alkaline electrolytes, the OER processes are shown in Equation 6-7 to Equation 6-10.

$$\mathrm{OH^- + * \rightarrow HO* + e^-} \qquad \text{Equation 6-7}$$

$$\mathrm{HO* + OH^- \rightarrow O* + H_2O + e^-} \qquad \text{Equation 6-8}$$

$$\mathrm{O* + OH^- \rightarrow HOO* + e^-} \qquad \text{Equation 6-9}$$

$$\mathrm{HOO* + OH^- \rightarrow * + O_2 + H_2O + e^-} \qquad \text{Equation 6-10}$$

Under alkaline conditions, several non-precious metals oxides, such as Ni-, Co-, Mn-, etc. containing oxides, show comparable stability, but their activity requires further development.[218,219]

Perovskite, which has advantages including diversified redox behaviour, good conductivity for both ions and electrons, excellent chemical stability, etc., is assumed to be a promising OER electrocatalyst as an alternative to those precious metal-based oxides.[222,223]

Perovskite has the general stoichiometry of ABO_3, Figure 6-4, where A-site cation represents larger cations such as alkaline-, alkaline earth-metal ions, etc., and B-site cation represents smaller cations such as transition metal ions. The larger A cation is usually the centre of the polyhedron consisting of twelve O anions, whereas the smaller B cation is located in the centre of the octahedron.[221,224,225] Since there are two types of cations in the structure, the electrocatalytic activity of perovskite is expected to be tuned easily by substitution, defect engineering, etc.[226,227] Lanthanum-based perovskite, which has the stoichiometry of $LaBO_3$, is particularly attractive due to its global abundance.[221,224,228] However, novel structural designs of those La-based perovskites for improved OER activity are still needed. In addition, their electrochemistry as well as dynamic stability under OER conditions requires in-depth study.

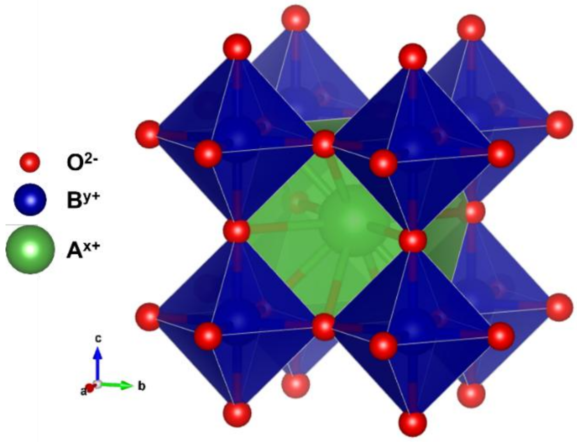

Figure 6-4. Schematic diagram of the perovskite structure.[220,221]

6-2 Materials and methods

The ICP-OES was an Agilent 5100 instrument, and the potentiostat was a BioLogic SP-300. All the water used in this Chapter was ultrapure water (MilliQ, Millipore, 18.2 MOhm cm, total organic carbon < 2 ppb). All the glassware was cleaned using boiling nitric acid 20% (diluted from >65% reagent grade, Sigma-Aldrich), which was then rinsed thoroughly with ultrapure water.

6-2.1 Substituted TiO_2 semiconductors for OER in acidic media

All samples were synthesized using a spray-freeze freeze-dry method by our collaborator from the University of Copenhagen, Denmark. The inks were made by adding 10 mg of the sample powder in a solution of 1 mL H_2O, 4 mL iPrOH, and 20 μL 5% Nafion 117 solution (Sigma Aldrich). The ink was shaken thoroughly and sonicated for better dispersion before drop-casting on the Ti foil. A 0.5×0.5 cm^2 Ti foil (0.25 mm thick, annealed, 99.5%, Alfa Aesar) was cut, followed by polishing with 1.0, 0.3 and 0.05 μm homogenised alumina suspension (Buehler) and a thorough rinse with MilliQ water before drying by N_2 blasting. The Ti was chosen thanks to its excellent stability within the potential window of interest in this study.[114] The ink was drop-cast by an air displacement pipette on the central 0.4×0.4 cm^2 area that was exposed in the flow cell, followed by drying by an infrared lamp. As the exposed Ti area is too small to take the desired amount of ink at once, the deposited layer was dried before the next increment and the final loading of the electrocatalyst was 100 μg cm^{-2}.

The ICP flow rate was 1.5 mL min^{-1}. Mn was monitored at 257.610 nm emission wavelength, V was 292.401 nm, Ti was 334.941 nm, and Co was 228.615 nm. Standard solutions for Mn, Ti, Co between 0 ppm (blank) and 1 ppm were prepared by diluting the 1000 ppm manganese ICP standard (Sigma-Aldrich) to 0.1, 0.2, 0.4, 0.6, 0.8, 1 ppm using 0.05 M H_2SO_4; While for V, the 1 ppm standard was diluted to 0.01, 0.02, 0.04, 0.06, 0.08, 0.1 ppm. The limit of detection (LoD) was estimated by multiplying the standard deviation of a blank solution across 10 measurements by 3.[89,165]

The 0.05 M H_2SO_4 solution prepared by dilution of concentrated sulfuric acid (Supelco, 96%) was used throughout the experiments in this section. A leak-free Ag/AgCl/3.4 M KCl electrode (Innovative Instruments) as RE and Pt coil as CE together with the samples coated on Ti to form a three electrodes setup in the flow cell. A polypropylene separator membrane (Celgard 3401) was used to enable the flow cell. The type 2 flow cell was used in this Chapter and its configurations and working principles are introduced in Chapter 2 and Chapter 3.

6-2.2 La-based perovskite for OER in alkaline electrolytes

$La_{0.8}Sr_{0.2}CoO_3$ (LSCO) and CoO inks were made by adding the sample powder in a solution of H_2O:EtOH=1:1 (w:w) with 5 wt% Nafion (Sigma Aldrich). After being mixed by a Vortex-Genie 2 mixer, the ink was then drop-cast onto the central 0.3×0.3 cm^2 area of a 0.5×0.5 cm^2

glassy carbon (GC), which was polished by 1.0, 0.3 and 0.05 μm homogenised alumina suspension, rinsed by ultrapure water, and dried by N_2 before. An infrared lamp was used to dry the drop-cast sample after each increment. In addition, both LSCO and CoO samples were also prepared by spray-coating by our collaborators from the University of Duisburg-Essen, Germany. The final loading of active material made from both methods was 1 mg cm^{-2}.

The electrolyte used throughout this section's experiments was a 1 M KOH solution prepared by diluting concentrated KOH (38%, VWR) with ultrapure water. The electrolyte was then purified through a column containing cation exchanger resin Chelex 100 (Sigma Aldrich) to remove Fe^{2+} ions, which has been observed in many studies to affect the OER activity even in trace amounts.[229]

The ICP flow rate was either 1.5 mL min^{-1} or 4 mL min^{-1}. La was monitored at 379.477 nm emission wavelength, Sr at 407.771 nm, Co at 228.615 nm, and Fe at 238.204 nm. Standard solutions for La, Sr, Co, and Fe between 0 ppm (blank) and 1 ppm were prepared by diluting the ICP standard (Sigma-Aldrich) to 0.1, 0.2, 0.4, 0.6, 0.8, 1 ppm using 1 M KOH. A leak-free Ag/AgCl/3.4 M KCl electrode (Innovative Instruments) or a reversible hydrogen electrode (RHE) was used as the RE and all the potential in the results were converted to RHE. An Au coil was used as the CE. The flow cell used was again the type 2 flow cell, and a polypropylene separator membrane (Celgard 3401) was used.

6-3 Results and discussion

6-3.1 Semiconductors with p-type and n-type dopants for efficient electrocatalytic water splitting in acidic electrolytes

The current in the electrochemical data usually involves not only OER but also the oxidation current of the containing elements and other side reactions. Thus, inferring the stability from only the electrochemical data is not reliable. By contrast, online ICP techniques can reveal the dissolution of the elements under different electrochemical conditions in real time, and can infer the stability of the electrocatalysts in a direct manner.[66,68,165,232–234]

Figure 6-5 shows the dissolution from Ti-Co-Mn oxide (TMCo) and Ti-Mn-V (TMV) during the open circuit potential (OCP), cyclic voltammetry (CV), and chronoamperometry (CA). The most intense dissolution for both TMCo and TMV appeared immediately after wetting by the electrolyte, Figure 6-5(a) and (d), which enriched the electrolyte close to the electrocatalyst surface with all the composition elements. After that, the dissolution of both decreases exponentially though TMV stabilized quicker, that is, the dissolution rate of TMV almost drops to around the detection limit after 200 s, whereas that of TMCo is still notable even after the whole 10-min OCP period. Notably, the Ti, which is generally considered stable in acidic media, dissolves from both.

Throughout the CV and CA measurements, Figure 6-5(b-c) and (e-f), Co from TMCo showed the highest dissolution rate. In TMV, Mn dissolution was the highest. For TMCo, Figure 6-5(b), the dissolution of Mn grew to a peak value when the potential was scanned to ca. 1.0 V, followed by dropping down to ca. 1 ng s^{-1} cm^{-2} for the rest of the first cycle. The peak dissolution rate for Co and Ti appeared just after the scan direction was revered from the positive vertex potential. In the 2nd cycle, all three elements showed a peak dissolution during the negative scan at around 1.8 V, and maintained stable for the rest of the cycle. In the 3rd cycle, the dissolution was reactivated during the negative scan at around 1.0 V and reached its maximum value when scanned back to 0.5 V. For TMV, Figure 6-5(e), no V dissolution was detected above the detection limit. The dissolution of Ti began at 0.8 V and grew to a plateau-like rate from 1.4 V to 2.0 V. While the dissolution of Mn started from 0.9 V and reached its maximum value at 2.0 V. In the following scans, the Mn dissolution showed an identical trend to that in its 1st cycle but a less intense signal, and Ti demonstrated a proportional signal with that of Mn.

In both samples, the dissolution peaks of different elements appear at different potentials during the 1st cycle, which may be an indication of the active sites of the electrocatalyst during OER, and the peaks appear at the same potential in the following cycles suggesting the transformed surface became more homogeneous. In addition, the dissolution of both samples under OER conditions is significantly less than their initial dissolution upon the contact with electrolyte.

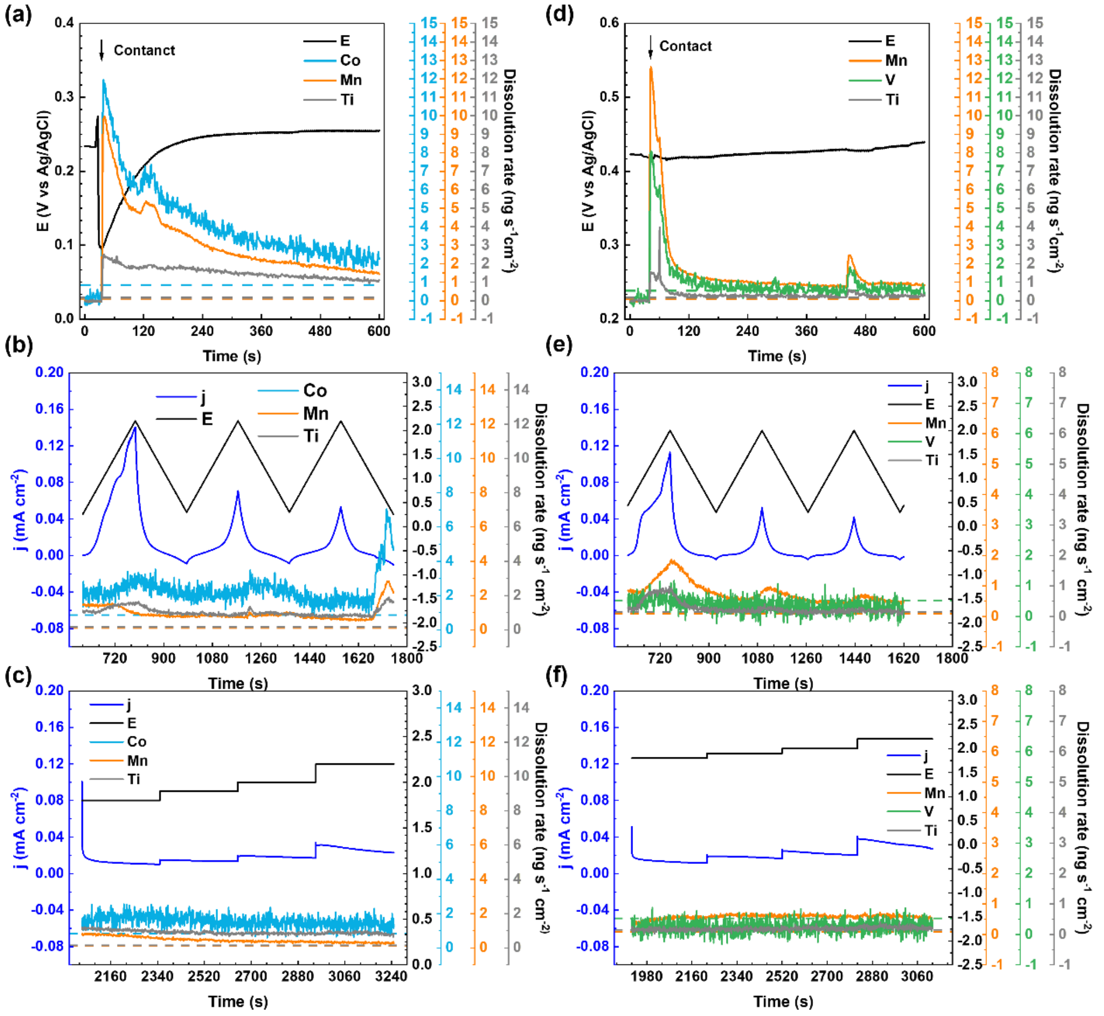

Figure 6-5. Real-time dissolution of the elements from (a-c) Ti-Co-Mn oxide (TMCo) and (d-f) Ti-Mn-V oxide (TMV) during a 10-min open circuit potential (OCP) followed by cyclic voltammetry (CV) and chronoamperometry (CA) (OCP was also measured in between CV and CA). Electrolyte: 0.05 M H_2SO_4. Scan rate for CV: 10 mV s^{-1}.

In the following CA measurements, Figure 6-5(c) and (f), the Mn dissolution rate decreased to lower than Ti in TMCo, though both showed decreasing trends even with increased potential. In TMV, only the dissolution Mn was kept slightly above the detection limit.

Though Ti oxides are known to have excellent chemical stability in acidic media, the dissolution of Ti was observed in our results.[235] The observed behaviour in the dissolution data, when the same dissolution rate for the transition metals (i.e. Co and Mn) as for the Ti, suggests that the conditions of the OER process is very likely promote the dissolute of Ti from the substituted TiO_2. If that is the case, the destabilization of Ti indicates that the co-substitution approach indeed activated Ti as a binding site for the intermediates during the OER process. One of the possible origins of Ti dissolution is the phase transformation of TiO_2 under different potentials as the stability of different phases of TiO_2 is found to be dependent on both pH and surface charge.[236] However, further study is required to distinguish the source and mechanism of the dissolved Ti species as Ti as substrate is also possible to dissolve.[237]

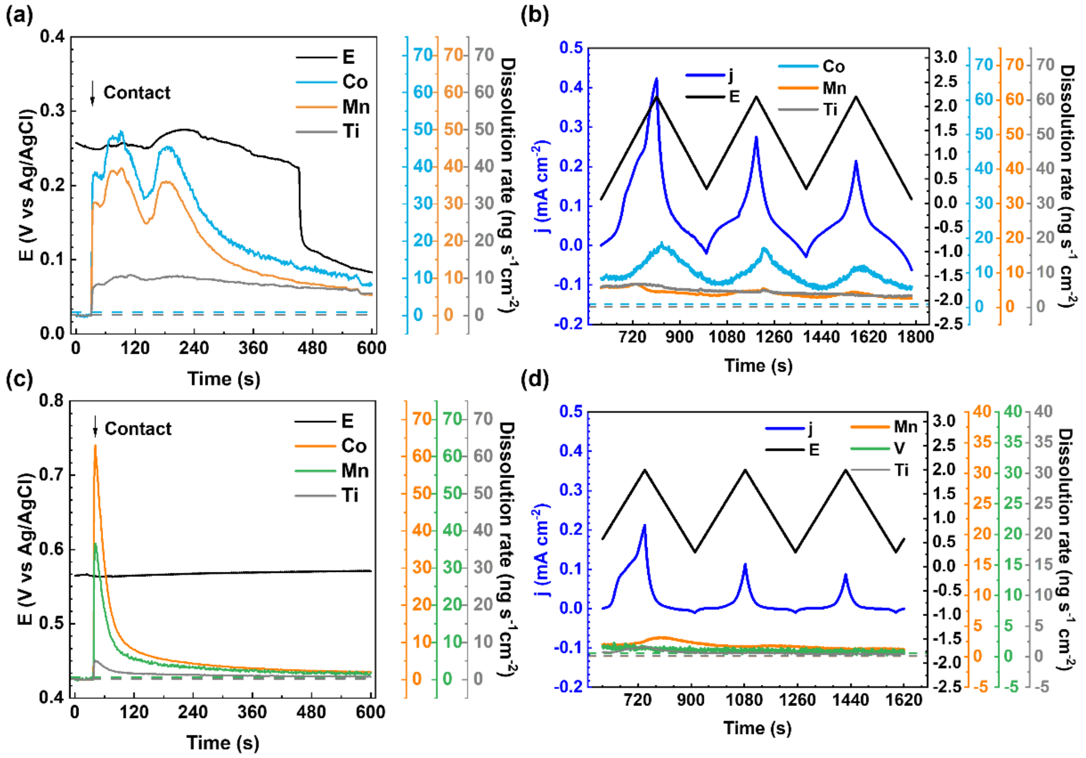

Figure 6-6. Real-time dissolution data of TMCo and TMV sample that are ca. 5 times thicker.

To further understand the stability of TMCo and TMV, a sample with ca. 5 times loading (thus thicker) for each was prepared and measured under identical conditions, Figure 6-6. Similar to what was observed in Figure 6-5, the potential of both fluctuated upon contact with the electrolyte, though TMV stabilized much quicker. The maximum dissolution rate of TMCo shifted to a minute after wetting, followed by another dissolution peak, Figure 6-6(a). For TMV, the maximum dissolution rate appeared at the initial wetting again, Figure 6-6(c). As shown in Figure 6-6(b) and (d), the dissolution rate of the samples with higher loading generally showed a similar trend to that in smaller loading samples, including the staggered peak during the initial cycle, and the amounts of elements dissolved were about 5 times, suggesting that the thicker film deposited was still within the 'thin film' regime and thus all the particles are contributed to the electrochemistry (and thus OER).[131]

6-3.2 $La_{0.8}Sr_{0.2}CoO$ (LSCO) and CoO as oxygen evolution electrocatalysts in alkaline solutions

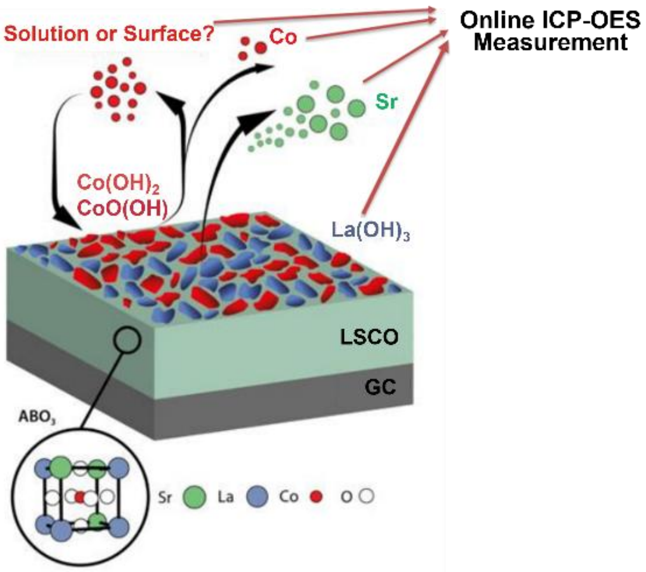

Figure 6-7. Schematic diagram of the dynamic surface change of LSCO.

Previously, our collaborator, the Hoster group from the University of Duisburg Essen (Germany), has studied the electrochemical properties of $La_{0.8}Sr_{0.2}CoO$ (LSCO) and CoO extensively. They investigated the OER activity of LSCO and CoO by rotating disc electrode (RDE) measurements at different scan rates (0.1-50 mV s^{-1}) and their results showed that LSCO has higher OER activity at slower scan rates (0.1-1 mV s^{-1}), while at faster scan rates (80-500 mV s^{-1}) the activity of CoO is better. In addition, LSCO showed increased activity during both chronoamperometry (CA) and chronopotentiometry (CP) measurements, suggesting a 'self-activated' property. However, the detailed process and mechanism of this 'self-activation' remain unclear. Therefore, the online ICP-OES measurements were employed to understand this phenomenon, Figure 6-7.

The dissolution of elements from LSCO under OER condition was measured during CV, Figure 6-8. In order to reach a current density of 10 mA cm^{-2}, 1.60 V vs RHE was needed. The overpotential needed during the online ICP-OES measurement agreed with that measured in other electrochemical measurements. Co was stable throughout the CV. La showed a ca. 30 ng s^{-1} cm^{-2} dissolution peak at the positive vertex potential. Non-zero Sr dissolution was detected throughout the CV, which increased from 1.68 V, reached its maximum value at the positive vertex potential, and only dropped back to around the detection limit when scanned back to below 1.5 V. The total Sr dissolved during the 1s cycle correspond to 0.6% of the total Sr from the sample.

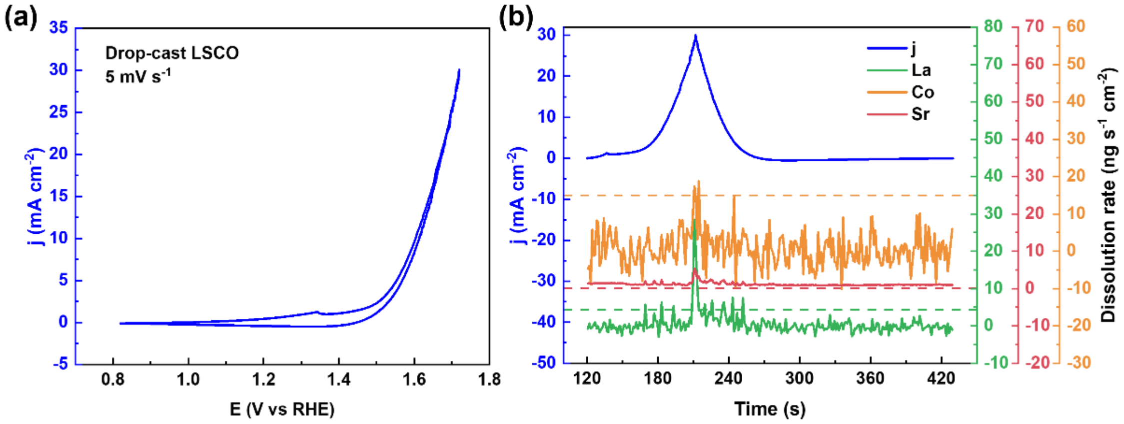

Figure 6-8. Real-time dissolution of the drop-cast LSCO on GC substrate during CV. Supporting electrolyte: purified 1 M KOH. Scan rate: 5 mV s^{-1}.

During the CA measurement, Figure 6-9, no Co dissolution was found to grow above the detection limit. La maintained stable as long as the potential was not higher than 1.4 V and only showed a slight increase when the potential was held at 1.5 V, which dropped back below the detection limit soon. For Sr, the dissolution increased immediately after the potential was held at 0.9 V, followed by a decreasing trend even when the potential was higher.

Figure 6-10(a) and (b) compares the stability of drop-cast and spray-coated LSCO. The drop-cast LSCO demonstrated lower overpotential but its potential took longer to stabilize, indicating a more homogeneous surface from the spray-coated sample. Co and La dissolution were not detected for both samples. Sr from the drop-cast sample dissolved at a much higher rate than that from the spray-coated sample.

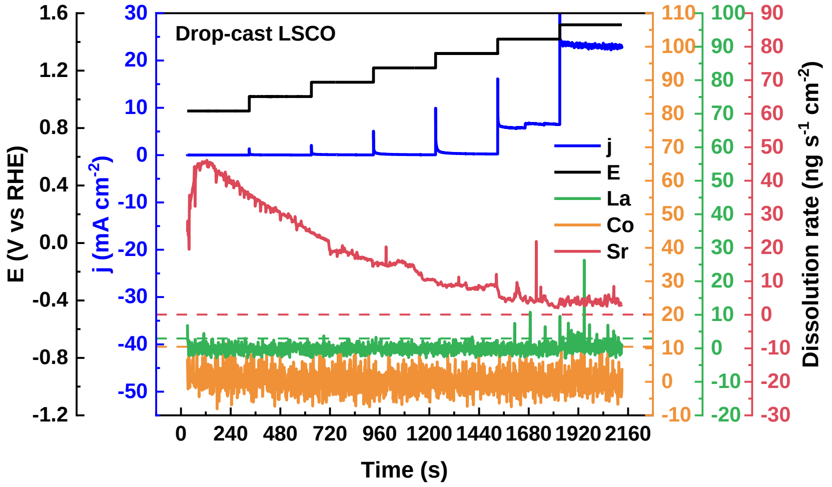

Figure 6-9. Real-time dissolution of the drop-cast LSCO during chronoamperometry measurements.

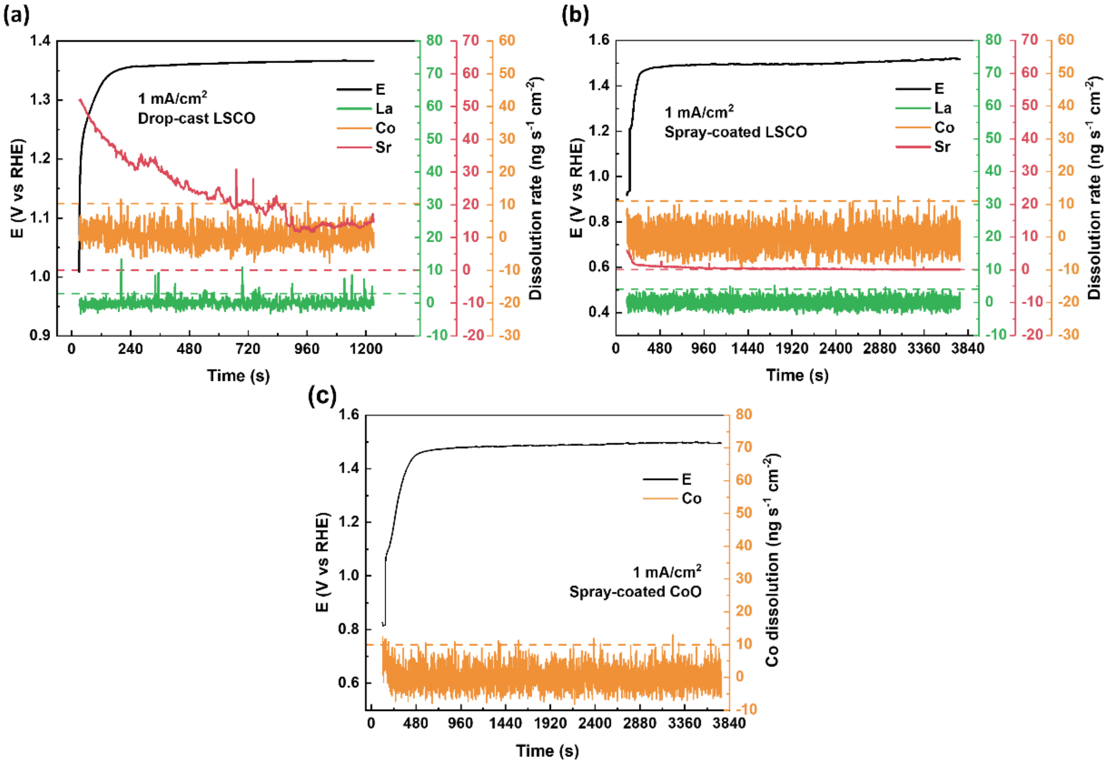

Figure 6-10. Real-time dissolution of (a) drop-cast LSCO, (b) spray-coated LSCO, and (c) spray-coated CoO during galvanostatic measurements. A constant current of 1 mA cm^{-2} was held for the three measurements.

As shown in Figure 6-10(b) and (c), CoO has a lower overpotential compared with LSCO, which agrees well with other electrochemical characterization. In addition, throughout the CP measurement, no Co dissolution above the detection limit was found except at the beginning, indicating that CoO can stabilize itself rapidly after wetting.

6-4 Conclusion

The co-substitution of wide bandgap semiconductors with both n- and p-type dopants affects both the electronic structure as well as the catalytic behaviour of semiconducting oxides. The OER electrocatalytic activity of the TiO_2 is increased by such a strategy. The experimental data of the co-substituted TiO_2 agreed well with the theoretical results. Good stability of the co-substituted TiO_2 samples under OER conditions were proved by online ICP-OES measurements.

The metal dissolution and stability of LSCO and CoO under OER conditions in an alkaline electrolyte were revealed and compared by online ICP-OES measurements. While Sr leached to the electrolyte in the most serious manner, La was only found to dissolve at high potential and Co showed relatively good stabilities.

Chapter 7. Conclusion and outlook

In this thesis, we studied extensively the interfacial degradation processes in electrochemical energy storage and conversion with a specific focus on LIB and water electrolysis.

We first established the online ICP-OES system starting from flow cell design and optimization, coupling the flow cell with ICP-OES, signals alignment, and system validation. We then used this technique for real-time electrolyte analysis of Mn dissolution from spinel LMO. Spinel, represented by LMO is a promising type of LIB cathode due to its structural stability and 3D Li^+ channels, low cost, and environmental friendliness, but its wider application is limited by premature ageing. One of the side reactions causing serious ageing is the transition metal dissolution (in this material, that is, Mn dissolution), which is well-known but poorly understood. We investigated the Mn dissolution from LMO during potentiostatic and galvanostatic cycling in electrolytes with varying pH values, and found that the widely accepted dissolution mechanism, Hunter's mechanism, is not able to explain the dissolution behaviour on its own. Besides, our data shows that the dissolution can be mitigated without coating, additives, etc. but by only potential conditioning.

Then, we used RRDE for real-time speciation of the dissolved Mn from LMO. ICP-OES can provide excellent detection limits for multiple elements but does not have access to the oxidation state of the dissolving species, which is essential for understanding the dissolution mechanism and subsequent mitigation strategy. There are increasing numbers of debates focusing on whether Mn^{2+} or Mn^{3+} is the dissolving species from Mn-containing cathode in recent years. Thus, we investigated the redox behaviour of the two species in depth. While Mn^{2+} can be easily prepared directly, Mn^{3+} is thermodynamically unstable and can be chemically transformed into other Mn species quickly. We therefore locally generated Mn^{3+} by oxidising Mn^{2+} on the disc of a RRDE and investigated its redox behaviour on the ring. We combined voltammetry, Levich and Koutechy-Levich analysis, Cottrell analysis, EIS, and Raman spectroscopy to understand the oxidation pathway of Mn^{2+}. Then, based on our understanding of the redox property of different Mn species on the Pt ring electrode, we quantitatively detect and speciate the dissolved Mn from LMO by combining RRDE and online ICP-OES. We found that both Mn^{2+} and Mn^{3+} are dissolving but at different potential/state of charge regions. Moreover, we also proposed a detailed mechanism of Mn dissolution.

One of the strategies to mitigate Mn dissolution suggested by many literatures is to replace 1/4 of Mn in the spinel with Ni, which then forms LNMO. However, the wider application of LNMO is still limited by its premature ageing, including the decomposition of electrolytes, the dissolution of transition metals, and their subsequent influences on the electrode-electrolyte interfaces for both cathode and anode. We investigated the chemical composition, morphology, crystal structure, and electrochemical properties of 2 commercial and 3 lab-synthesized LNMO. Moreover, the dynamic phase transformation of the CEI was observed by *operando* Raman spectroscopy. We found that some samples can be fully delithiated and form a new phase and some cannot. Our results suggested that *operando* Raman spectroscopy is an effective technique for interface study during electrochemical measurements.

Water electrolysis is one of the most promising methods of green hydrogen generation but is limited by the lack of efficient OER electrocatalysts. Ideal electrocatalysts are expected to show excellent activity and stability while having reasonable costs. We investigated the active material dissolution of several OER electrocatalysts during varying electrochemical conditions, which then provided clues for inferring their dynamic active sites and long-term.

Overall, we established and optimized several techniques for studying the interfaces of LIB and OER electrocatalysts. Our methodologies also have good capabilities with similar materials and systems. Our results contribute to a more comprehensive understanding of the degradation process and mechanism in the electrochemical energy storage and conversion systems, and hint at strategies for prolonging their lifetimes.

As an outlook, for the LMO study, combining our results with other real-time/*in situ*/*operando* techniques to study the bulk behaviour is expected to provide a deeper understanding of spinel

LMO, which is essential for further enhancing the performance of this type of material in LIB. Our techniques for dissolution detection and speciation are promising to be applied to other transition metals (Ni, Co, etc.), and for screening materials under environments with different key parameters including potential window, temperature, etc. In addition, the dissolved transition metal ions are widely believed to affect anode stability, and it would be interesting to investigate the anode surface under electrochemical conditions. For the LNMO study, we were limited to focus on the cathode surface transformation because of the technique chosen and time constraints, other surface- and bulk-sensitive techniques (such as synchrotron) and longer-term experiments are expected to help with a more comprehensive understanding. For the water electrolysis systems, larger-scale experiments would be valuable under conditions closer to industrial reality.

References

1. Höök, M. & Tang, X. Depletion of fossil fuels and anthropogenic climate change—A review. *Energy Policy* **52**, 797–809 (2013).
2. Lelieveld, J. *et al.* Effects of fossil fuel and total anthropogenic emission removal on public health and climate. *Proceedings of the National Academy of Sciences* **116**, 7192–7197 (2019).
3. Mac Dowell, N., Fennell, P. S., Shah, N. & Maitland, G. C. The role of CO2 capture and utilization in mitigating climate change. *Nature Climate Change* **7**, 243–249 (2017).
4. International Energy Agency. Global Energy Crisis. *https://www.iea.org/topics/global-energy-crisis* https://www.iea.org/topics/global-energy-crisis (2022).
5. Inumaru, J. *et al.* Fossil fuels combustion and environmental issues. in *Advances in Power Boilers* 1–56 (Elsevier, 2021).
6. Mitali, J., Dhinakaran, S. & Mohamad, A. A. Energy storage systems: a review. *Energy Storage and Saving* **1**, 166–216 (2022).
7. Haas, O. & J. Cairns, E. Chapter 6. Electrochemical energy storage. *Annual Reports Section 'C' (Physical Chemistry)* **95**, 163 (1999).
8. Goodenough, J. B. Electrochemical energy storage in a sustainable modern society. *Energy Environment Science* **7**, 14–18 (2014).
9. Liu, K., Liu, Y., Lin, D., Pei, A. & Cui, Y. Materials for lithium-ion battery safety. *Science Advances* **4**, (2018).
10. Manthiram, A. An Outlook on Lithium Ion Battery Technology. *ACS Central Science* **3**, 1063–1069 (2017).
11. Zhao, L. *et al.* Engineering of Sodium-Ion Batteries: Opportunities and Challenges. *Engineering* **24**, 172–183 (2023).
12. Yabuuchi, N., Kubota, K., Dahbi, M. & Komaba, S. Research Development on Sodium-Ion Batteries. *Chemical Reviews* **114**, 11636–11682 (2014).
13. Mekhilef, S., Saidur, R. & Safari, A. Comparative study of different fuel cell technologies. *Renewable and Sustainable Energy Reviews* **16**, 981–989 (2012).
14. Tariq, A. H., Kazmi, S. A. A., Hassan, M., Muhammed Ali, S. A. & Anwar, M. Analysis of fuel cell integration with hybrid microgrid systems for clean energy: A comparative review. *International Journal of Hydrogen Energy* **52**, 1005–1034 (2024).
15. Jiang, F., Li, Y. & Pan, Y. Design Principles of Single-Atom Catalysts for Oxygen Evolution Reaction: From Targeted Structures to Active Sites. *Advanced Materials* **36**, (2024).
16. Wang, J., Wen, J., Wang, J., Yang, B. & Jiang, L. Water electrolyzer operation scheduling for green hydrogen production: A review. *Renewable and Sustainable Energy Reviews* **203**, 114779 (2024).
17. Vetter, J. *et al.* Ageing mechanisms in lithium-ion batteries. *J Power Sources* **147**, 269–281 (2005).
18. Geiger, S. *et al.* Catalyst Stability Benchmarking for the Oxygen Evolution Reaction: The Importance of Backing Electrode Material and Dissolution in Accelerated Aging Studies. *ChemSusChem* **10**, 4140–4143 (2017).

19. Han, X. *et al.* A review on the key issues of the lithium ion battery degradation among the whole life cycle. *eTransportation* **1**, 100005 (2019).
20. Rieger, B., Schlueter, S., Erhard, S. V. & Jossen, A. Strain Propagation in Lithium-Ion Batteries from the Crystal Structure to the Electrode Level. *Journal of the Electrochemical Society* **163**, A1595–A1606 (2016).
21. Pegel, H. *et al.* Volume and thickness change of NMC811 SiO_x-graphite large-format lithium-ion cells: from pouch cell to active material level. *Journal of Power Sources* **537**, 231443 (2022).
22. Clerici, D., Martelli, S., Mocera, F. & Somà, A. Mechanical characterization of lithium-ion batteries with different chemistries and formats. *Journal of Energy Storage* **84**, 110899 (2024).
23. Kabir, M. M. & Demirocak, D. E. Degradation mechanisms in Li-ion batteries: a state-of-the-art review. *International Journal of Energy Research* **41**, 1963–1986 (2017).
24. Birkl, C. R., Roberts, M. R., McTurk, E., Bruce, P. G. & Howey, D. A. Degradation diagnostics for lithium ion cells. *Journal of Power Sources* **341**, 373–386 (2017).
25. Hausbrand, R. *et al.* Fundamental degradation mechanisms of layered oxide Li-ion battery cathode materials: Methodology, insights and novel approaches. *Materials Science and Engineering: B* **192**, 3–25 (2015).
26. Cabana, J., Kwon, B. J. & Hu, L. Mechanisms of Degradation and Strategies for the Stabilization of Cathode–Electrolyte Interfaces in Li-Ion Batteries. *Accounts of Chemical Research* **51**, 299–308 (2018).
27. Takahashi, I., Kiuchi, H., Ohma, A., Fukunaga, T. & Matsubara, E. Cathode Electrolyte Interphase Formation and Electrolyte Oxidation Mechanism for Ni-Rich Cathode Materials. *The Journal of Physical Chemistry C* **124**, 9243–9248 (2020).
28. Cherkashinin, G., Motzko, M., Schulz, N., Späth, T. & Jaegermann, W. Electron Spectroscopy Study of $Li[Ni,Co,Mn]O_2$ /Electrolyte Interface: Electronic Structure, Interface Composition, and Device Implications. *Chemistry of Materials* **27**, 2875–2887 (2015).
29. Gauthier, M. *et al.* Electrode–Electrolyte Interface in Li-Ion Batteries: Current Understanding and New Insights. *Journal of Physical Chemistry Letter* **6**, 4653–4672 (2015).
30. Kim, T., Ono, L. K. & Qi, Y. Understanding the active formation of a cathode–electrolyte interphase (CEI) layer with energy level band bending for lithium-ion batteries. *Journal of Material Chemistry A* **11**, 221–231 (2023).
31. Gilbert, J. A., Shkrob, I. A. & Abraham, D. P. Transition Metal Dissolution, Ion Migration, Electrocatalytic Reduction and Capacity Loss in Lithium-Ion Full Cells. *Journal Electrochemical Society* **164**, A389–A399 (2017).
32. Zhan, C., Wu, T., Lu, J. & Amine, K. Dissolution, migration, and deposition of transition metal ions in Li-ion batteries exemplified by Mn-based cathodes – a critical review. *Energy&Environment Science* **11**, 243–257 (2018).
33. Zhan, C. *et al.* Mn(II) deposition on anodes and its effects on capacity fade in spinel lithium manganate–carbon systems. *Nature Communication* **4**, 2437 (2013).
34. Liu, T. *et al.* Correlation between manganese dissolution and dynamic phase stability in spinel-based lithium-ion battery. *Nature Communication* **10**, 4721 (2019).

35. Hunter, J. C. Preparation of a new crystal form of manganese dioxide: λ-MnO_2. *Journal of Solid State Chemistry* **39**, 142–147 (1981).
36. Xiao, X., Ahn, D., Liu, Z., Kim, J.-H. & Lu, P. Atomic layer coating to mitigate capacity fading associated with manganese dissolution in lithium ion batteries. *Electrochemistry Communications* **32**, 31–34 (2013).
37. Palacín, M. R. Understanding ageing in Li-ion batteries: a chemical issue. *Chemical Society Reviews* **47**, 4924–4933 (2018).
38. Huang, Y. *et al.* Lithium Manganese Spinel Cathodes for Lithium-Ion Batteries. *Advanced Energy Materials* **11**, (2021).
39. Tesfamhret, Y., Liu, H., Chai, Z., Berg, E. & Younesi, R. On the Manganese Dissolution Process from $LiMn_2O_4$ Cathode Materials. *ChemElectroChem* **8**, 1516–1523 (2021).
40. Jang, D. H., Young J. Shin & Seung M. Oh. Dissolution of Spinel Oxides and Capacity Losses in 4 V Li / $Li_xMn_2O_4$ Cells. *Journal of Electrochemical Society* **143**, 2204–2211 (1996).
41. Hanf, L., Henschel, J., Diehl, M., Winter, M. & Nowak, S. Mn^{2+} or Mn^{3+}? Investigating transition metal dissolution of manganese species in lithium ion battery electrolytes by capillary electrophoresis. *Electrophoresis* **41**, 697–704 (2020).
42. Zhao, L., Chénard, E., Çapraz, Ö. Ö., Sottos, N. R. & White, S. R. Direct Detection of Manganese Ions in Organic Electrolyte by UV-vis Spectroscopy. *Journal of Electrochemical Society* **165**, A345–A348 (2018).
43. Wang, J., Islam, M. M. & Donne, S. W. *In-situ* detection of $LiMn_2O_4$ dissolution during electrochemical cycling by. *Electrochimica Acta* **386**, 138366 (2021).
44. Wang, L.-F., Ou, C.-C., Striebel, K. A. & Chen, J.-S. Study of Mn Dissolution from $LiMn_2O_4$ Spinel Electrodes Using Rotating Ring-Disk Collection Experiments. *Journal of Electrochemical Society* **150**, A905 (2003).
45. Chen, J.-S. *et al.* Rotating ring–disk electrode measurements on Mn dissolution and capacity losses of spinel electrodes in various organic electrolytes. *Journal of Power Sources* **157**, 515–521 (2006).
46. Wang, L.-F., Fang, B.-J. & Chen, J.-S. Rotating ring-disc electrode measurements of manganese dissolution and capacity loss of $Li_{1+x}Mn_{2-x}O_4$ and $Li_{1+x}Al_yMn_{2-x-y}O_4$ spinel electrodes for lithium-ion batteries. *Journal of Power Sources* **150**, 1–10 (2005).
47. Banerjee, A. *et al.* On the Oxidation State of Manganese Ions in Li-Ion Battery Electrolyte Solutions. *Journal of the American Chemical Society* **139**, 1738–1741 (2017).
48. Shilina, Y. *et al.* Combined Electron Paramagnetic Resonance and Atomic Absorption Spectroscopy/Inductively Coupled Plasma Analysis As Diagnostics for Soluble Manganese Species from Mn-Based Positive Electrode Materials in Li-ion Cells. *Analytical Chemistry* **88**, 4440–4447 (2016).
49. Benedek, R. Role of Disproportionation in the Dissolution of Mn from Lithium Manganate Spinel. *The Journal of Physical Chemistry C* **121**, 22049–22053 (2017).
50. Allen, J. P. & Grey, C. P. Determining the oxidation states of dissolved transition metals in battery electrolytes from solution NMR spectra. *Chemical Communications* **59**, 1677–1680 (2023).
51. Rynearson, L. *et al.* Speciation of Transition Metal Dissolution in Electrolyte from Common Cathode Materials. *Angewandte Chemie* (2023).

52. Terada, Y., Nishiwaki, Y., Nakai, I. & Nishikawa, F. Study of Mn dissolution from $LiMn_2O_4$ spinel electrodes using in situ total reflection X-ray fluorescence analysis and fluorescence XAFS technique. *Journal of Power Sources* **97–98**, 420–422 (2001).

53. Schwieters, T. *et al.* Visualizing elemental deposition patterns on carbonaceous anodes from lithium ion batteries: A laser ablation-inductively coupled plasma-mass spectrometry study on factors influencing the deposition of lithium, nickel, manganese and cobalt after dissolution and migration from the $Li1[Ni_{1/3}Mn_{1/3}Co_{1/3}]O_2$ and $LiMn_{1.5}Ni_{0.5}O_4$ cathode. *Journal of Power Sources* **380**, 194–201 (2018).

54. Abraham, D. P., Spila, T., Furczon, M. M. & Sammann, E. Evidence of Transition-Metal Accumulation on Aged Graphite Anodes by SIMS. *Electrochemical and Solid-State Letters* **11**, A226 (2008).

55. Komaba, S. *et al.* Impact of 2-Vinylpyridine as Electrolyte Additive on Surface and Electrochemistry of Graphite for $C/LiMn_2O_4$ Li-Ion Cells. *Journal of Electrochemical Society* **152**, A937 (2005).

56. Xie, X. *et al.* Oxygen Evolution Reaction in Alkaline Environment: Material Challenges and Solutions. *Advanced Functional Materials* **32**, (2022).

57. McCrory, C. C. L., Jung, S., Peters, J. C. & Jaramillo, T. F. Benchmarking Heterogeneous Electrocatalysts for the Oxygen Evolution Reaction. *Journal of the American Chemical Society* **135**, 16977–16987 (2013).

58. Ma, Z. *et al.* Reaction mechanism for oxygen evolution on RuO_2, IrO_2, and $RuO_2@IrO_2$ core-shell nanocatalysts. *Journal of Electroanalytical Chemistry* **819**, 296–305 (2018).

59. Suen, N.-T. *et al.* Electrocatalysis for the oxygen evolution reaction: recent development and future perspectives. *Chemical Society Reviews* **46**, 337–365 (2017).

60. Ayers, K. E. *et al.* Research Advances towards Low Cost, High Efficiency PEM Electrolysis. *ECS Transactions* **33**, 3–15 (2010).

61. Matute, G., Yusta, J. M. & Correas, L. C. Techno-economic modelling of water electrolysers in the range of several MW to provide grid services while generating hydrogen for different applications: A case study in Spain applied to mobility with FCEVs. *International Journal of Hydrogen Energy* **44**, 17431–17442 (2019).

62. Wang, J. *et al.* Sb incorporated into oxides enhances stability in acid during the oxygen evolution reaction by inhibiting structural distortion. *Nano Energy* **110**, 108355 (2023).

63. Song, F. *et al.* Transition Metal Oxides as Electrocatalysts for the Oxygen Evolution Reaction in Alkaline Solutions: An Application-Inspired Renaissance. *Journal of the American Chemical Society* **140**, 7748–7759 (2018).

64. Lu, F., Zhou, M., Zhou, Y. & Zeng, X. First-Row Transition Metal Based Catalysts for the Oxygen Evolution Reaction under Alkaline Conditions: Basic Principles and Recent Advances. *Small* **13**, (2017).

65. Chen, F.-Y., Wu, Z.-Y., Adler, Z. & Wang, H. Stability challenges of electrocatalytic oxygen evolution reaction: From mechanistic understanding to reactor design. *Joule* **5**, 1704–1731 (2021).

66. Cherevko, S. *et al.* Dissolution of Noble Metals during Oxygen Evolution in Acidic Media. *ChemCatChem* **6**, 2219–2223 (2014).

67. Kasian, O. *et al.* Degradation of iridium oxides *via* oxygen evolution from the lattice: correlating atomic scale structure with reaction mechanisms. *Energy & Environmental*

Science **12**, 3548–3555 (2019).

68. Frydendal, R. *et al.* Benchmarking the Stability of Oxygen Evolution Reaction Catalysts: The Importance of Monitoring Mass Losses. *ChemElectroChem* **1**, 2075–2081 (2014).
69. Li, Z., De Feyter, S. & Mertens, S. F. L. Covalent and non-covalent functionalization of graphitic substrates under electrochemical control. (PhD dissertation, Katholieke Universiteit Leuven, 2017).
70. Lazanas, A. Ch. & Prodromidis, M. I. Electrochemical Impedance Spectroscopy─A Tutorial. *ACS Measurement Science Au* **3**, 162–193 (2023).
71. Pletcher, D. *A First Course in Electrode Processes*. (RSC, 2009).
72. Hirt, T. J. & Palmer, H. B. Quantitative Determination of Carbon Suboxide by Gas Chromatography. *Analytical Chemistry* **34**, 164–164 (1962).
73. Allen J. Bard & Larry R. Faulkner. *Electrochemical Methods: Fundamentals and Applications*. (Wiley, New York, 2001).
74. Albery, W. J. & Bruckenstein, S. Ring-disc electrodes. Part 2.—Theoretical and experimental collection effciencies. *Transactions of the Faraday Society* **62**, 1920–1931 (1966).
75. Levich, V. G. *Physicochemical Hydrodynamics*. (Prentice-Hall: Englewood Cliffs, New Jersey, 1962).
76. Treimer, S., Tang, A. & Johnson, D. C. A Consideration of the Application of Koutecký-Levich Plots in the Diagnoses of Charge-Transfer Mechanisms at Rotated Disk Electrodes. *Electroanalysis* **14**, 165 (2002).
77. Prass, S., St-Pierre, J., Klingele, M., Friedrich, K. A. & Zamel, N. Hydrogen Oxidation Artifact During Platinum Oxide Reduction in Cyclic Voltammetry Analysis of Low-Loaded PEMFC Electrodes. *Electrocatalysis* **12**, 45–55 (2021).
78. Khan, S. R., Sharma, B., Chawla, P. A. & Bhatia, R. Inductively Coupled Plasma Optical Emission Spectrometry (ICP-OES): a Powerful Analytical Technique for Elemental Analysis. *Food Analytical Methods* **15**, 666–688 (2022).
79. Makonnen, Y. & Beauchemin, D. The inductively coupled plasma as a source for optical emission spectrometry and mass spectrometry. in *Sample Introduction Systems in ICPMS and ICPOES* 1–55 (Elsevier, 2020).
80. Sharp, B. L. Pneumatic nebulisers and spray chambers for inductively coupled plasma spectrometry. A review. Part 1. Nebulisers. *Journal of Analytical Atomic Spectrometry* **3**, 613 (1988).
81. Burgener, J. A. & Makonnen, Y. Nebulization systems. in *Sample Introduction Systems in ICPMS and ICPOES* 57–142 (Elsevier, 2020).
82. Aguirre, M. Á., Kovachev, N., Almagro, B., Hidalgo, M. & Canals, A. Compensation for matrix effects on ICP-OES by on-line calibration methods using a new multi-nebulizer based on Flow Blurring® technology. *Journal of Analytical Atomic Spectrometry* **25**, 1724 (2010).
83. Todoli, J.-L. & Jean-Michel Mermet. *Liquid Sample Introduction in ICP Spectrometry: A Practical Guide.* (Elsevier, 2011).
84. Maestre, S., Mora, J., Todolí, J.-L. & Canals, A. Evaluation of several commercially available spray chambers for use in inductively coupled plasma atomic emission spectrometry. *Journal of Analytical Atomic Spectrometry* **14**, 61–67 (1999).

85. Hou, X., Amais, R. S., Jones, B. T. & Donati, G. L. Inductively Coupled Plasma Optical Emission Spectrometry. in *Encyclopedia of Analytical Chemistry* 1–29 (Wiley, 2021).
86. Wiltsche, H., Wolfgang, M. & Hallwirth, F. Effects of argon on the analytical properties of a microwave-sustained, inductively coupled, atmospheric-pressure plasma. *Journal of Analytical Atomic Spectrometry* **37**, 1298–1308 (2022).
87. Luo, T. *et al.* Reassessment of the influence of carrier gases He and Ar on signal intensities in 193 nm excimer LA-ICP-MS analysis. *Journal of Analytical Atomic Spectrometry* **33**, 1655–1663 (2018).
88. Thomas, R. *Practical Guide to ICP-MS*. (CRC Press, 2013).
89. Shrivastava, A. & Gupta, V. Methods for the determination of limit of detection and limit of quantitation of the analytical methods. *Chronicles of Young Scientists* **2**, 21 (2011).
90. Nikman, S. Construction and Application of an On-line Flow Cell ICP-OES Setup for Real Time Dissolution Detection. (PhD dissertation, Lancaster University, Lancaster, 2020).
91. Ma, L. & Zhi, C. Zn electrode/electrolyte interfaces of Zn batteries: A mini review. *Electrochemistry Communications* **122**, 106898 (2021).
92. Toporski, J. & Dieing, T. *Confocal Raman Microscopy*. (Springer International Publishing AG, New York, 2018).
93. Scrosati, B. History of lithium batteries. *Journal of Solid State Electrochemistry* **15**, 1623–1630 (2011).
94. Armaroli, N. & Balzani, V. Towards an electricity-powered world. *Energy & Environmental Science* **4**, 3193 (2011).
95. International Energy Agency. *Key World Energy Statistics 2020*. https://www.iea.org/reports/key-world-energy-statistics-2020 (2020).
96. BloombergNEF. Energy storage outlook 2019. https://about.bnef.com/blog/energy-storage-investments-boom-battery-costs-halve-next-decade/ (2019).
97. Larcher, D. & Tarascon, J.-M. Towards greener and more sustainable batteries for electrical energy storage. *Nature Chemistry* **7**, 19–29 (2015).
98. Goodenough, J. B. & Kim, Y. Challenges for Rechargeable Li Batteries. *Chemistry of Materials* **22**, 587–603 (2010).
99. Guéguen, A. *et al.* Decomposition of $LiPF_6$ in High Energy Lithium-Ion Batteries Studied with Online Electrochemical Mass Spectrometry. *Journal of Electrochemical Society* **163**, A1095–A1100 (2016).
100. Dai, Y., Cai, L. & White, R. E. Capacity Fade Model for Spinel $LiMn_2O_4$ Electrode. *Journal of Electrochemical Society* **160**, A182–A190 (2013).
101. Wang, X. *et al.* Regulation of Cathode-Electrolyte Interphase via Electrolyte Additives in Lithium Ion Batteries. *Chemistry: An Asian Journal* **15**, 2803–2814 (2020).
102. Lee, Y. K., Park, J. & Lu, W. A Comprehensive Study of Manganese Deposition and Side Reactions in Li-Ion Battery Electrodes. *Journal of Electrochemical Society* **164**, A2812–A2822 (2017).
103. Wang, F. *et al.* Stabilizing high voltage $LiCoO_2$ cathode in aqueous electrolyte with interphase-forming additive. *Energy & Environmental Science* **9**, 3666–3673 (2016).
104. Li, W., Dahn, J. R. & Wainwright, D. S. Rechargeable Lithium Batteries with Aqueous Electrolytes. *Science (1979)* **264**, 1115–1118 (1994).

105. Kim, H. *et al.* Aqueous Rechargeable Li and Na Ion Batteries. *Chemical Reviews* **114**, 11788–11827 (2014).
106. Zhi, J., Bertens, K., Yazdi, A. Z. & Chen, P. Acrylonitrile copolymer/graphene skinned cathode for long cycle life rechargeable hybrid aqueous batteries at high-temperature. *Electrochimica Acta* **268**, 248–255 (2018).
107. Stich, M., Göttlinger, M., Kurniawan, M., Schmidt, U. & Bund, A. Hydrolysis of $LiPF_6$ in Carbonate-Based Electrolytes for Lithium-Ion Batteries and in Aqueous Media. *The Journal of Physical Chemistry C* **122**, 8836–8842 (2018).
108. Evertz, M., Kasnatscheew, J., Winter, M. & Nowak, S. Investigation of various layered lithium ion battery cathode materials by plasma- and X-ray-based element analytical techniques. *Analytical and Bioanalytical Chemistry* **411**, 277–285 (2019).
109. Bhandari, A. & Bhattacharya, J. Review—Manganese Dissolution from Spinel Cathode: Few Unanswered Questions. *Journal of Electrochemical Society* **164**, A106–A127 (2017).
110. Ogle, K. & Weber, S. Anodic Dissolution of 304 Stainless Steel Using Atomic Emission Spectroelectrochemistry. *Journal of Electrochemical Society* **147**, 1770 (2000).
111. Klemm, S. O. *et al.* Time and potential resolved dissolution analysis of rhodium using a microelectrochemical flow cell coupled to an ICP-MS. *Journal of Electroanalytical Chemistry* **677–680**, 50–55 (2012).
112. Alias, N. & Mohamad, A. A. Advances of aqueous rechargeable lithium-ion battery: A review. *Journal of Power Sources* **274**, 237–251 (2015).
113. Wang, M., Dong, X., Escobar, I. C. & Cheng, Y.-T. Lithium Ion Battery Electrodes Made Using Dimethyl Sulfoxide (DMSO)-A Green Solvent. *ACS Sustainable Chemistry & Engineering* **8**, 11046–11051 (2020).
114. Oliveira, E. M., Marino, C. E. B., Biaggio, S. R. & Rocha-Filho, R. C. Reactivation of passive titanium: the enhancement of O_2 evolution after potentiodynamic cyclings. *Electrochemistry Communications* **2**, 254–258 (2000).
115. Schuppert, A. K., Topalov, A. A., Katsounaros, I., Klemm, S. O. & Mayrhofer, K. J. J. A Scanning Flow Cell System for Fully Automated Screening of Electrocatalyst Materials. *Journal of Electrochemical Society* **159**, F670–F675 (2012).
116. Shkirskiy, V., Maciel, P., Deconinck, J. & Ogle, K. On The Time Resolution of the Atomic Emission Spectroelectrochemistry Method. *Journal of Electrochemical Society* **163**, C37–C44 (2016).
117. Tron, A., Park, Y. D. & Mun, J. AlF_3-coated $LiMn_2O_4$ as cathode material for aqueous rechargeable lithium battery with improved cycling stability. *Journal of Power Sources* **325**, 360–364 (2016).
118. Mertens, S. F. L. *et al.* Switching stiction and adhesion of a liquid on a solid. *Nature* **534**, 676–679 (2016).
119. Hem, J. D. *Chemical Equilibria and Rates of Manganese Oxidation - Chemistry of Manganese in Natural Water*. https://pubs.usgs.gov/wsp/1667a/report.pdf (1963).
120. Hem, J. D. Manganese Complexes with Bi-Carbonate and Sulfate in Natural Water. *J Chem Eng Data* **8**, 99–101 (1963).
121. Broughton, J. N. & Brett, M. J. Investigation of thin sputtered Mn films for electrochemical capacitors. *Electrochimica Acta* **49**, 4439–4446 (2004).

122. Ogle, K., Mokaddem, M. & Volovitch, P. Atomic emission spectroelectrochemistry applied to dealloying phenomena II. Selective dissolution of iron and chromium during active–passive cycles of an austenitic stainless steel. *Electrochimica Acta* **55**, 913–921 (2010).

123. Marchini, F., Calvo, E. J. & Williams, F. J. Effect of the electrode potential on the surface composition and crystal structure of $LiMn_2O_4$ in aqueous solutions. *Electrochimica Acta* **269**, 706–713 (2018).

124. Baumung, M., Kollenbach, L., Xi, L. & Risch, M. Undesired Bulk Oxidation of $LiMn_2O_4$ Increases Overpotential of Electrocatalytic Water Oxidation in Lithium Hydroxide Electrolytes. *ChemPhysChem* **20**, 2981–2988 (2019).

125. Benedek, R., Thackeray, M. M. & van de Walle, A. Pourbaix-like phase diagram for lithium manganese spinels in acid. *Journal of Materials Chemistry* **20**, 369–374 (2010).

126. Takahashi, K. *et al.* Electrochemical properties of lithium manganese oxides with different surface areas for lithium ion batteries. *Journal of Power Sources* **136**, 115–121 (2004).

127. Tang, D. *et al.* Surface Structure Evolution of $LiMn_2O_4$ Cathode Material upon Charge/Discharge. *Chemistry of Materials* **26**, 3535–3543 (2014).

128. Tang, D. *et al.* Electrochemical behavior and surface structural change of $LiMn_2O_4$ charged to 5.1 V. *Journal of Materials Chemistry A* **2**, 14519–14527 (2014).

129. Thackeray, M. M. *et al.* Structural Fatigue in Spinel Electrodes in High Voltage (4 V) $Li/Li_xMn_2O_4$ Cells. *Electrochemical and Solid-State Letters* **1**, 7 (1999).

130. Lee, Y. K., Park, J. & Lu, W. A Comprehensive Experimental and Modeling Study on Dissolution in Li-Ion Batteries. *Journal of Electrochemical Society* **166**, A1340–A1354 (2019).

131. Mertens, S. F. L., Mészáros, G. & Wandlowski, T. Dynamics of ionic liquid mediated quantised charging of monolayer-protected clusters. *Physical Chemistry Chemical Physics* **12**, 5417 (2010).

132. Hendriks, R., Cunha, D. M., Singh, D. P. & Huijben, M. Enhanced Lithium Transport by Control of Crystal Orientation in Spinel $LiMn_2O_4$ Thin Film Cathodes. *ACS Applied Energy Materials* **1**, 7046–7051 (2018).

133. Hanf, L., Henschel, J., Diehl, M., Winter, M. & Nowak, S. Mn^{2+} or Mn^{3+}? Investigating transition metal dissolution of manganese species in lithium ion battery electrolytes by capillary electrophoresis. *Electrophoresis* **41**, 697–704 (2020).

134. Zhao, L., Chénard, E., Çapraz, Ö. Ö., Sottos, N. R. & White, S. R. Direct Detection of Manganese Ions in Organic Electrolyte by UV-vis Spectroscopy. *Journal of Electrochemical Society* **165**, A345–A348 (2018).

135. Wang, L.-F., Ou, C.-C., Striebel, K. A. & Chen, J.-S. Study of Mn Dissolution from $LiMn_2O_4$ Spinel Electrodes Using Rotating Ring-Disk Collection Experiments. *Journal of Electrochemical Society* **150**, A905 (2003).

136. Banerjee, A. *et al.* On the oxidation state of manganese ions in li-ion battery electrolyte solutions. *Journal of the American Chemical Society* **139**, 1738–1741 (2017).

137. Shilina, Y. *et al.* Combined Electron Paramagnetic Resonance and Atomic Absorption Spectroscopy/Inductively Coupled Plasma Analysis As Diagnostics for Soluble Manganese Species from Mn-Based Positive Electrode Materials in Li-ion Cells.

Analytical Chemistry **88**, 4440–4447 (2016).

138. Benedek, R. Role of Disproportionation in the Dissolution of Mn from Lithium Manganate Spinel. *Journal of Physical Chemistry C* **121**, 22049–22053 (2017).
139. Fernández-Barcia, M. *et al.* Electrodeposition of manganese layers from sustainable sulfate based electrolytes. *Surface and Coating Technology* **334**, 261–268 (2018).
140. Nijjer, S., Thonstad, J. & Haarberg, G. M. Oxidation of manganese(II) and reduction of manganese dioxide in sulphuric acid. *Electrochimica Acta* **46**, 395–399 (2000).
141. Devadoss, V., Noel, M., Jayaraman, K. & Ahmed Basha, C. Electrochemical behaviour of Mn^{3+}/Mn^{2+}, Co^{3+}/Co^{2+} and Ce^{4+}/Ce^{4+} redox mediators in methanesulfonic acid. *Journal Applied Electrochemistry* **33**, 319–323 (2003).
142. Rodrigues, S., Shukla, A. K. & Munichandraiah, N. A cyclic voltammetric study of the kinetics andmechanism of electrodeposition of manganese dioxide. *Journal Applied Electrochemistry* **28**, 1235–1241 (1998).
143. Kao, W.-H. & Weibel, V. J. *Electrochemical Oxidation of Manganese(II) at a Platinum Electrode*. *Journal Applied Electrochemistry* **22**, (1992).
144. Clarke, C. J., Browning, G. J. & Donne, S. W. An RDE and RRDE study into the electrodeposition of manganese dioxide. *Electrochimica Acta* **51**, 5773–5784 (2006).
145. Najafpour, M. M. *et al.* Nanolayered manganese oxides: insights from inorganic electrochemistry. *Catalysis Science & Technology* **7**, 3499–3510 (2017).
146. Pourbaix, M. *Atlas of Electrochemical Equilibria in Aqueous Solutions*. (NACE International Cebelcor, Houston, Texas, USA, 1974).
147. Biedermann, G. & Palombari, R. On the Hydrolysis of the Manganese(III) Ion. *Acta Chemica Scandinavic A* **32**, 381–390 (1978).
148. Rosseinsky, D. R. & Nicol, M. J. Kinetics and mechanism of the formation of manganese(III) from manganese(II) and (VII) in aqueous perchlorate solution. *Transactions of the Faraday Society* **61**, 2718 (1965).
149. Davies, G. Some aspects of the chemistry of manganese(III) in aqueous solution. *Coord Chemical Reviews* **4**, 199–224 (1969).
150. Klewicki, J. K. & Morgan, J. J. Kinetic Behavior of Mn(III) Complexes of Pyrophosphate, EDTA, and Citrate. *Environmental Science & Technology* **32**, 2916–2922 (1998).
151. Gibson, A. J., Johannessen, B., Beyad, Y., Allen, J. & Donne, S. W. Dynamic Electrodeposition of Manganese Dioxide: Temporal Variation in the Electrodeposition Mechanism. *Journal of Electrochemical Society* **163**, H305–H312 (2016).
152. Qian, A. *et al.* Geochemical Stability of Dissolved Mn(III) in the Presence of Pyrophosphate as a Model Ligand: Complexation and Disproportionation. *Environmental Science & Technology***53**, 5768–5777 (2019).
153. Messaoudi, B., Joiret, S., Keddam, M. & Takenouti, H. *Anodic Behaviour of Manganese in Alkaline Medium*. *Electrochimica Acta* **46**, (2001).
154. Ray, K. & McCreery, R. L. Spatially Resolved Raman Spectroscopy of Carbon Electrode Surfaces: Observations of Structural and Chemical Heterogeneity. *Analytical Chemistry* **69**, 4680–4687 (1997).
155. Bernard, M., Hugot-Le Goff, A., Thi, B. V. & Cordoba de Torresi, S. Electrochromic Reactions in Manganese Oxides: I. Raman Analysis. *Journal of Electrochemical Society*

140, 3065–3070 (1993).

156. Bernardini, S., Bellatreccia, F., Della Ventura, G. & Sodo, A. A Reliable Method for Determining the Oxidation State of Manganese at the Microscale in Mn Oxides *via* Raman Spectroscopy. *Geostandards and Geoanalytical Research* **45**, 223–244 (2021).
157. Xin, Y. *et al.* A systematic spectroscopic study of laboratory synthesized manganese oxides relevant to Mars. *Journal of Raman Spectroscopy* **53**, 340–355 (2022).
158. Jarju, J. J., Figueiredo, M. C. & Kolen'ko, Y. V. Electrocatalysis using nanomaterials. in 343–420 (2021).
159. Patil, S. F., Rajurkar, N. S. & Borhade, A. V. Self-diffusion of cobalt and manganese ions in aqueous electrolyte solutions. *Journal of the Chemical Society, Faraday Transactions* **87**, 3405 (1991).
160. Gao, P. *et al.* The critical role of point defects in improving the specific capacitance of δ-MnO2 nanosheets. *Nature Communication* **8**, 14559 (2017).
161. Li, X. & Wei, B. Facile synthesis and super capacitive behavior of SWNT/MnO_2 hybrid films. *Nano Energy* **1**, 479–487 (2012).
162. Mertens, S. F., Xhoffer, C., De Cooman, B. C. & Temmerman, E. Short-Term Deterioration of Polymer-Coated 55% Al-Zn — Part 1: Behavior of Thin Polymer Films. *CORROSION* **53**, 381–388 (1997).
163. Moalleminejad, M. & Chung, D. D. L. Dielectric constant and electrical conductivity of carbon black as an electrically conductive additive in a manganese-dioxide electrochemical electrode, and their dependence on electrolyte permeation. *Carbon* **91**, 76–87 (2015).
164. Tron, A., Park, Y. D. & Mun, J. AlF_3-coated $LiMn_2O_4$ as cathode material for aqueous rechargeable lithium battery with improved cycling stability. *Journal of Power Sources* **325**, 360–364 (2016).
165. Nikman, S., Zhao, D., Gonzalez-Perez, V., Hoster, H. E. & Mertens, S. F. L. Surface or bulk? Real-time manganese dissolution detection in a lithium-ion cathode. *Electrochimica Acta* **386**, 138373 (2021).
166. Morgan Chan, Z. *et al.* Electrochemical trapping of metastable Mn^{3+} ions for activation of MnO_2 oxygen evolution catalysts. *Proceedings of the National Academy of Sciences* **115**, (2018).
167. Bisen, O. Y., Baumung, M., Tatzel, M., Volkert, C. A. & Risch, M. Manganese dissolution in alkaline medium with and without concurrent oxygen evolution in $LiMn_2O_4$. *Energy Advances* **3**, 504–514 (2024).
168. Liang, G., Peterson, V. K., See, K. W., Guo, Z. & Pang, W. K. Developing high-voltage spinel $LiNi_{0.5}Mn_{1.5}O_4$ cathodes for high-energy-density lithium-ion batteries: current achievements and future prospects. *Journal of Material Chemistry A* **8**, 15373–15398 (2020).
169. Thackeray, M. M. Exploiting the Spinel Structure for Li-ion Battery Applications: A Tribute to John B. Goodenough. *Advanced Energy Materials* **11**, (2021).
170. Ohzuku, T., Takeda, S. & Iwanaga, M. Solid-state redox potentials for $Li[Me_{1/2}Mn_{3/2}]O_4$ (Me: 3d-transition metal) having spinel-framework structures: a series of 5 volt materials for advanced lithium-ion batteries. *Journal of Power Sources* **81–82**, 90–94 (1999).
171. Yi, T.-F., Mei, J. & Zhu, Y.-R. Key strategies for enhancing the cycling stability and rate

capacity of $LiNi_{0.5}Mn_{1.5}O_4$ as high-voltage cathode materials for high power lithium-ion batteries. *Journal of Power Sources* **316**, 85–105 (2016).

172. Kim, J., Pieczonka, N. P. W. & Yang, L. Challenges and Approaches for High-Voltage Spinel Lithium-Ion Batteries. *ChemPhysChem* **15**, 1940–1954 (2014).

173. Aurbach, D. *et al.* Studies of cycling behavior, ageing, and interfacial reactions of $LiNi_{0.5}Mn_{1.5}O_4$ and carbon electrodes for lithium-ion 5-V cells. *Journal of Power Sources* **162**, 780–789 (2006).

174. Talyosef, Y. *et al.* The study of $LiNi_{0.5}Mn_{1.5}O_4$ 5-V cathodes for Li-ion batteries. *Journal of Power Sources* **146**, 664–669 (2005).

175. Kim, J. *et al.* In Situ Formation of a Cathode–Electrolyte Interface with Enhanced Stability by Titanium Substitution for High Voltage Spinel Lithium-Ion Batteries. *Advanced Materials Interfaces* **2**, (2015).

176. Yang, L., Ravdel, B. & Lucht, B. L. Electrolyte Reactions with the Surface of High Voltage $LiNi_{0.5}Mn_{1.5}O_4$ Cathodes for Lithium-Ion Batteries. *Electrochemical and Solid-State Letters* **13**, A95 (2010).

177. Kim, J.-H. *et al.* Understanding the capacity fading mechanism in $LiNi_{0.5}Mn_{1.5}O_4$/graphite Li-ion batteries. *Electrochimica Acta* **90**, 556–562 (2013).

178. Pieczonka, N. P. W. *et al.* Understanding Transition-Metal Dissolution Behavior in $LiNi_{0.5}Mn_{1.5}O_4$ High-Voltage Spinel for Lithium Ion Batteries. *The Journal of Physical Chemistry C* **117**, 15947–15957 (2013).

179. Fehse, M. *et al.* Influence of Transition-Metal Order on the Reaction Mechanism of LNMO Cathode Spinel: An *Operando* X-ray Absorption Spectroscopy Study. *Chemistry of Materials* **34**, 6529–6540 (2022).

180. Baddour-Hadjean, R. & Pereira-Ramos, J.-P. Raman Microspectrometry Applied to the Study of Electrode Materials for Lithium Batteries. *Chemical Reviews* **110**, 1278–1319 (2010).

181. Bhatia, A., Dridi Zrelli, Y., Pereira-Ramos, J.-P. & Baddour-Hadjean, R. Detailed redox mechanism and self-discharge diagnostic of 4.9 V $LiMn_{1.5}Ni_{0.5}O_4$ spinel cathode revealed by Raman spectroscopy. *Journal of Materials Chemistry A* **9**, 13496–13505 (2021).

182. Kim, J.-H., Myung, S.-T., Yoon, C. S., Kang, S. G. & Sun, Y.-K. Comparative Study of $LiNi_{0.5}Mn_{1.5}O_{4-\delta}$ and $LiNi_{0.5}Mn_{1.5}O_4$ Cathodes Having Two Crystallographic Structures: $Fd\bar{3}m$ and $P4_332$. *Chemistry of Materials* **16**, 906–914 (2004).

183. Sun, H. *et al.* Tailoring Disordered/Ordered Phases to Revisit the Degradation Mechanism of High-Voltage $LiNi_{0.5}Mn_{1.5}O_4$ Spinel Cathode Materials. *Advanced Functional Materials* **32**, (2022).

184. Gao, C. *et al.* Insights for the New Function of *N*, *N* -Dimethylpyrrolidone in Preparation of a High-Voltage Spinel $LiNi_{0.5}Mn_{1.5}O_4$ Cathode. *ACS Applied Materials & Interfaces* **13**, 20014–20023 (2021).

185. Strobel, P., Ibarra-Palos, A., Anne, M., Poinsignon, C. & Crisci, A. Cation ordering in $Li_2Mn_3MO_8$ spinels: structural and vibration spectroscopy studies. *Solid State Science* **5**, 1009–1018 (2003).

186. Branford, W., Green, M. A. & Neumann, D. A. Structure and Ferromagnetism in Mn^{4+} Spinels: $AM_{0.5}Mn_{1.5}O_4$ (A = Li, Cu; M = Ni, Mg). *Chemistry of Materials* **14**, 1649–

1656 (2002).

187. Qian, Y. *et al.* Investigation of the Effect of Extra Lithium Addition and Postannealing on the Electrochemical Performance of High-Voltage Spinel $LiNi_{0.5}Mn_{1.5}O_4$ Cathode Material. *The Journal of Physical Chemistry C* **118**, 15581–15589 (2014).

188. Chen, H., Yin, C. & Zhou, H. Solvent-controlled the morphology and electrochemical properties of $LiNi_{0.5}Mn_{1.5}O_4$ derived from metal–organic frameworks. *Ionics (Kiel)* **27**, 4995–5008 (2021).

189. Liu, D. *et al.* Spinel materials for high-voltage cathodes in Li-ion batteries. *RSC Adv.* **4**, 154–167 (2014).

190. Jehnichen, P. & Korte, C. Operando Raman Spectroscopy Measurements of a High-Voltage Cathode Material for Lithium-Ion Batteries. *Analytical Chemistry* **91**, 8054–8061 (2019).

191. Miwa, K. Prediction of Raman spectra with DFT+U method. *Physical Review B* **97**, 075143 (2018).

192. Boulet-Roblin, L. *et al.* Versatile Approach Combining Theoretical and Experimental Aspects of Raman Spectroscopy To Investigate Battery Materials: The Case of the $LiNi_{0.5}Mn_{1.5}O_4$ Spinel. *The Journal of Physical Chemistry C* **120**, 16377–16382 (2016).

193. Spence, S. L., Xu, Z., Sainio, S., Nordlund, D. & Lin, F. Tuning the Morphology and Electronic Properties of Single-Crystal $LiNi_{0.5}Mn_{1.5}O_{4-\delta}$: Exploring the Influence of LiCl–KCl Molten Salt Flux Composition and Synthesis Temperature. *Inorganic Chemistry* **59**, 10591–10603 (2020).

194. Luo, R., Chen, W. & Fang, H. Implication of Lithium Excess Induced Structure and Electrochemical Behavior Changes of $LiNi_{0.5}Mn_{1.5}O_4$ Spinel. *Journal of Electrochemical Society* **168**, 040527 (2021).

195. Shin, D. W., Bridges, C. A., Huq, A., Paranthaman, M. P. & Manthiram, A. Role of Cation Ordering and Surface Segregation in High-Voltage Spinel $LiMn_{1.5}Ni_{0.5-x}M_xO_4$ (M = Cr, Fe, and Ga) Cathodes for Lithium-Ion Batteries. *Chemistry of Materials* **24**, 3720–3731 (2012).

196. Solchenbach, S., Wetjen, M., Pritzl, D., Schwenke, K. U. & Gasteiger, H. A. Lithium Oxalate as Capacity and Cycle-Life Enhancer in LNMO/Graphite and LNMO/SiG Full Cells. *Journal of Electrochemical Society* **165**, A512–A524 (2018).

197. Dokko, K., Mohamedi, M., Anzue, N., Itoh, T. & Uchida, I. In situ Raman spectroscopic studies of $LiNi_xMn_{2-x}O_4$ thin film cathode materials for lithium ion secondary batteries. *Journal of Materials Chemistry* **12**, 3688–3693 (2002).

198. Zhu, W. *et al.* In-situ Raman spectroscopic investigation of $LiMn_{1.45}Ni_{0.45}M_{0.1}O_4$ (M = Cr, Co) 5 V cathode materials. *Journal of Power Sources* **298**, 341–348 (2015).

199. Ni, M., Leung, D. Y. C. & Leung, M. K. H. A review on reforming bio-ethanol for hydrogen production. *International Journal of Hydrogen Energy* **32**, 3238–3247 (2007).

200. Rostrup-Nielsen, J. R., Sehested, J. & Nørskov, J. K. Hydrogen and synthesis gas by steam- and CO_2 reforming. in 65–139 (2002).

201. Carmo, M., Fritz, D. L., Mergel, J. & Stolten, D. A comprehensive review on PEM water electrolysis. *International Journal of Hydrogen Energy* **38**, 4901–4934 (2013).

202. Schalenbach, M. *et al.* Acidic or Alkaline? Towards a New Perspective on the Efficiency of Water Electrolysis. *Journal of Electrochemical Society* **163**, F3197–F3208 (2016).

203. Stoerzinger, K. A., Qiao, L., Biegalski, M. D. & Shao-Horn, Y. Orientation-Dependent Oxygen Evolution Activities of Rutile IrO_2 and RuO_2. *Journal of Physical Chemistry Letter* **5**, 1636–1641 (2014).
204. Lee, Y., Suntivich, J., May, K. J., Perry, E. E. & Shao-Horn, Y. Synthesis and Activities of Rutile IrO_2 and RuO_2 Nanoparticles for Oxygen Evolution in Acid and Alkaline Solutions. *Journal of Physical Chemistry Letter* **3**, 399–404 (2012).
205. Divanis, S., Kutlusoy, T., Ingmer Boye, I. M., Man, I. C. & Rossmeisl, J. Oxygen evolution reaction: a perspective on a decade of atomic scale simulations. *Chemical Science* **11**, 2943–2950 (2020).
206. Man, I. C. *et al.* Universality in Oxygen Evolution Electrocatalysis on Oxide Surfaces. *ChemCatChem* **3**, 1159–1165 (2011).
207. Briquet, L. G. V., Sarwar, M., Mugo, J., Jones, G. & Calle-Vallejo, F. A New Type of Scaling Relations to Assess the Accuracy of Computational Predictions of Catalytic Activities Applied to the Oxygen Evolution Reaction. *ChemCatChem* **9**, 1261–1268 (2017).
208. García-Mota, M. *et al.* Tailoring the Activity for Oxygen Evolution Electrocatalysis on Rutile TiO_2(110) by Transition-Metal Substitution. *ChemCatChem* **3**, 1607–1611 (2011).
209. Jang, D. M. *et al.* Transition-Metal Doping of Oxide Nanocrystals for Enhanced Catalytic Oxygen Evolution. *The Journal of Physical Chemistry C* **119**, 1921–1927 (2015).
210. García-Mota, M., Vojvodic, A., Abild-Pedersen, F. & Nørskov, J. K. Electronic Origin of the Surface Reactivity of Transition-Metal-Doped TiO_2(110). *The Journal of Physical Chemistry C* **117**, 460–465 (2013).
211. Seitz, L. C., Nordlund, D., Gallo, A. & Jaramillo, T. F. Tuning Composition and Activity of Cobalt Titanium Oxide Catalysts for the Oxygen Evolution Reaction. *Electrochimica Acta* **193**, 240–245 (2016).
212. Umebayashi, T., Yamaki, T., Itoh, H. & Asai, K. Analysis of electronic structures of 3d transition metal-doped TiO_2 based on band calculations. *Journal of Physics and Chemistry of Solids* **63**, 1909–1920 (2002).
213. Roy, N., Sohn, Y., Leung, K. T. & Pradhan, D. Engineered Electronic States of Transition Metal Doped TiO_2 Nanocrystals for Low Overpotential Oxygen Evolution Reaction. *The Journal of Physical Chemistry C* **118**, 29499–29506 (2014).
214. Wang, Y., Zhang, R., Li, J., Li, L. & Lin, S. First-principles study on transition metal-doped anatase TiO_2. *Nanoscale Research Letter* **9**, 46 (2014).
215. Luo, H. *et al.* Photocatalytic Activity Enhancing for Titanium Dioxide by Co-doping with Bromine and Chlorine. *Chemistry of Materials* **16**, 846–849 (2004).
216. Srinivasan, S. S., Wade, J., Stefanakos, E. K. & Goswami, Y. Synergistic effects of sulfation and co-doping on the visible light photocatalysis of TiO_2. *Journal of Alloys and Compounds* **424**, 322–326 (2006).
217. Yuan, Z., Jia, J. & Zhang, L. Influence of co-doping of Zn(II)+Fe(III) on the photocatalytic activity of TiO_2 for phenol degradation. *Materials Chemistry and Physics* **73**, 323–326 (2002).
218. Erbe, A. *et al. Operando* studies of Mn oxide based electrocatalysts for the oxygen evolution reaction. *Physical Chemistry Chemical Physics* **25**, 26958–26971 (2023).

219. Lu, Z. *et al.* Electrochemical tuning of layered lithium transition metal oxides for improvement of oxygen evolution reaction. *Nature Communication* **5**, 4345 (2014).

220. Wold, A. & Ward, R. Perowskite-Type Oxides of Cobalt, Chromium and Vanadium with Some Rare Earth Elements. *Journal of the American Chemical Society* **76**, 1029–1030 (1954).

221. Dias, J. A., Andrade, M. A. S., Santos, H. L. S., Morelli, M. R. & Mascaro, L. H. Lanthanum-Based Perovskites for Catalytic Oxygen Evolution Reaction. *ChemElectroChem* **7**, 3173–3192 (2020).

222. Hu, Y. *et al.* Thermal decomposition of ammonium perchlorate over perovskite catalysts: Catalytic decomposition behavior, mechanism and application. *Applied Surface Science* **513**, 145849 (2020).

223. Mefford, J. T. *et al.* Water electrolysis on $La_{1-x}Sr_xCoO_{3-\delta}$ perovskite electrocatalysts. *Nature Communication* **7**, 11053 (2016).

224. Wan, M. *et al.* Building block nanoparticles engineering induces multi-element perovskite hollow nanofibers structure evolution to trigger enhanced oxygen evolution. *Electrochimica Acta* **279**, 301–310 (2018).

225. Hwang, C., Gwon, O., Jo, H., Ok, K. M. & Kim, G. Major Role of Surface Area in Perovskite Electrocatalysts for Alkaline Systems. *ChemElectroChem* **4**, 468–471 (2017).

226. Cheng, X. *et al.* Oxygen Evolution Reaction on $La_{1-x}Sr_xCoO_3$ Perovskites: A Combined Experimental and Theoretical Study of Their Structural, Electronic, and Electrochemical Properties. *Chemistry of Materials* **27**, 7662–7672 (2015).

227. Wan, G. *et al.* Amorphization mechanism of $SrIrO_3$ electrocatalyst: How oxygen redox initiates ionic diffusion and structural reorganization. *Science Advances* **7**, (2021).

228. Seo, M. H., Park, H. W., Lee, D. U., Park, M. G. & Chen, Z. Design of Highly Active Perovskite Oxides for Oxygen Evolution Reaction by Combining Experimental and ab Initio Studies. *ACS Catalysis* **5**, 4337–4344 (2015).

229. Anantharaj, S., Kundu, S. & Noda, S. "The Fe Effect": A review unveiling the critical roles of Fe in enhancing OER activity of Ni and Co based catalysts. *Nano Energy* **80**, 105514 (2021).

230. Lopes, P. P. *et al.* Dynamics of electrochemical Pt dissolution at atomic and molecular levels. *Journal of Electroanalytical Chemistry* **819**, 123–129 (2018).

231. Parsons, R. The rate of electrolytic hydrogen evolution and the heat of adsorption of hydrogen. *Transactions of the Faraday Society* **54**, 1053 (1958).

232. Chung, D. Y. *et al.* Activity–Stability Relationship in Au@Pt Nanoparticles for Electrocatalysis. *ACS Energy Letter* **5**, 2827–2834 (2020).

233. Kasian, O., Geiger, S., Mayrhofer, K. J. J. & Cherevko, S. Electrochemical On-line ICP-MS in Electrocatalysis Research. *Chemical Record* **19**, 2130–2142 (2019).

234. Pedersen, A. *et al. Operando* Fe dissolution in Fe–N–C electrocatalysts during acidic oxygen reduction: impact of local pH change. *Energy & Environmental Science* **17**, 6323–6337 (2024).

235. Dong, L. *et al.* Hydrothermal growth of rutile TiO_2 nanorod films on titanium substrates. *Thin Solid Films* **519**, 4634–4640 (2011).

236. Finnegan, M. P., Zhang, H. & Banfield, J. F. Phase Stability and Transformation in Titania Nanoparticles in Aqueous Solutions Dominated by Surface Energy. *The Journal*

of Physical Chemistry C **111**, 1962–1968 (2007).

237. Cherevko, S., Reier, T., Zeradjanin, A. R., Pawolek, Z., Strasser, P. & Mayrhofer, K. J. J. Stability of nanostructured iridium oxide electrocatalysts during oxygen evolution reaction in acidic environment. *Electrochemistry Communications* **48**, 81–85 (2014).
238. Cui, X., Zhou, X., Liang, W., Tuo, K., Wang. P., Cui, X., Zhang, L. & Li, S. Exploring the action mechanism of magnesium in different cations sites for $LiNi_{0.5}Mn_{1.5}O_4$ cathode materials. *Materials Today Sustainability* **17**, 100105 (2023).
239. Liu, Y., Liu, J., Kuo, Y. & Kuo, J. Simultaneous structure and surface engineering of metal-organic framework derived $LiNi_{0.5-x}Fe_{2x}Mn_{1.5-x}O_4$ cathode material for improving high voltage performance of lithium-ion batteries. *Materials Today Energy* **46**, 101711 (2024).